DURABILITY AND PREDICTION OF LONG-TERM PERFORMANCE OF CARBON FIBER REINFORCED POLYMER (CFRP) LAMINATES UNDER ENVIRONMENTAL CONDITIONS

by

EYAD ABDULLAH ALSUHAIBANI

DISSERTATION

Presented to the Faculty of the Graduate School of

The University of Texas at Arlington in Partial Fulfillment

of the Requirements

for the Degree of

DOCTOR OF PHILOSOPHY

THE UNIVERSITY OF TEXAS AT ARLINGTON

August 2020

Arlington, Texas

Acknowledgments

First and foremost, I would like to thank my God (Allah) for giving me the strength, knowledge, ability, passion, and opportunity to undertake this research and to persevere and complete it satisfactorily. From him, through him and to him are all things.

In my journey towards this degree, I have found a teacher, a friend, an inspiration, and a pillar of support, Professor Nur Yazdani. My sincere appreciation goes to him for his continuous support, guidance, patience, and mentorship. Without his supervision, this research would not have been successfully completed.

I would like to extend my deepest gratitude to Dr. Raad Azzawi, Dr. Samantha Sabatino, and Dr. Bill Carroll for serving on my dissertation committee and for their encouragement, advice, and interest during my study.

I am thankful to my friend, Dr. Eyosias Beneberu, for his continuous help and guidance during the research work. Also, special thanks to my friends and colleagues: Ahmed Alateeq, Karzan Habeeb, Dr. Tariq Aljaafreh, Dr. Towfiqul Quadir, Mohd Rahman, Mai Aljaberi, Khadiza Jalal, and Ikram Efaz for their help during this research.

I am grateful to the Department of Civil Engineering at UT Arlington for providing me with support and facilities to perform my research work.

July 1, 2020

Dedication

This dissertation is dedicated to my parents for their infinite love, support, and prayers.

With special appreciation to my best friend, love, and wife, Eng. Reem Alsogaih, for her endless encouragement throughout my career.

And, to my son, Abdullah, whose smile is the most pleasant in my life and has been my motivation resource.

Abstract

PREDICTION OF LONG-TERM PERFORMANCE AND DURABILITY OF CARBON FIBER REINFORCED POLYMER UNDER ENVIRONMENTAL CONDITIONS

Eyad Alsuhaibani, PhD

The University of Texas at Arlington, 2020

Supervising Professor: Nur Yazdani

Strengthening deteriorated concrete structures with carbon fiber reinforced polymer (CFRP) has been widely validated through laboratory experiments and field tests. Questions and concerns persist related to the CFRP's long-term performance and service life, however, thus the main objective of this research was to evaluate its durability under various environmental conditions. This research is divided into four distinct phases. In the first phase, the deterioration trends of CFRP laminate under environmental regimes were evaluated after immersion in water at 23, 45, and 60 °C for periods up to 32 weeks. In the second phase, four prediction models of the long-term performance were completed and calibrated with real data from the field, and the most applicable model was used to evaluate the environmental reduction factor, C_E, from ACI 440.2R (2017). The third phase involved evaluating the durability performance of externally bonded CFRP concrete beams under environmental conditions, using direct tension pull-off and three-point flexural tests. In the fourth phase, numerical analyses were performed to simulate the flexural test of externally bonded CFRP concrete beams, using ABAQUS, a non-linear

finite element software. The numerical analyses were calibrated with the experimental results and other parameters were studied.

The environmental reduction factor from ACI 440.2R (2017) was evaluated and compared with five international strengthening guidelines. The comparative results showed that ACI 440.2R (2017) overestimated the tensile strength of CFRP material, which could result in unsafe conditions before the end of the designed service life. Hence, a function to estimate the environmental reduction factor was proposed, and 75% strength retention was anticipated after a service life of 75 years.

Table of Contents

List of Figures

List of Tables

Chapter 1. Introduction

1.1 Background

According to the American Society of Civil Engineers (ASCE, 2017), America's infrastructure score is a D+, a score which indicates that the infrastructure is showing major signs of deterioration and is approaching the end of its service life. This is due to durability issues that might be caused by corrosion of the steel in reinforced concrete structures. Hence, there is considerable interest in a new non-metallic reinforcement, FRP composites, that can be used in new structures or applied to existing structures to strengthen them. FRP composites consist of high strength and continuous fibers embedded in a binding agent or matrix resin, as illustrated in Figure 1-1, and much attention is being paid to its ability to strengthen deteriorated concrete structures, including beams, slabs, columns, and walls (Breña et al., 2001; Karbhari and Seible, 2000; Pendhari et al., 2008).

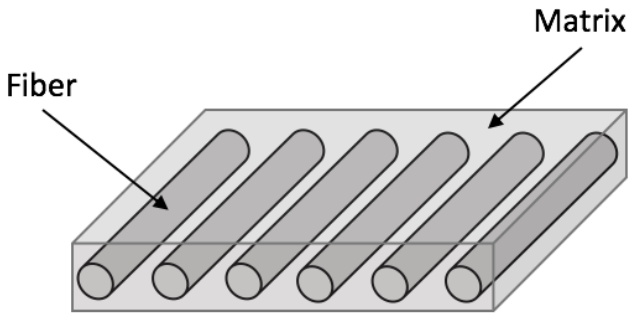

Figure 1-1 Schematic view showing the typical unidirectional FRP laminate

The specific strength, calculated as shown in Eq. (1-1), was considered and compared with traditional materials to measure the mechanical advantage of fiber composites:

$$\text{specific strength} = \frac{\sigma_{ult}}{\rho g} \tag{1-1}$$

where: σ_{ult} = the ultimate strength,

ρ = the density of the material, and

g = the acceleration due to gravity (32.2 ft/s^2 or 9.81 m/s^2).

The specific strength is extremely high in aramid and carbon fibers compared with other traditional materials, as shown in Figure 1-2. For instance, graphite/epoxy and steel rods with identical cross-sectional areas are designed to take a fixed axial load; however, the mass of the graphite/epoxy rod would be one-third of the steel rod, which equates to reduced material and energy costs.

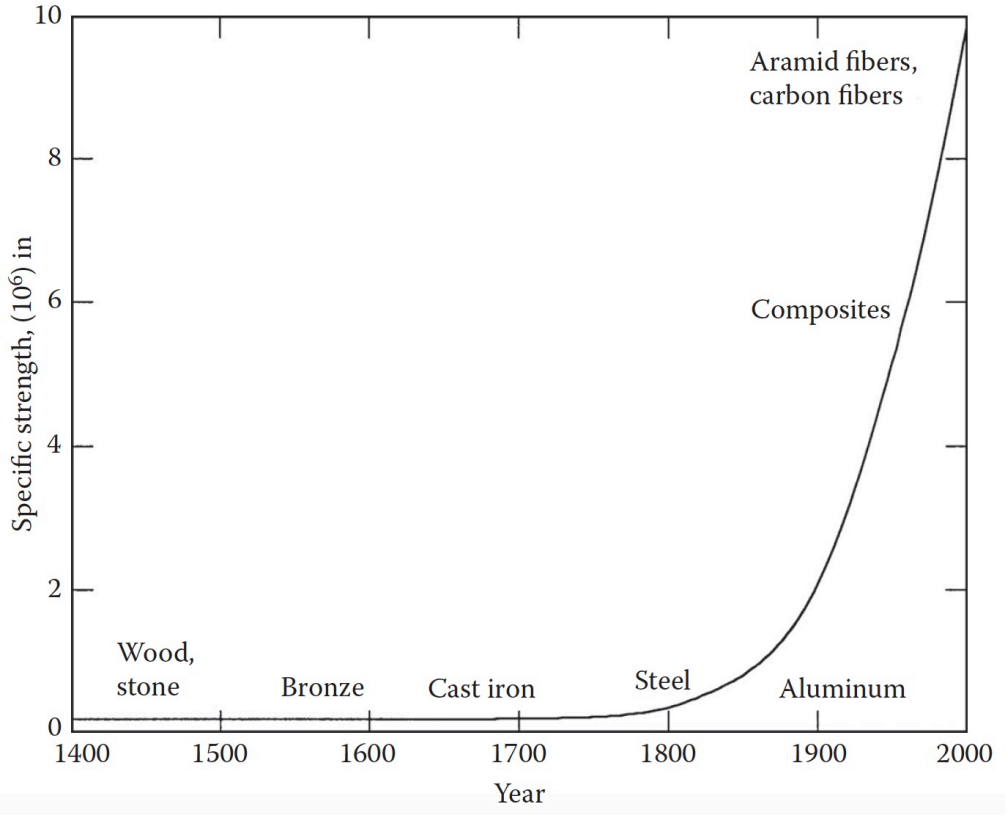

Figure 1-2 Specific strength as a function of time of use of materials (Kaw, 2006)

The attention that FRP composites have received from the engineering community can be attributed to their outstanding performance. The advantages of FRP composites are as follows:

- High tensile strength;
- Light weight and relative ease of application, which result in lowering construction time and labor;
- Corrosion resistance;
- High strength-to-weight ratio;
- Nonmagnetic electrical insulation; and
- Small creep deformation.

FRP composite materials used in civil infrastructures are based on carbon fiber reinforced polymer (CFRP), glass fiber reinforced polymer (GFRP), or aramid fiber reinforced polymer (AFRP). Fibers are the main stress-bearing constituent, while the resin polymer transfers stresses among fibers and protects them. Each fiber type is a unique combination of resins such as epoxy, phenolics, acrylic, vinyl-ester, urethane, and/or polyamide. The most common type of matrix material is epoxy, due to its behavior that includes high strength and low shrink rates.

1.2 Problem Statement

On May 28, 2005, the MacArthur Blvd./State Highway 183 (SH 183) bridge in Irving, Texas experienced extensive fire damage. It took 48 days to the repair the bridge by chipping out the deteriorated concrete areas, cleaning the rebar, applying mortar to the removed areas, and strengthening several columns and girders by applying CFRP.

Later, on June 16, 2017, four CFRP coupon samples were obtained from a U-wrap of a girder in span 3 of the bridge and were tested in the laboratory to obtain the tensile strength. After comparing the field samples with them, the field samples were degraded 21.38 % over 11.92 years (4354 days), as shown in Table 1-1. The tensile strength retention for the field data was 78.62% (Timilsina, 2018; Timilsina et al., 2020); however, the environmental reduction factor, C_E, from ACI 440.2R (2017) is 85% for carbon fiber used in bridges, as shown in Table 1-2. It should be noted that the tensile strength retention for field data was beyond the threshold of the environmental reduction factor, C_E, by 6.38 %, which may result in unsafe conditions before the end of the designed service life. The sequence of events that occurred to the MacArthur Blvd/SH183 bridge is displayed in Figure 1-3.

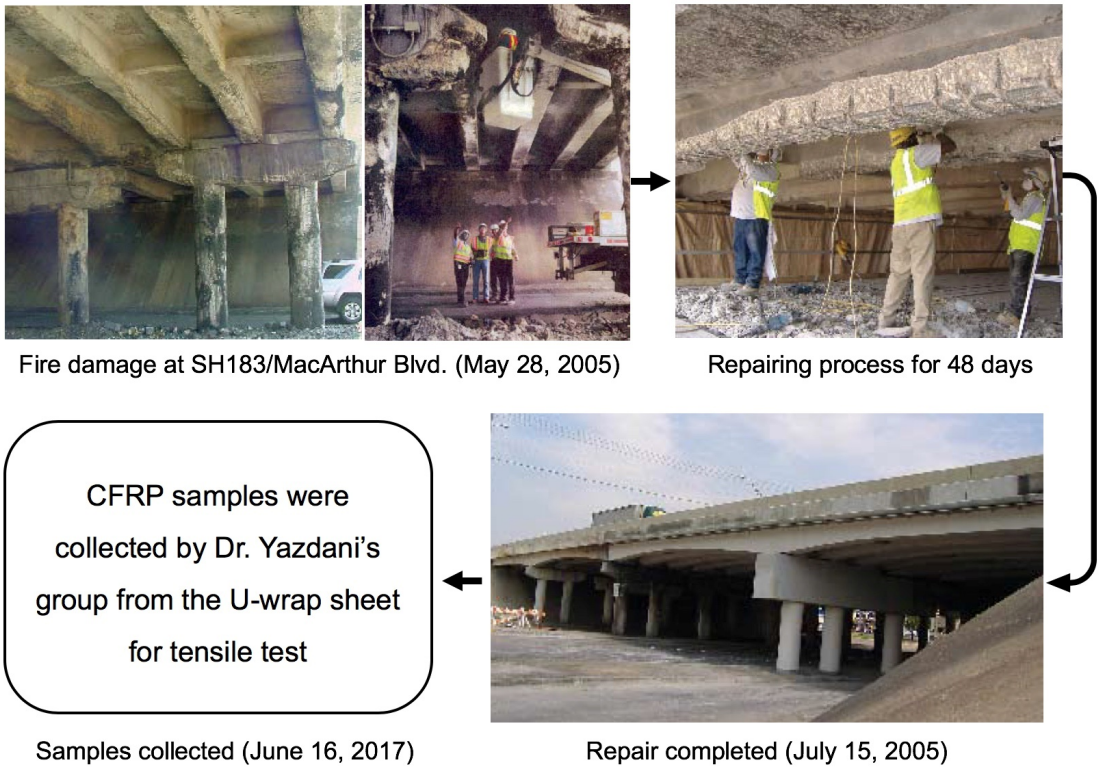

Figure 1-3 Sequence of events at the MacArthur Blvd./SH183 bridge, photo credits (Sika Corporation, 2006)

Table 1-1 Field and lab fail stress results of Timilsina's research

	Lab Sample	Field Sample
Average fail stress, MPa (ksi)	725 (105.15)	570 (82.67)
Standard deviation, MPa (ksi)	136.3 (19.8)	70.8 (10.3)
Tensile strength retention, %	100	78.62

Table 1-2 Environmental reduction factor for various FPA systems and exposure conditions (ACI 440.2R-17, 2017)

Exposure conditions	Fiber type	Environmental reduction factor, C_E
Interior exposure	Carbon	0.95
	Glass	0.75
	Aramid	0.85
Exterior exposure (bridges, piers, and open parking garages)	Carbon	0.85
	Glass	0.65
	Aramid	0.75
Aggressive environment (chemical plants and wastewater treatment plants)	Carbon	0.85
	Glass	0.50
	Aramid	0.70

ACI 440.2R-17 (2017) does not provide an explanation of how the environmental reduction factor of CFRP was approached, which has led researchers to fill the gap by studying CFRP's long-term performance, durability, and resistance to environmental contaminants. Several studies have been conducted on the long-term durability of the

FRP service life by employing predictive models such as the Arrhenius method (Abanilla et al., 2005; Cromwell et al., 2011; Li et al., 2017). However, due to the lack of real data from the field for calibration purposes, there is a level of uncertainty related to the environmental reduction factors and the long-term performance of FRP composites.

1.3 Objectives

Carbon fiber reinforced polymer (CFRP) composites are expected to strengthen and retrofit deteriorated concrete structures, but extensive investigations are needed to evaluate their long-term performance, durability, and service life. Thus, this research was conducted with the following main objectives:

- Evaluate the deterioration trends of CFRP laminate under three different environmental conditions, through a series of tensile strength tests conducted after specific exposure periods.
- Predict the long-term performance of CFRP using the Arrhenius method.
- Calibrate the effectiveness of the new prediction model with real data from the field.
- Evaluate the environmental reduction factor, C_E, from ACI 440.2R (2017).
- Propose an equation to estimate the environmental reduction factor of CFRP.
- Investigate the degradation mechanism of externally bonded CFRP concrete beams under environmental conditions using flexural and pull-off tests.
- Develop numerical modeling of externally bonded CFRP concrete beams to simulate and calibrate the flexural test with experimental results and expand the parametric study.

1.4 Organization of the Dissertation

The dissertation is organized into six chapters; the content of each is described below.

Chapter 1. Introduction

Chapter one gives brief idea on the research background, problem statement, objectives, and the organization of the dissertation.

Chapter 2. Literature Review

This chapter presents a review of previous research conducted on the durability of FRP composites under several environmental conditions. Models used to predict the long-term performance of FRP and numerical studies of externally bonded FRP concrete systems are discussed.

Chapter 3. Experimental Program

Chapter three describes the preparation of CFRP laminate and externally bonded CFRP concrete beams and provides comprehensive information about the environmental conditions to which they were exposed. Experiments conducted on CFRP laminate and externally bonded CFRP concrete beams are also presented in detail.

Chapter 4. Experimental Results and Discussions

The results obtained from the experimental tensile tests conducted on CFRP laminates are discussed, and four prediction models are proposed and calibrated with the field data. The environmental reduction factor of CFRP materials from (ACI 440.2R-17, 2017) is evaluated and compared with other international strengthening guidelines.

Flexural and direct pull-off results of externally bonded CFRP concrete beams are reviewed, as well as the associated failure mode of each test.

Chapter 5. Finite Element Modeling

A complete analysis model involves choosing a suitable numerical approach, modeling each material using precise rules, mesh verification, and steps to obtain a calibrated finite element mode That process is presented in this chapter, as well as a comparison of the load-deflection curves for the experimental and finite element models and other parameters.

Chapter 6. Conclusions and Recommendations

A summary of the findings and conclusions drawn from the experimental and theoretical studies are presented in this chapter, and recommendations for further research are discussed.

Chapter 2. Literature Review

2.1 Fiber Reinforced Polymers (FRP)

In recent decades, fiber-reinforced polymer (FRP) composites, consisting of high strength fibers embedded in a binding agent or matrix resin, have been increasingly used in civil infrastructures. A microscopic view of CFRP, taken with the aid of a scanning electron microscope (SEM), is shown in Figure 2-1. The advantages of FRP composites are high tensile strength, light weight, corrosion resistance, and relative ease of application (ACI 440.2R-17, 2017). Field applications and laboratory experiments have established that externally bonded FRP systems can improve the structural performance of existing concrete beams, slabs, columns, and walls (Breña et al., 2001; Pendhari et al., 2008; Rahimi and Hutchinson, 2001).

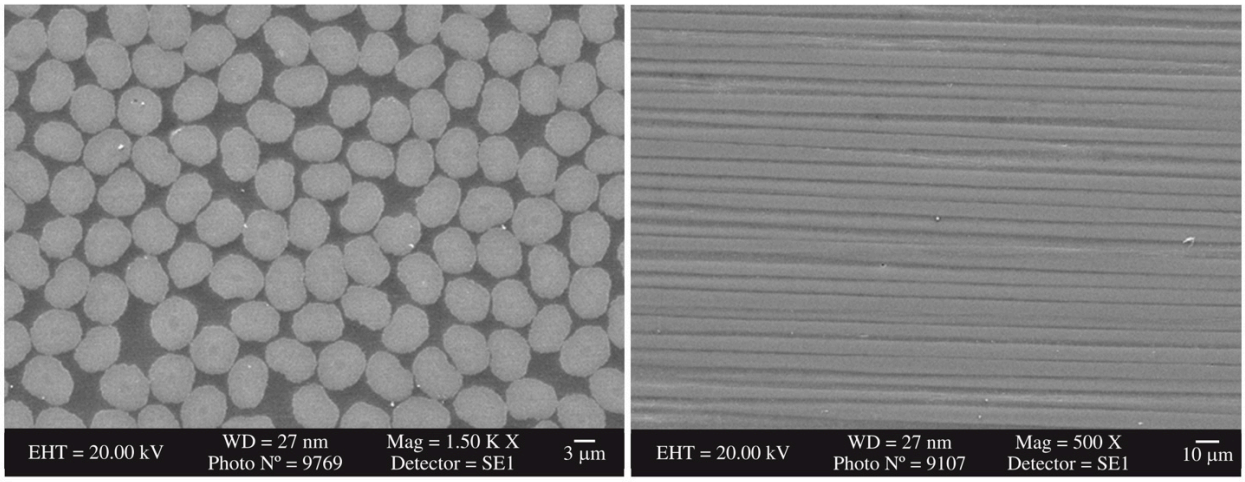

(a) (b)

Figure 2-1 SEM micrograph showing: (a) longitudinal and cross-sectional uniform distribution of carbon fibers in epoxy matrix (Srinivasaa et al., 2010)

The characteristics of FRP composites depend on the type and volume fraction of the fiber, matrix, and properties. Most of the applied load is carried by the fibers, and the

matrix serves as a binding agent for both the fibers and surrounding structures. Various types of FRP composite materials are used in civil infrastructures, including carbon fiber reinforced polymer (CFRP), glass fiber reinforced polymer (GFRP), and aramid fiber reinforced polymer (AFRP). Each type of FRP composite has its own unique properties and applications, as listed in Table 2-1.

Table 2-1 Qualitative comparison of laminates (Meier, 1995)

Property	Carbon laminate	E-glass laminate	Aramid laminate
Tensile strength	Very good	Very good	Very good
Compressive strength	Very good	Good	Inadequate
Modulus of elasticity	Very good	Adequate	Good
Long term behavior	Very good	Adequate	Good
Fatigue behavior	Excellent	Adequate	Good
Bulk density	Good	Adequate	Excellent
Alkaline resistance	Very good	Inadequate	Good
Cost	Adequate	Very good	Adequate

2.2 Durability of FRP

Numerous studies have been conducted, using aging tests to examine the long-term performance of FRP composites. Silva, et al. (2014) studied the degradation of GFRP laminates under accelerated aging systems by immersing them in a saltwater solution at 30, 40, and 55 °C and salt fog cycles for a period up to 5000 hours. The physical and mechanical properties of GFRP were examined by moisture absorption and

tensile tests, which revealed that the tensile strength decreased after immersion in a saltwater solution, and as the water temperature increased, the solution uptake by the composites and the degradation also increased.

Li, et al. (2017) investigated the mechanical properties of CFRP and GFRP laminates subjected to sustained loads and environmental conditions, including hygrothermal aging, freeze-thaw cycles, and wet-dry cycles. The sustained loads were 30% and 60% of the ultimate loads. Their results showed that the hygrothermal aging test significantly decreased the tensile strength and elongation of the CFRP and GFRP specimens with sustained loads. For the load-free condition, the wet-dry cycles aging test revealed a major decrease in tensile strength, but the tensile modulus showed excellent resistance to degradation.

Homam, et al. (2000) studied the long-term durability of FRP subjected to various environmental conditions such as freeze-thaw cycles, UV radiation, temperature variations, an alkaline environment, and moisture. Specimens were examined by direct tension and direct shear tests, which revealed that the mechanical properties of FRP materials are resistant to all of the environmental conditions mentioned except moisture.

Cao et al. (2009) conducted research on the tensile characteristics of CFRP and hybrid FRP composites at temperatures ranging from 16 to 200 °C. The hybrid composites were carbon/glass and carbon/basalt FRP sheets. The tensile strength of the CFRP decreased significantly with increasing temperatures, up to the point where the polymer exceeded its glass transition temperature. Then it remained steady at an ultimate value, as shown in Figure 2-2. It was concluded that hybridization of CFRP with glass or

basalt fibers can improve the tensile strength and strain performance more than single CFRP sheets.

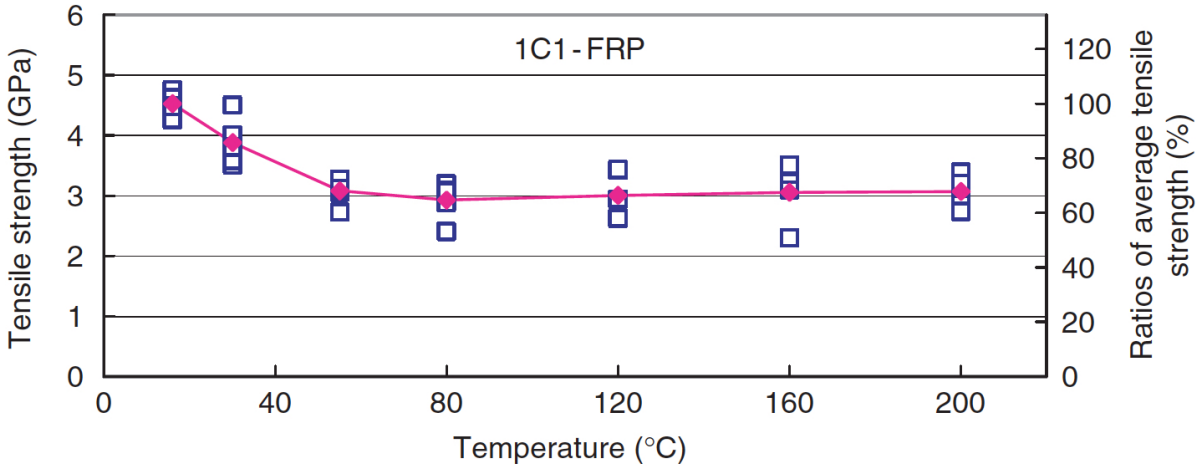

Figure 2-2 Tensile strengths and average strength ratios of CFRP sheets at various temperatures (Cao et al., 2009)

Uthaman et al. (2020) investigated the behavior of neat resin (epoxy) and CFRP plates immersed in water and acidic and alkaline solutions at temperatures of 20, 40, and 60 °C. The dynamic mechanical analysis (DMA), tensile test, and scanning electron microscopy were used to characterize the materials at intervals of 20, 40, and 80 days of exposure. The tensile strength of both the epoxy and CFRP decreased as the temperature increased in all of the solutions. The tensile strength reduction of CFRP was 20%, 25%, and 24% for water, acidic, and alkaline solutions, respectively; however, the modulus of elasticity did not significantly change during aging.

2.3 Prediction of FRP Service Life

The prediction of the long-term effects and service life of FRP composites in civil infrastructure is lacking attention from researchers (Bank et al., 2003; Chen et al., 2006; Karbhari and Abanilla, 2007; Phani and Bose, 1987). Due to its accurate results, the

Arrhenius approach is used to show first-order effects (Karbhari and Abanilla, 2007). The main hypothesis of the Arrhenius method is that the single dominant degradation mechanism does not change with temperature and time. When the temperature is increased, however, the degradation rate accelerates. The degradation rate proposed by Nelson (2004) is shown in Eq. (2-1) :

$$k = A \times \exp\left(\frac{-E_a}{RT}\right) \tag{2-1}$$

where: *k* = degradation rate (1/time),

A = constant of the material and degradation process,

E_a= activation energy associated with the set of mechanism,

R = universal gas constant (8.3143 10^{-3} kJ/mol K), and

T = temperature in Kelvin.

Phani and Bose (1987, 1986) studied the flexural strength of GFRP composite laminates under hydrothermal aging, using the acousto-ultrasonic technique and three-point bending test. They proposed a prediction model based on the Arrhenius method, in which the strength after exposure for a time period, t, is given by Eq. (2-2):

$$\sigma(t) = (\sigma_0 - \sigma_\infty)\left[\frac{-t}{\tau_0}\exp\left(\frac{-E_a}{RT}\right)\right] + \sigma_\infty \tag{2-2}$$

where: σ_0 = the unexposed strength of the composite,

σ_∞ = the asymptotic composite strength after long-term exposure,

t = the exposure time, and

τ_0 = a constant determined from Eq. (2-3):

$$\frac{1}{\tau} = \frac{1}{\tau_0} \exp\left(\frac{-E_a}{RT}\right) \tag{2-3}$$

where: τ = the characteristic time.

Bank et al. (2003) proposed a model specification for FRP composite materials and a protocol for predicting long-term property values subjected to accelerated aging, based on the Arrhenius model. The property retention of accelerated aged specimens at the time of testing versus the logarithmic time can be plotted, as shown in Figure 2-3 (a). The Arrhenius plot can be created as logarithmic time versus the inverse absolute temperature for various percentages of property retention, as shown in Figure 2-3 (b).

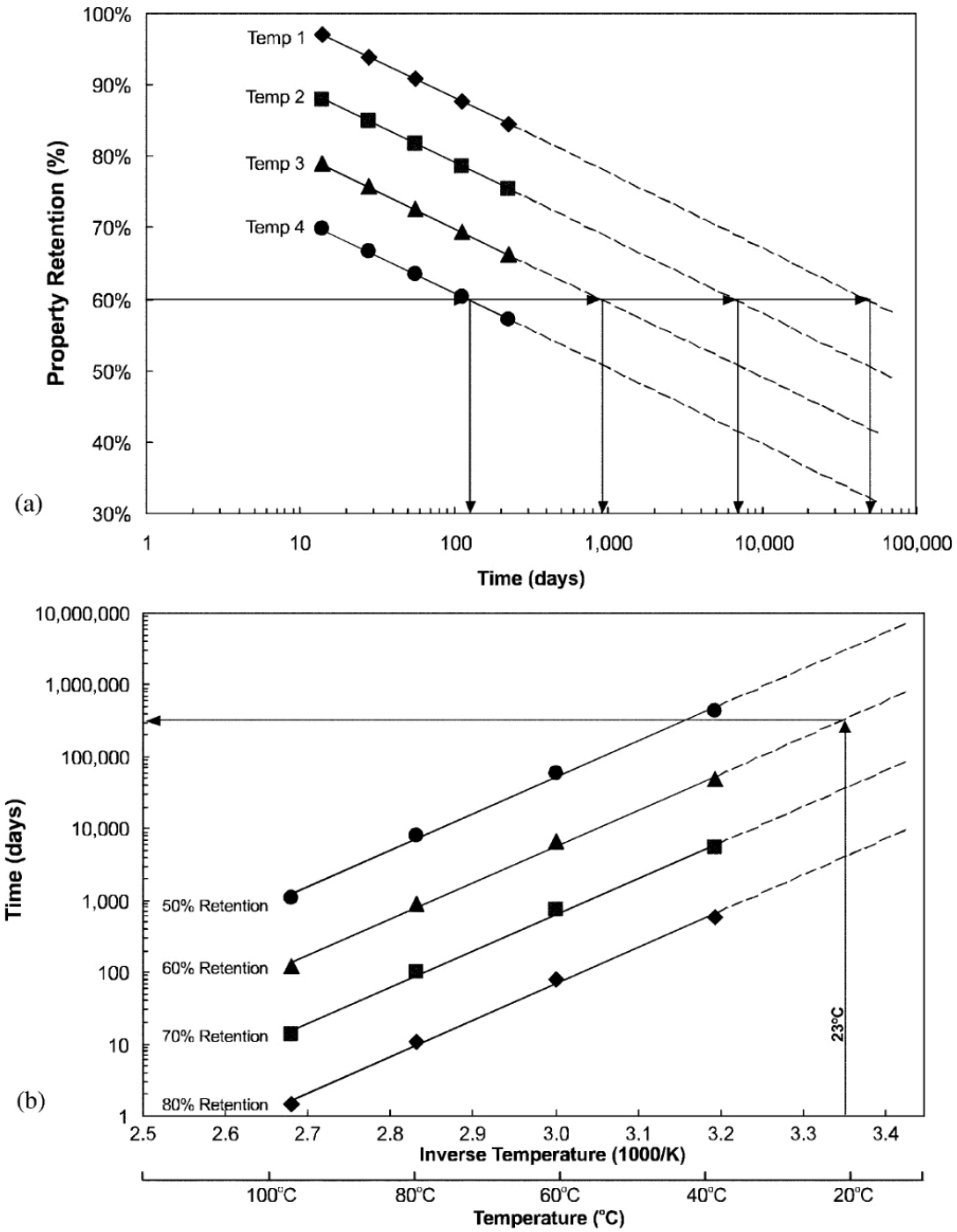

Figure 2-3 (a) Plot of property retention as a function of time and (b) Arrhenius plot for service life as a function of temperature and percent of retention (Bank et al., 2003)

Karbhari and Abanilla (2007) studied the tensile, flexural, short-beam, and in-plane shear strength of CFRP laminates. The Arrhenius and Phani and Bose methods, used to predict the long-term effects, were compared, based on the accelerated aging test of specimens immersed in high-temperature water tanks (Figure 2-4), and it was concluded that the Arrhenius method is more accurate than the Phani and Bose approach.

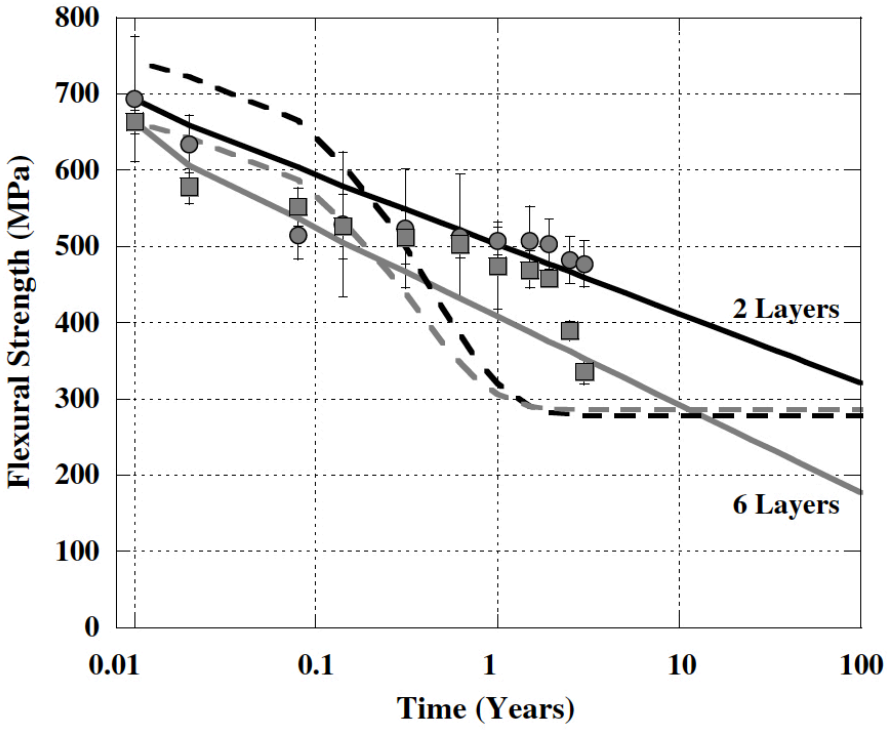

Figure 2-4 Comparison of predictions of flexural strength

(Solid line corresponds to the Arrhenius method, and the dashed line corresponds to the Phani and Bose method.) (Karbhari and Abanilla, 2007)

2.4 FRP Externally Bonded to Concrete Structure

Extensive research has been performed to evaluate the flexural performance of concrete structures strengthened with externally bonded FRPs systems (Al-Rousan et al., 2018; Bahn and Harichandran, 2008; Chajes et al., 1994; Esfahani et al., 2007). Karbhari

and Seible (2000) and Pendhari et al. (2008) reviewed the applications of FRP composite materials used primarily for strengthening and retrofitting beams, slabs, columns, pipelines, and decks subjected to regular and seismic loads. Chajes et al. (1994) studied the flexural performance of reinforced concrete beams strengthened with externally bonded aramid, E-glass, and graphite FRP composites, using the four-point bending test. As shown in Figure 2-5, the flexural strengths were increased by 46%, 41%, and 43%, respectively.

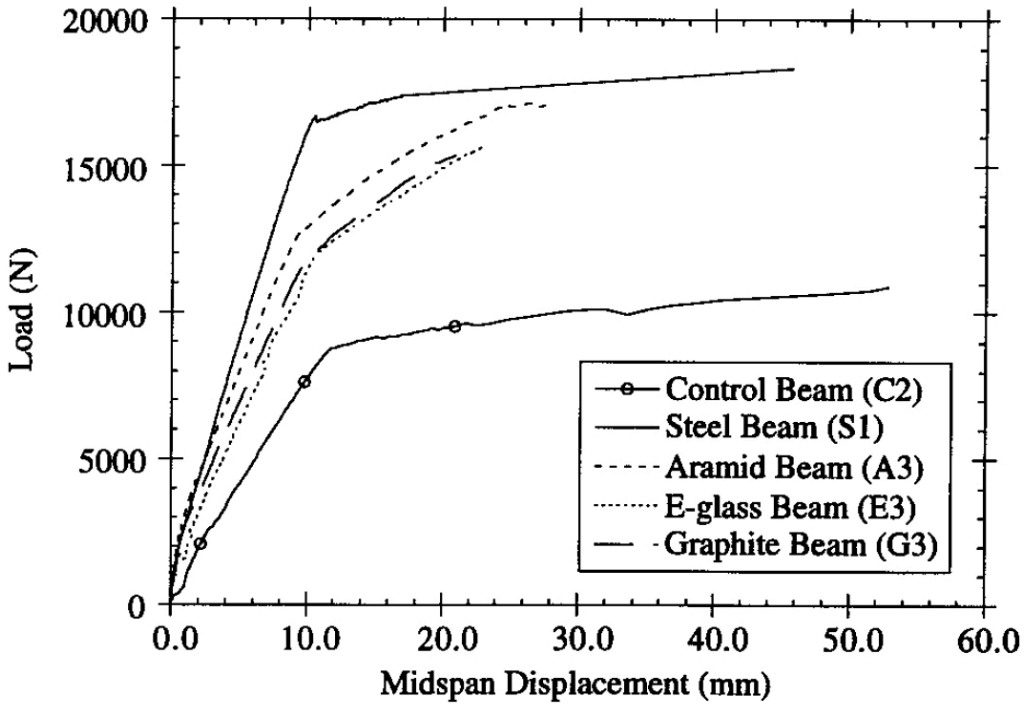

Figure 2-5 Load versus midspan deflection plot for typical beams (Chajes et al., 1994)

Al-Rousan et al. (2018) investigated the behavior of 72 plain concrete beams anchored with CFRPs of various dosages of macro discontinuous structural synthetic fiber (DSSF) and different lengths of CFRP sheets. The results showed that the CFRP improved the ultimate load-carrying capacity from 8% to 22%.

2.5 Durability of FRP Externally Bonded to Concrete Structure

Many studies have been conducted, using accelerated aging tests to examine the long-term behavior of bonded FRP composite systems. Choi et al. (2011) summarized the results from previous studies regarding the durability of interfacial bonding for CFRP bonded to concrete using epoxy adhesives subjected to water exposure (Table 2-2). They also investigated various FRP systems designed for external reinforcement of concrete under various environmental conditions. Their results showed that the hygrothermal performance was not consistent among the different FRP systems, and the epoxy resin used in the composite highly affected the durability.

Table 2-2 Effects of continuous water exposure on the durability of epoxy/concrete or FRP bond strengths (adopted from Choi et al., 2011)

Materials	Exposure conditions	Testing	Results
CFRP wet lay-up on concrete	Immersion/ 3-8 weeks	Modified double cantilever beam	Dry specimens failed cohesively, wet specimens failed adhesively, 35–75% loss in interfacial fracture toughness (Wan et al. 2006)
CFRP wet lay-up on mortar	Immersion/ 60 days	Modified peel test	10–20% decrease in critical energy release rate, fracture mode changes from primarily cohesive to adhesive (Karbhari et al. 1997)
Pre-cured CFRP bonded with epoxy	100% RH, 23 °C, 50 °C 0-56 days	Shear/peel tests	Dry specimens failed cohesively, wet specimens failed adhesively, 50–60% loss in fracture toughness (Au and Buyukozturk 2006)
CFRP wet lay-up on mortar	Immersion/ 60 days	Four-point flexure	24–33% loss in strength (Karbhari and Engineer 1996)

Deng, et al. (2010) studied flexure and direct tension behavior of bonded CFRP materials, using specimens submerged in a water bath subjected to an elevated temperature. They discovered that the bond between the concrete surface and the adhesive material is the weakest region for externally applied CFRP due to the effects of water and elevated temperatures.

Another study was done by Subhani, et al. (2016) that showed that the bond between CFRP and concrete could be improved by adding rubber to the epoxy. They also studied the strength deterioration of bonds subjected to wet-dry cycles of saltwater. Their findings showed that in a marine environment, the modified epoxy had a higher value in strength, in terms of ductility, than normal epoxy.

Previous studies indicated that hygrothermal conditions are deleterious to the durability of CFRP concrete bonded systems. Karbhari and Engineer (1996) examined the effects of short-term environmental exposures on reinforced concrete beams externally strengthened with CFRP. The reduction of failure load was 24% after immersion in fresh water at an ambient temperature for 60 days. Shrestha et al. (2016) studied the durability performance of the concrete CFRP bonded system after it had been immersed in water at 20 °C for periods up to 18 months and found that the average direct tension strength obtained from pull-off tests was reduced by 19 to 41%. However, Pallempati et al. (2016) evaluated the performance of the CFRP's strengthening of several concrete bridge components, using the pull-off test, and concluded that age-based environmental degradation is not a significant factor in the strength of the CFRP-epoxy-concrete interface.

A case study conducted by Allen & Atadero (2012) evaluated the long-term durability of externally bonded FRP via field assessments. They collected FRP samples from the Castlewood Canyon Bridge in Colorado, a concrete arch bridge shown in Figure 2-6, eight years after the FRP was initially attached. The authors conducted an on-site inspection for delaminations between the concrete surface and the FRP, using non-destructive testing of acoustic sounding and thermographic imaging. They performed destructive testing, using pull-off tests, to evaluate the bond strength between the concrete surface and the FRP and discovered many deteriorations and debonding regions. They cut some of the debonded regions out of the structure and evaluated them in the laboratory, using a tensile test. The results were compared with the ultimate tensile strength of the manufacturer, and the mean tensile strength from the field data was higher than that of the manufacturer's. However, by using the statistical equation of the mean of tensile strength minus 3 standard deviations, the field samples were about 61% below the designed ultimate strength of the manufacturer.

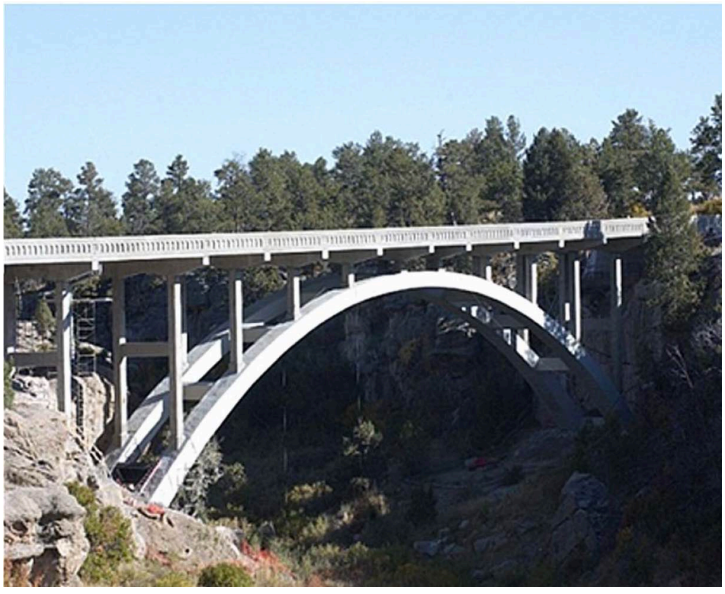

Figure 2-6 Castlewood Canyon Bridge (Allen and Atadero, 2012)

A similar study was conducted by Mata and Atadero (2014) to evaluate the FRP concrete bond, using the pull-off test. The results were highly variable, which might be attributed to their being localized and dependent on parameters that may have had little influence on the bond. The predominant failure mode was the bonding epoxy failure at dolly, Mode A, which occurred in 60% of the control samples.

Silva and Biscaia (2008) studied the effects of cycles of salt fog, temperature, moisture, and immersion in saltwater on the bending response of beams externally strengthened with CFRP and GFRP. The ultimate capacity of the GFRP beams showed a gain of 21% at 10,000 hours for immersed specimens, which can be attributed to an increase in the tensile strength of the concrete and post-curing of the polymers. Pull-out tests of CFRP concrete beams showed an increase of strength for the salt fog cycles, as shown in Figure 2-7, which can be attributed to the wet curing associated with an elevated temperature of 35 °C.

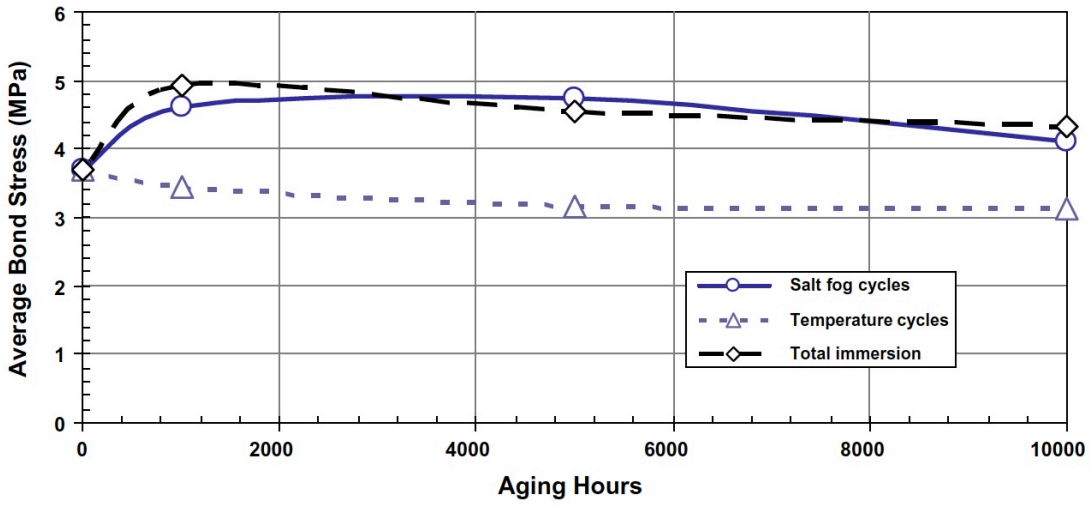

Figure 2-7 Evolution of the maximum average bond stress for each artificial aging period considered (Silva and Biscaia, 2008)

Tatar and Hamilton (2016) compared the durability of the FRP-concrete bond for laboratory and field samples, using the notched beam three-point bending and direct tension pull-off tests. The laboratory specimens were subjected to accelerated conditioning, including immersion in 30 and 60 °C water for eight weeks, while field exposure consisted of test patches on the girders of the Sunshine Skyway Bridge in Tampa Bay, Florida. All of the laboratory specimens showed a reduction in bond strength throughout the exposure period; however, none of the field specimens showed significant degradation, indicating that the rate of degradation was extremely slow.

Karbhari and Ghosh (2009) investigated the durability of the bond between the FRP and the concrete substrate under environmental exposure conditions, including ponding at different humidity levels, exposure to a freeze condition of -18 °C, and immersion in water and saltwater. Moisture uptake, tensile strength, and direct tension pull-off testing of the FRP concrete assembly were used to characterize the FRP systems. It was noted that immersion in saltwater caused the highest level of degradation of direct tension strength.

A study to evaluate the environmental reduction factor, C_E, prescribed in ACI 440.2R-17 (2017) was conducted and proposed by Cromwell, et al. (2011). They investigated the behavior of three FRP systems (CFRP plate, CFRP fabric, and GFRP fabric) that had been subjected to nine environmental conditions. The environmental conditions, with various durations and cycles, included water, saltwater, alkaline conditions, dry heat, diesel, weathering, freeze-heat, and freeze-thaw. The effects of the environmental conditions were evaluated by using four standard test methods: tension,

short beam shear, bond to concrete, and beam flexure. Table 2-3 lists the current and revised approaches to the environmental reduction factor, C_E, from ACI 440.2R-17 (2017).

Table 2-3 Reduction factors for environmental exposure (Cromwell et al., 2011)

		CFRP plate	CFRP fabric	GFRP fabric
Reported study	Tension modulus	0.96	0.90	0.94
	Tension strength	1.00	0.92	0.82
	Bond capacity	0.91	0.60	0.52
Recommendations	Material properties	0.90	-	0.80
	Bond capacity	0.90	0.50	-

2.6 Finite Element Modeling of FRP-Strengthened Concrete Structure

The simulation of FRP bonded externally to a concrete structure, using finite element modeling (FEM), is a powerful technique for validating the experimental tests and studying the effects of other parameters. Using the commercial software, ABAQUS, Obaidat et al. (2010) created a three-dimensional model of a concrete beam strengthened with CFRP laminate, loaded under four-point bending. The model results were compared with the experimental data, and good agreements were observed regarding the load-displacement response, debonding failure, and crack pattern.

Using FEM, Lu et al. (2005) evaluated the results of 253 pull tests on simple FRP-to-concrete bonded joints. They also proposed expressions for maximum shear stress, τ_{max}, and the interfacial fracture energy, G_f, as shown in Eqs. (2-4) and (2-5), respectively.

$$\tau_{max} = 1.5\,\beta_w\,f_{ct} \tag{2-4}$$

$$G_f = 0.308\,\beta_w^2\,\sqrt{f_{ct}} \tag{2-5}$$

where: f_{ct} = the concrete tensile strength,

β_w = the expression of the width ratio factor and given by Eq. (2-6):

$$\beta_w = \sqrt{\frac{2.25 - \frac{b_f}{b_c}}{1.25 + \frac{b_f}{b_c}}} \tag{2-6}$$

where: b_f = the CFRP sheet width, and

b_c = the concrete width.

Obaidat et al. (2013) evaluated the parameters of the bond between FRP and concrete structures strengthened in flexure, based on nonlinear finite element results and other experimental results from the literature. The FEM parameters were shear strength, initial stiffness, and fracture energy of the FRP-concrete interface; no geometry-related correction coefficients were considered. By using multiple regression, they obtained equations of material parameters suitable for use in the FEM model. The initial stiffness, K_0, was utilized by Eq. (2-7):

$$K_0 = 0.16\frac{G_m}{t_m} + 0.47 \tag{2-7}$$

where: t_m = the matrix thickness, and

G_m = shear modulus of the matrix.

The interfacial fracture energy, G_f, and the maximum shear stress, τ_{max}, were obtained by Eqs. (2-8) and (2-9), respectively:

$$G_f = 0.52 \times f_{ct}^{0.26} \times G_m^{-0.23} \quad (2\text{-}8)$$

$$\tau_{max} = 1.46 \times f_{ct}^{1.033} \times G_m^{0.165} \quad (2\text{-}9)$$

Gawil et al. (2020) developed a three-dimensional extended finite element model (X-FEM) to study the behavior of concrete beams and columns subjected to temperatures of 25, 100, and 180 °C. The X-FEM offers significant benefits in numerical modeling in terms of crack propagation. As shown in Figure 2-8, X-FEM simulated the first rupture of CFRP when the external load reached 99.63% of the peak load, followed by the final stages of loading.

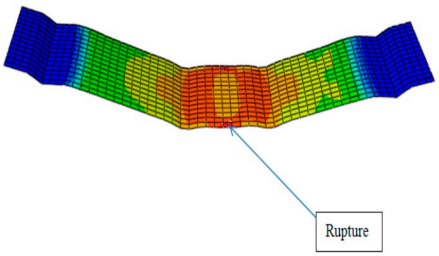

The first rupture of CFRP started when the external load reached 99.63% of the peak load.

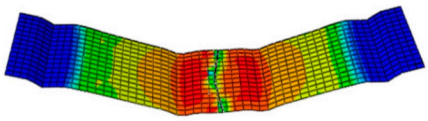

The external load reached 99.64% of the peak load.

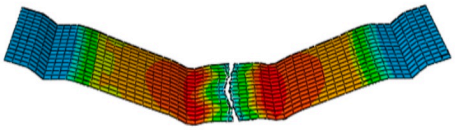

The external load reached 99.65% of the peak load.

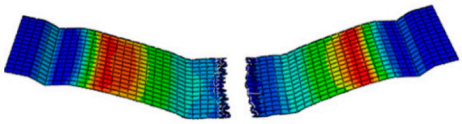

At peak load.

Figure 2-8 CFRP rupture simulation of CFRP-strengthened concrete beams at room temperature (Gawil et al., 2020)

Chapter 3. Experimental Program

3.1 CFRP Laminate Preparation

A typical CFRP wet lay-up process that consisted of a woven unidirectional carbon fiber fabric (SikaWrap Hex 117C) and matrix resin was selected for the laminate preparation. The matrix, Sikadur® 330, is a two-part epoxy with a mixing ratio of component 'A' to component 'B' of four-to-one by weight. Table 3-1 lists the properties of the dry carbon fiber, epoxy, and CFRP laminate, as provided by the manufacturer's product sheet.

Table 3-1 Properties of materials

Material	Tensile Strength		Young's Modulus		Failure Strain (%)
	(MPa)	(ksi)	(GPa)	(ksi)	
Dry carbon fiber	3793	550	234	33939	1.5
Matrix (epoxy)	33.8	4.90	4.5	653	1.2
CFRP laminate	724	105	56.5	8195	1

A wooden frame was fabricated to grip and stretch the carbon fiber fabric, as shown in Figure 3-1. The two-part epoxy was mixed thoroughly for 5 minutes with an electric mixer at a speed of 320 rpm at 23 °C, as shown in Figure 3-2. The epoxy resin was applied with a roller and slipper to both surfaces of the carbon fiber laminate to form the CFRP and to ensure that the carbon fiber was fully saturated with the resin (Figure 3-3). The epoxy resin was cured for three days in the ambient temperature. Coupons were

fabricated, using an electric band saw that cut a 254 mm (10 in.) long and 14.5 mm (0.57 in.) wide cross-section, as shown in Figure 3-4. Nearly 100 specimens were selected for testing the tensile strength, as shown in Figure 3-5. The detailed geometry of the CFRP coupon is illustrated in Figure 3-6. The standard tensile coupon test, as per ASTM D3039 (ASTM, 2017), was conducted to measure the material properties of the CFRP samples. Five identical specimens per test condition were tested.

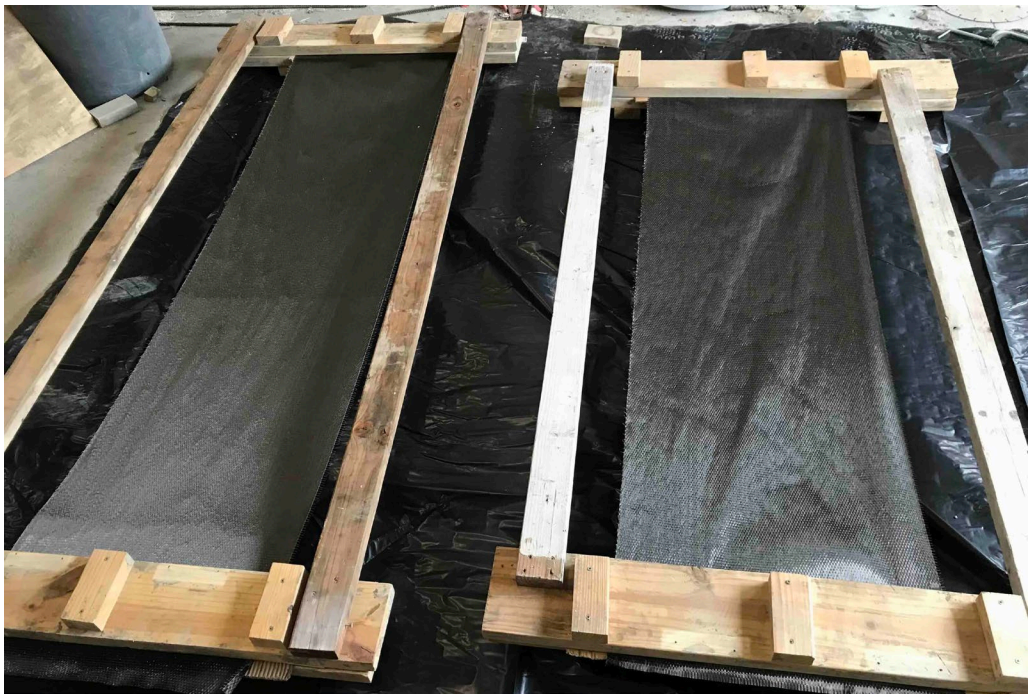

Figure 3-1 CFRP sheet gripped by the wooden frame

Figure 3-2 Mixing the two-part epoxy resin

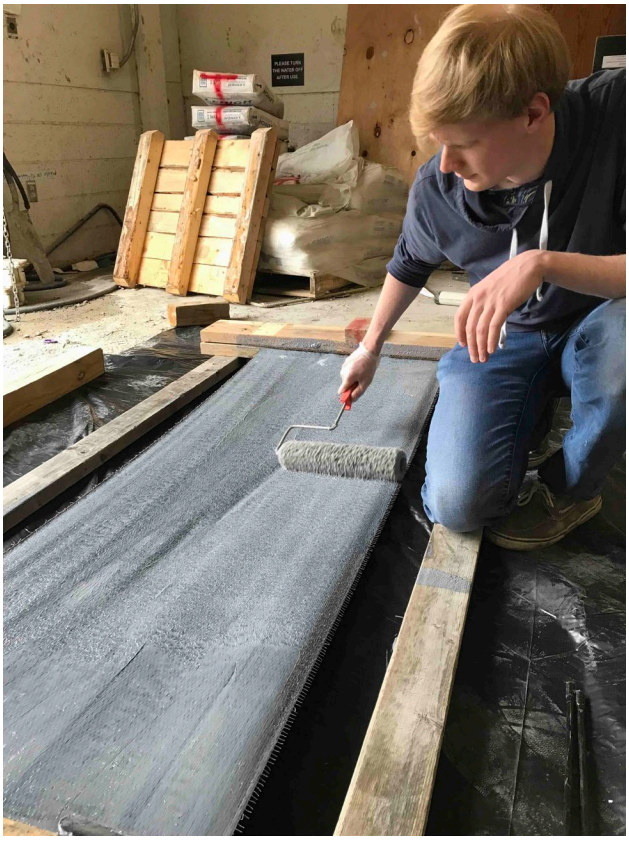

Figure 3-3 Applying the epoxy to both sides of the carbon fiber sheet with a roller

Figure 3-4 Cutting the CFRP laminate into strips (coupons)

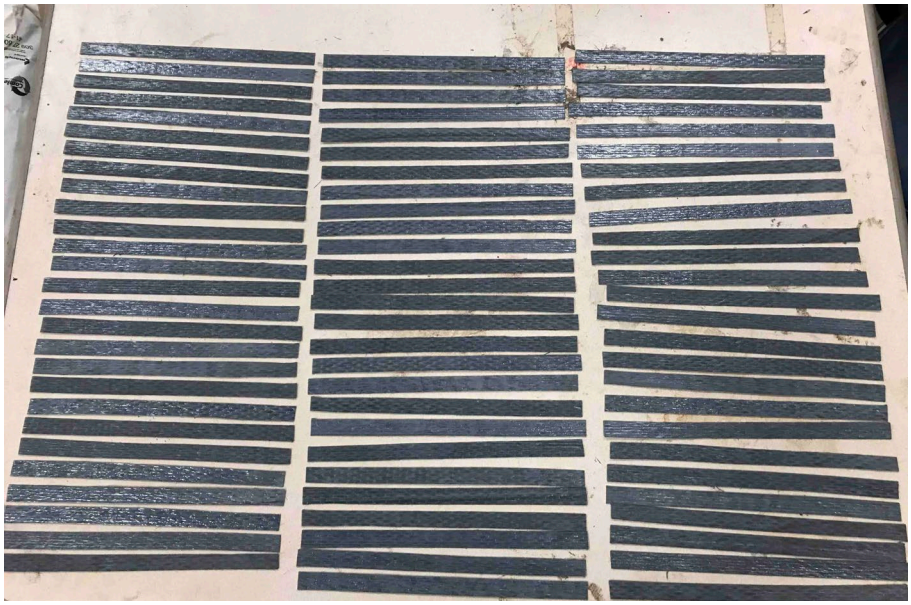

Figure 3-5 Specimens of CFRP laminate (coupons)

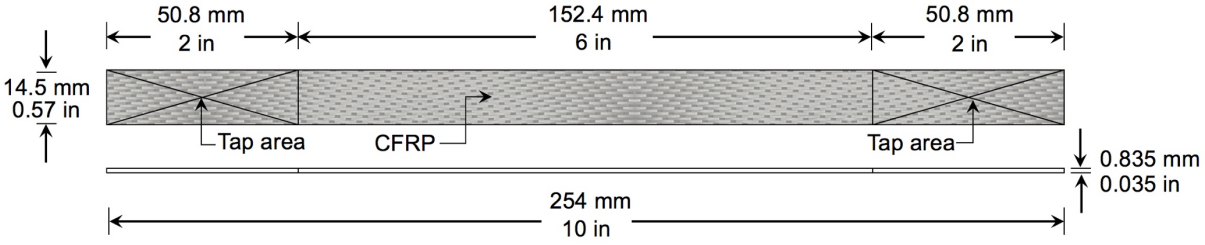

Figure 3-6 Geometry of CFRP sample (coupon)

3.2 Environmental Exposure of CFRP Laminate

The environmental exposure protocol, adopted from a model proposed by Bank et al. (2003), consisted of 80 specimens that were designed in an effort to discover the degradation mechanisms of wet lay-up CFRP under an environmental condition. The variables considered in the test were exposure conditions and duration. To avoid reaching the viscous state of the epoxy resin, a maximum conditioning temperature of 60 °C was considered as 80% of the nominal glass transition temperature (Bank et al., 2003). Since implementing the Arrhenius theory accurately requires that at least three different temperatures be used to obtain the degradation data (Wang et al., 2014), after being preconditioned, the FRP samples were immersed in tap water at 23, 45, and 60 °C.

Water boiler tanks were used for environmental conditions of 45 and 60 °C with a temperature variation range of ± 3 °C, as demonstrated in Figure 3-7. Five values for each regime were averaged for the sake of error reduction. Specimens were placed in water tanks for up to 32 weeks and were removed for testing at intervals of 28, 56, 84, 112, and 224 days, as listed in Table 3-2.

(a) (b)

Figure 3-7 Accelerated aging: (a) three water tanks with different temperatures, (b) inside view of 45 °C water tank with CFRP coupons

Table 3-2 Experimental program of the accelerated aging test of CFRP laminate

Environmental exposure	Duration (day)	No. of samples
Immersion in the water at 23 °C, denoted as room temperature (RT)	28, 56, 84, 112, and 224	25
Immersion in the water at 45 °C, denoted as moderate temperature (MT)	28, 56, 84, 112, and 224	25
Immersion in the water at 60 °C, denoted as high temperature (HT)	28, 56, 84, 112, and 224	25
Control sample	-	8
Total No. of samples		83

3.3 Experimental Test of CFRP Laminate

All specimens were removed from their environmental conditions after a specific period of exposure, then the width and thickness of each specimen were measured with a digital micrometer with 0.001 mm (3.94 x10^{-5} in.) resolution. A resistance-based foil

strain gauge, Tokyo-Sokki FLA-5-350, with a resistance of 350 Ω and a gauge length of 5 mm (0.2 in.) was installed, using a cyanoacrylate-based epoxy, Tokyo-Sokki CN adhesive, to the mid-length of each CFRP specimen for capturing the strain response, as shown in Figure 3-8.

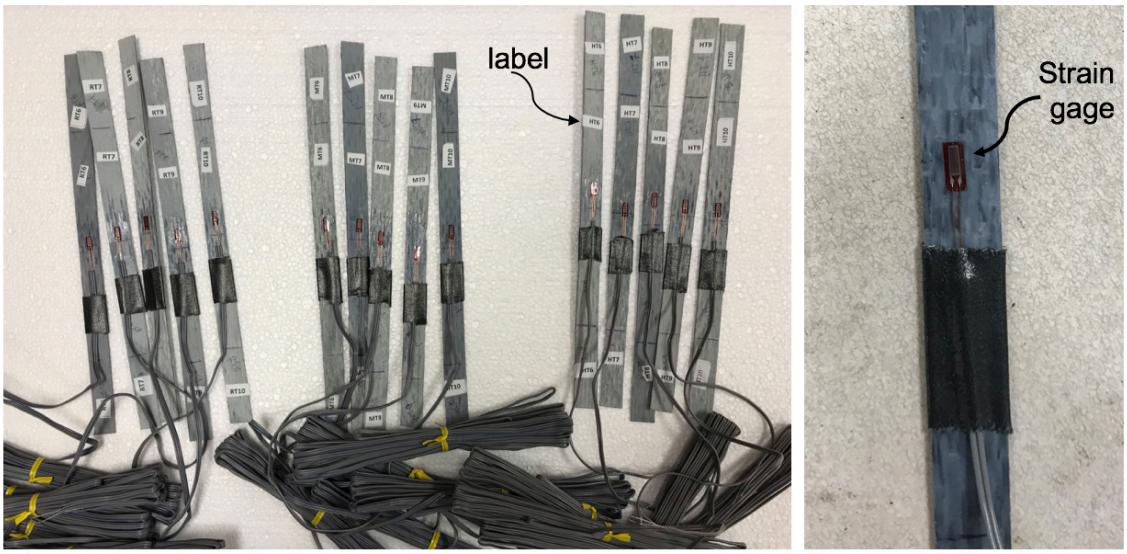

Figure 3-8 CFRP specimens: (a) five labeled specimens of each environmental condition, (b) close view showing the stain gage attached to CFRP specimen

All coupon specimens were tested for tensile properties in accordance with ASTM D3039 (ASTM, 2017). The test was conducted using the material test system MTS 810 at a loading rate of 1 mm/min (0.04 in/min) and was monitored by the MultiPurpose TestWare MPT application. The load and displacement data were acquired using the MTS FlexTest® 40 data control acquisition system. Strain gage wires were connected to the data acquisition system, Tokyo Sokki DS750, and monitored using a Tokyo Sokki DS 50A data logger at a frequency of 8 Hz. The schematic view of the test setup is presented in detail in Figure 3-9.

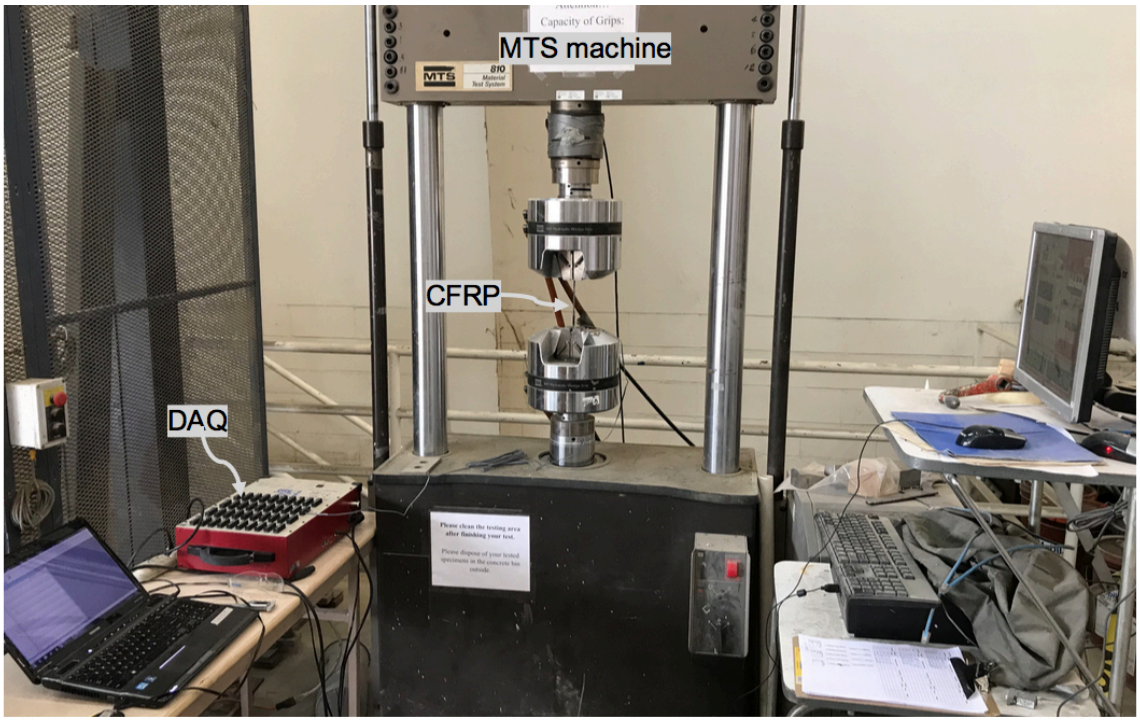

(a) Overview of tensile test set-up showing the apparatus of the practical test

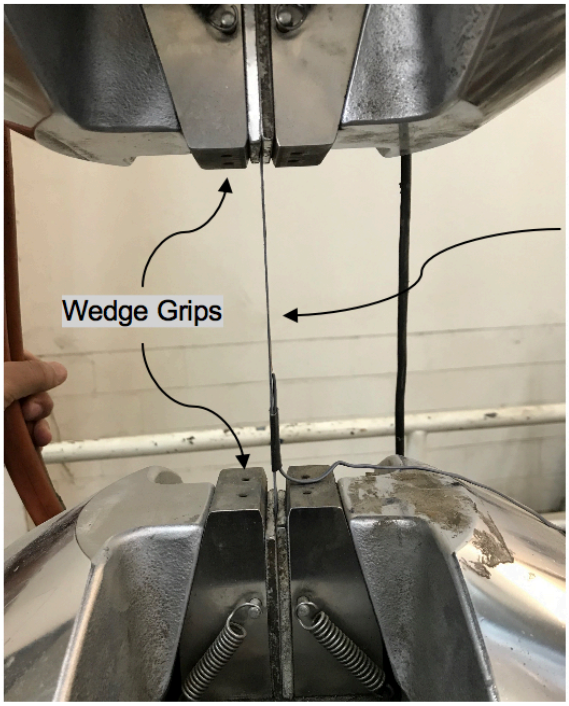

(b) CFRP specimen with a straight alignment installed between wedge grips

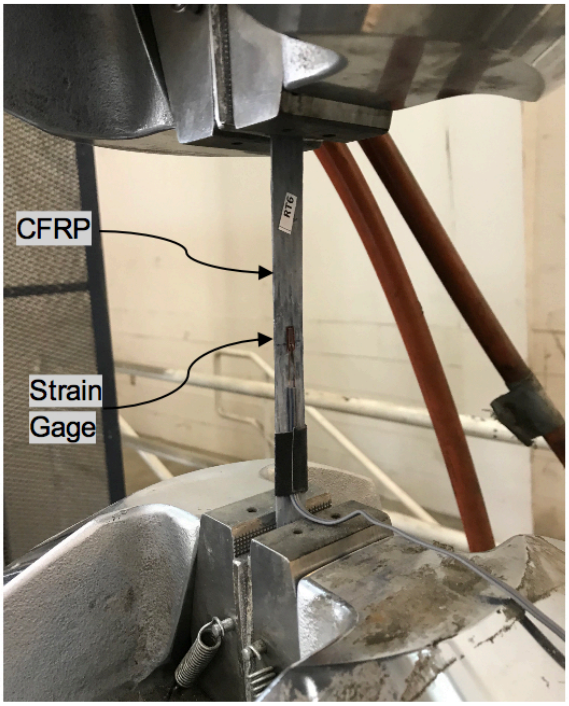

(c) CFRP specimen before conducting the tensile test

Figure 3-9 Tensile test set-up

3.4 Preparation of CFRP Concrete Bonded Beams

3.4.1 Experimental Materials and Specimens

Concrete beams with dimensions of 152.4 x 152.4 x 533.4 mm (6 x 6 x 21 in.) were fabricated based on ASTM Standard C78 (ASTM, 2018), and cylindrical molds with a diameter of 101.6 mm (4 in.) and height of 203.2 mm (8 in.) were used to produce column specimens in accordance with ASTM C39 (ASTM, 2016), as shown in Figure 3-10. Ready-mix normal weight concrete with a target 28-day compressive strength of 20.65 MPa (3 ksi) was used for all the beam specimens. The concrete casting procedures began with conducting the slump test to determine the consistency and workability of the fresh concrete. Concrete was poured into the beam molds and spread by shovels and concrete placers, as shown in Figure 3-11(b). A mechanical vibrator was used to vibrate the concrete and prevent any imperfections, such as honeycombing, as shown in Figure 3-11(c). One hour after casting, a waterproofing agent was applied to the top of each beam to prevent moisture from evaporating. After curing for 24 hours in the molds, the concrete beams were demolded and moved to a curing room for 28 days.

Figure 3-10 Rectangular beam and cylinder molds before casting

(a) pouring the concrete into the beam molds

(b) spreading the concrete into the mold

(c) using the vibrator in each mold

(d) one hour after casting

Figure 3-11 Concrete casting

The slump test was conducted before the concrete was cast to confirm the quality of the fresh concrete mix and to verify its workability and consistency. According to ASTM C143/C143M (2015), the standard concrete slump test cone is 304.8 mm (12 in.) high, the base is 203.2 mm (8 in.) in diameter, and the top is 101.6 mm (4 in.) in diameter. The large diameter of the slump cone mold was positioned on a flat, rigid, and smooth plate surface. The fresh concrete was poured and compacted into the cone mold in three layers. Each layer was stroked 25 times with a round tamping rod of 16 mm (0.625 in.) diameter. After pouring the concrete, the cone mold was lifted and the concrete was

permitted to slump. Then, the slump value, which is the vertical distance between the original and displaced position of the middle of the top surface of the concrete, was measured, as shown in Figure 3-12.

(a) (b)

Figure 3-12 The slump test: (a) compacting the fresh concrete by tamping rod, (b) measuring slump value

3.4.2 Compressive Strength

To check the compressive strength of the concrete beams, concrete cylinders with a diameter of 101.6 mm (4 in.) and height of 203.2 mm (8 in.) were cast from the same concrete mix that was used to cast the beams. The compressive strength tests were conducted on specimens 28 days after casting, which was the same day a flexural test was performed on each beam, in accordance with ASTM C39 (ASTM, 2016). The cylinder specimens' ends were prepared by using molten sulfur mortar to form bonded caps, as shown in Figure 3-13. The capping method created a smooth, flat, perpendicular surfaces on the applied axial load, so that the applied load was uniformly distributed on the two ends. Figure 3-14 shows the capped concrete specimen inside the concrete compression

machine, before and after failure. To calculate the compressive strength of the specimen, the maximum load carried by the specimen was divided by the cross-sectional area of the specimen, as detailed in Table 3-3.

Figure 3-13 Capping of concrete cylinders

(a) (b)

Figure 3-14 Compression test: (a) concrete cylinder inside the compression machine, (b) concrete cylinder after failure

Table 3-3 Concrete compression test 28 days after casting

Sample	Diameter, mm (in)	Height, mm (in)	Area, mm^2 (in^2)	Fail load, kN (kips)	Compressive Strength on 28^{th} day, MPa (ksi)
1	101.6 (4)	203.2 (8)	8,110 (12.57)	136.11 (30.6)	18.32 (2.66)
2	101.6 (4)	203.2 (8)	8,110 (12.57)	160.42 (36.06)	16.79 (2.44)
3	101.6 (4)	203.2 (8)	8,110 (12.57)	148.35 (33.35)	19.79 (2.87)

3.4.3 Surface Preparation

After 28 days of curing, the concrete beams were moved outside for surface preparation. According to Santos and Júlio (2013), the International Concrete Repair Institute (ICRI) developed a visual inspection for classifications of surface textures based on the distance from the peaks of the surface to the valleys. The ICRI classified surface textures into nine concrete surface profiles (CSP 1-9), as shown in Figure 3-15, and found that surface roughness ascends with the CSP number. For example, CSP 1 is almost flat, but CSP 9 is rougher, and the span between 1 and 9 becomes progressively rougher. Level 3 of the CSP was achieved by sandblasting, as defined by ICRI. The technician reached the desired surface roughness by exerting high air pressure with sand, as presented in Figure 3-16. After being sandblasted, the concrete beams were cleaned of any dust or contaminants by applying high air pressure.

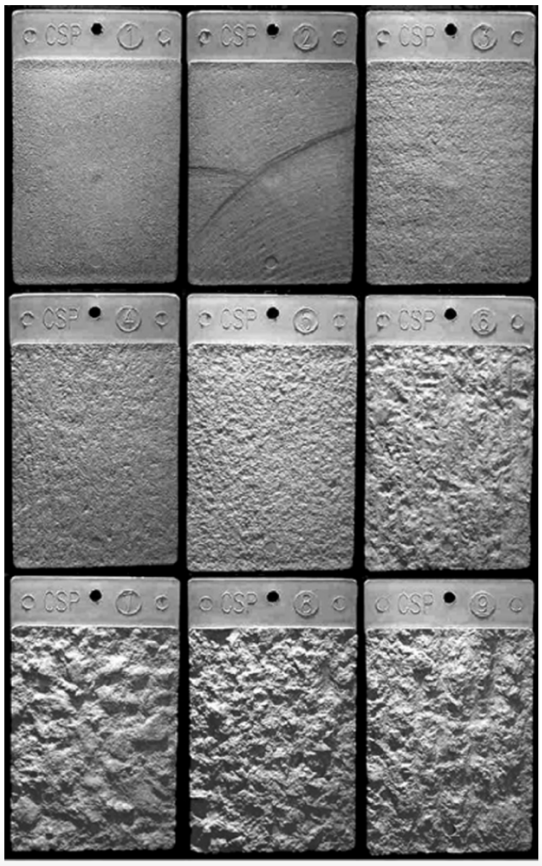

Figure 3-15 Concrete surface profile by ICRI (Santos & Júlio, 2013)

(a) (b)

Figure 3-16 Sandblasting: (a) The technician sandblasts the top surface of the concrete beams, (b) top concrete beam of (CSP 3) with corresponding to ICRI

3.4.4 CFRP Application

After the concrete beams were cleaned to remove any dust or contaminants, they were placed inside a chamber at 25 °C to process the CFRP application. The system chosen for the CFRP application was a typical wet lay-up process that consisted of a woven unidirectional carbon fiber fabric of 300 gsm (9.0 osy). As provided by the manufacturer's product sheet, the dry fibers have a nominal strength, modulus, and density of 3793 MPa (550 ksi), 234 GPa (34,000 ksi), and 1.80 g/cm^3 (0.065 lb/in^3), respectively. The dimensions of the CFRP laminate to be applied to the tension side (bottom) of the concrete beam were 152.4 x 381 mm (6 x 15 in.); the dimensions of the CFRP laminate to be applied to the side of the concrete beam were 152.4 x 152.4 mm (6 x 6 in.). Scissors were used to cut the dry fiber sheets to the desired dimensions, as shown in Figure 3-17.

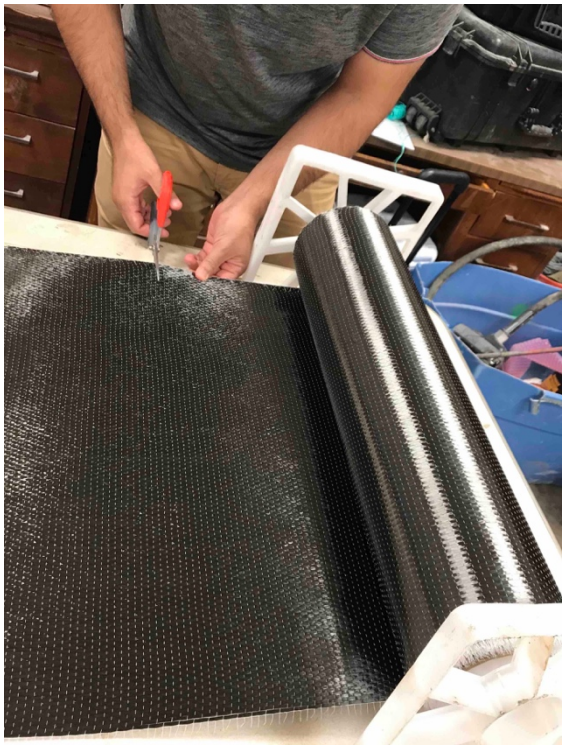

Figure 3-17 Cutting the CFRP fiber sheet

The matrix, Sikadur® 330, is a two-part epoxy with a mixing ratio of component ‘A’ to component ‘B’ of 4:1 by weight. It was mixed thoroughly for 5 minutes in an electric mixer at a speed of 320 rpm at 25 °C, as shown in Figure 3-18. The 7-day tensile strength, ultimate elongation, flexural strength, and flexural modulus were 33.8 MPa (4,900 psi); 1.2%, 60.6 MPa (8,800 psi); and 3489 MPa (506 ksi), respectively. After the epoxy resin was mixed, it was applied with a roller to both sides of the dry carbon fiber sheet, to ensure that the carbon fiber was fully saturated. The epoxy resin was also applied to the desired concrete beam surfaces with a roller, as illustrated in Figure 3-18. Next, the carbon fiber laminate was laid down on the surface of the concrete beam, and an aluminum roller and wide plastic scraper were used to release any entrapped air bubbles or voids between the CFRP laminate and the concrete surface.

Figure 3-18 Mixing the epoxy resin

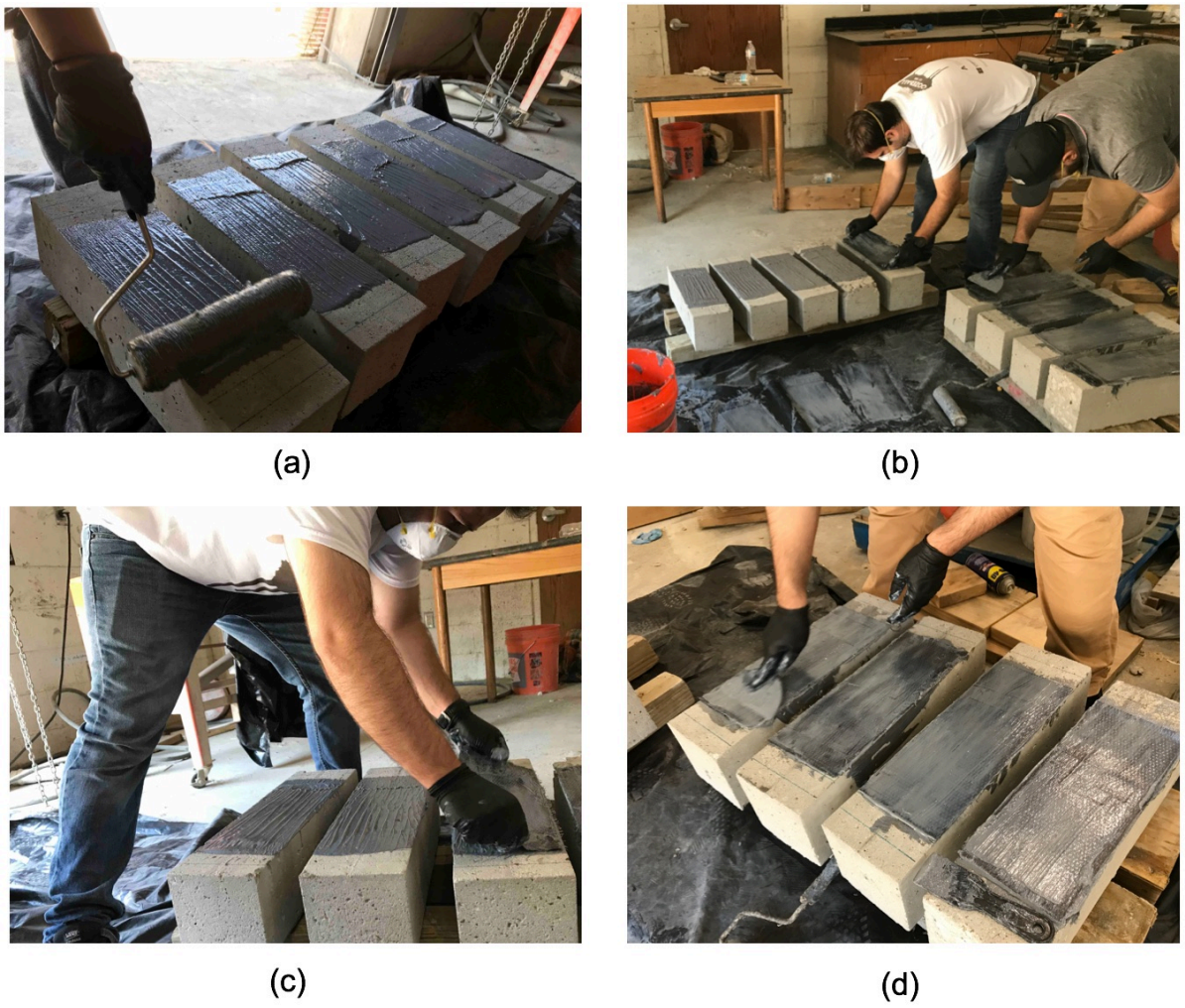

Figure 3-19 CFRP application: (a) applying the epoxy to the top surface of concrete beam, (b and c) applying the CFRP fiber sheet to the designed location, and (d) smoothing the surface and releasing any voids with the scraper

The freshly bonded concrete beams were cured for 7 days inside the chamber at 25 °C (Figure 3-20), before being moved to the environmental condition test, as described in the next section.

Figure 3-20 Concrete beams after applying the CFRP

3.5 Environmental Exposure of CFRP-Concrete-Bonded Beams

A total of 14 specimens were prepared to investigate the degradation mechanisms of CFRP bonded to concrete beams under an environmental condition. The variables considered in the test were exposure conditions and duration. Once the samples were preconditioned, they were exposed to three different environments: immersion in tap water at 23, 45, and 60 °C. To avoid reaching the viscous state of the epoxy matrix, a maximum conditioning temperature of 60 °C was considered as 80% of the nominal glass transition temperature (Bank et al., 2003). Elevated-temperature water tanks were used for the environmental conditions at 45 and 60 °C, with a temperature variation range of ± 3 °C. Specimens were exposed to the environmental condition for periods up 16 weeks

and were removed for testing at various intervals. Table 3-4 lists the details of the experimental program of CFRP bonded to concrete beams.

Table 3-4 Experimental program of CFRP bonded to concrete beams

Environmental Condition	Duration (days)	No. of samples
Immersion in the water at 23 °C, denoted as room temperature (RT)	28, 56, 84, and 112	4
Immersion in the water at 45 °C, denoted as moderate temperature (MT)	28, 56, 84, and 112	4
Immersion in the water at 60 °C, denoted as high temperature (HT)	28, 56, 84, and 112	4
Control sample	-	2
Total No. of Samples		14

The design of the environmental exposure test was simple, easy, and cost effective. As shown in Figure 3-21, the apparatus consisted of storage containers with lids, ceramic fiber blankets, immersion rod water heaters, pre-wired thermostat temperature controllers, and water circulation pumps. The first step was to wrap each storage container in a ceramic fiber blanket, which served as insulation material and maintained an elevated water temperature. Then, 170 liters (45 gallons) of tap water were poured into the storage container, and four concrete beam specimens bonded with CFRP were placed in it. The pre-wired thermostat temperature controller was programmed by setting the desired temperature set value and the heating differential value. The thermostat sensor that was immersed in the container controlled the socket plugs, and when the temperature became less than or equal to the temperature set value minus the

heating differential value, the system entered a heating status, and the socket plugs powered on. On the other hand, when the sensor detected that the temperature was greater than or equal to the temperature set value, the heating relay stopped working and the socket plugs powered off.

(a) Lidded storage container

(b) Ceramic fiber blanket

(c) Immersion rod water heater

(d) Pre-wired thermostat temperature controller

(e) Water circulation pump

Figure 3-21 The apparatus of environmental exposure

The 1000-watt immersion rod water heater and water circulation pump were plugged into the sockets of the pre-wired thermostat temperature controller. The immersion rod was used to heat the water when the socket plug powered on. (It can raise water temperature three degrees Celsius within an hour.) The water circulation pump, which can circulate 2000 liters/hour (528 gallons/hour), was used to move the water inside the container and to ensure a constant water temperature. Photos of the elevated-temperature water tank, specimens, and apparatus are shown in Figure 3-22.

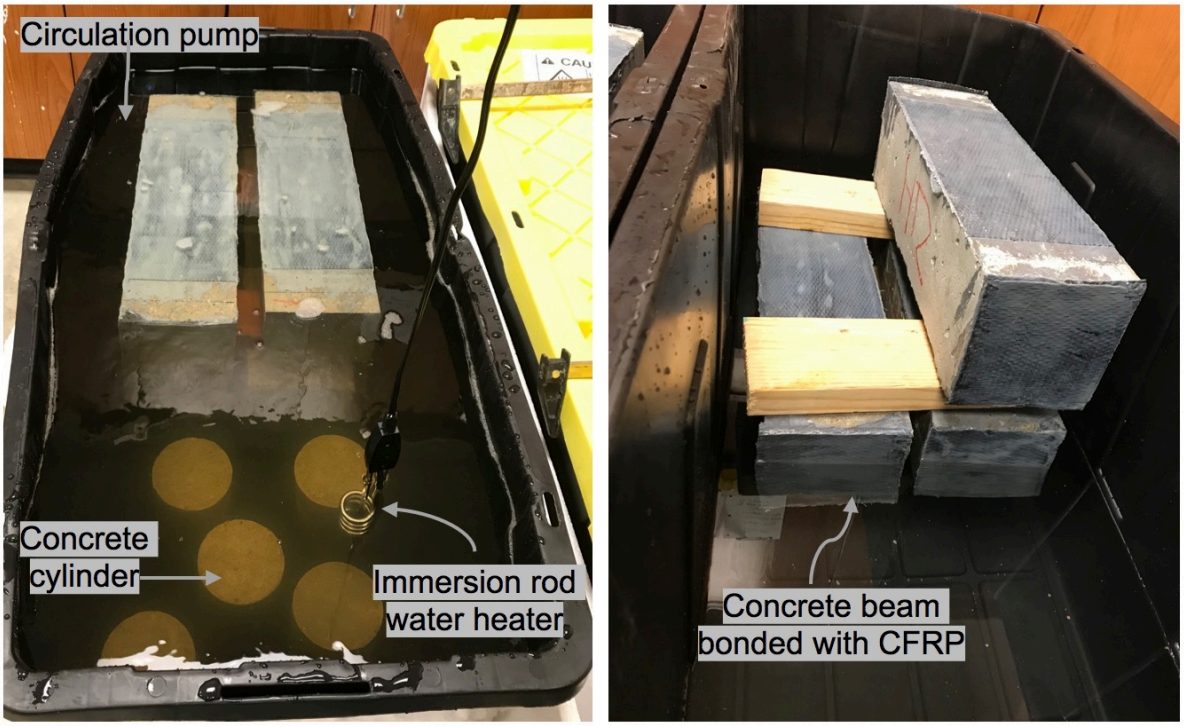

Figure 3-22 Inside view of the elevated-temperature water tanks

A lid was placed on top of the storage container to prevent water evaporation. Figure 3-23 shows the overview photo of the exterior of the elevated-temperature water tanks. Ratchet tie-down straps and bar clamps were also used. The ratchet tie-down strap was used to encircle the container and reduce the water pressure inside the container.

Two bar clamps were used on each storage container lid to fasten the lid to the container, as well as to reduce the water pressure.

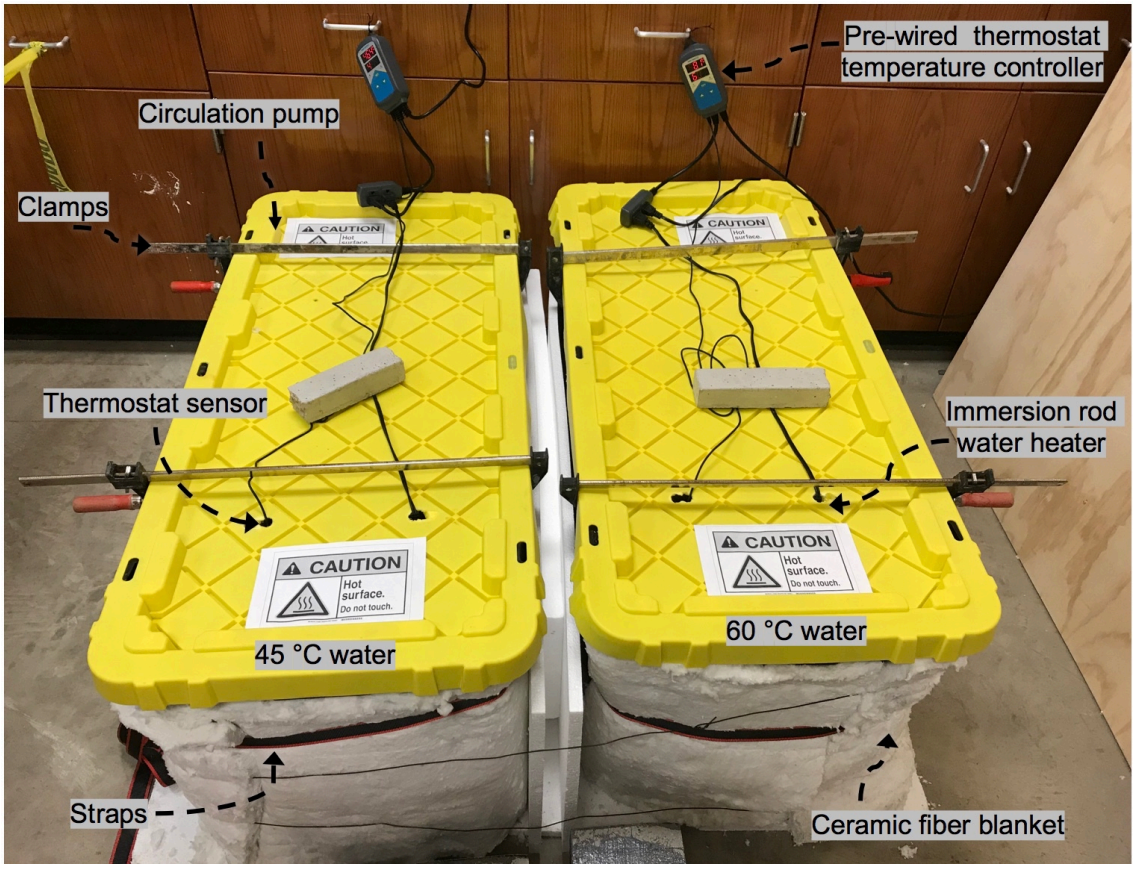

Figure 3-23 Overview photo of the exterior of the water tanks

3.6 Experimental Testing of CFRP-Concrete Bonded Beams

3.6.1 Direct Tension Pull-off Test

A pull-off test was performed in accordance with ASTM D7522 (2012) to check the bond between the concrete surface and the CFRP laminate. This test is used to determine the maximum perpendicular tension force that the concrete substrate, CFRP laminate, and adhesive can resist, as failures occur at the weakest plane (Figure 3-24). According to Pallempati et al. (2016), the durability evaluation of CFRP is beneficial to

better understanding CFRP as a concrete strengthening material. Two pull-off tests were performed for each beam sample (i.e., one test on each 152.4 x 152.4 mm [6 x 6 in.] side of the beam sample). The locations selected for the pull-off tests were on the far end of the sides, due to low stresses there and in consideration of the flexural test that would be performed on each beam after the pull-off test. Damage resulting from the pull-off test is very minor and can be ignored.

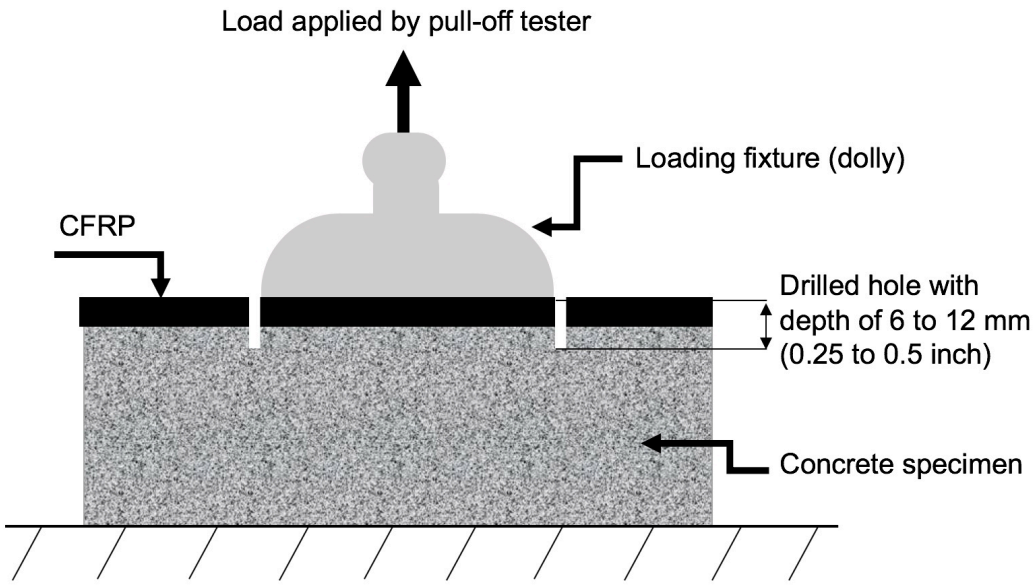

Figure 3-24 Illustration of pull-off test

The following is the procedure for the pull-off test.

1) Using a thin-walled diamond hole saw drill, make a 6 to 12 mm (0.25 to 0.5 in.) notch from the CFRP laminate into the substrate concrete, as illustrated in Figure 3-25 (a).
2) Clean the CFRP surface with a solvent before attaching the loading fixture (dolly).

3) Attach the loading fixture (dolly) to the designated region with proper adhesive material, as shown in Figure 3-25 (e).
4) Affix the grip of the pull-off tester to the loading fixture (dolly) carefully, without bending or twisting it.
5) Apply continuous loading by the pull-off tester at a rate of 1 MPa/min (150 psi/min) until a rupture occurs, as illustrated in Figure 3-25 (f).
6) Record the pull-off strength and nature of the failure mode.

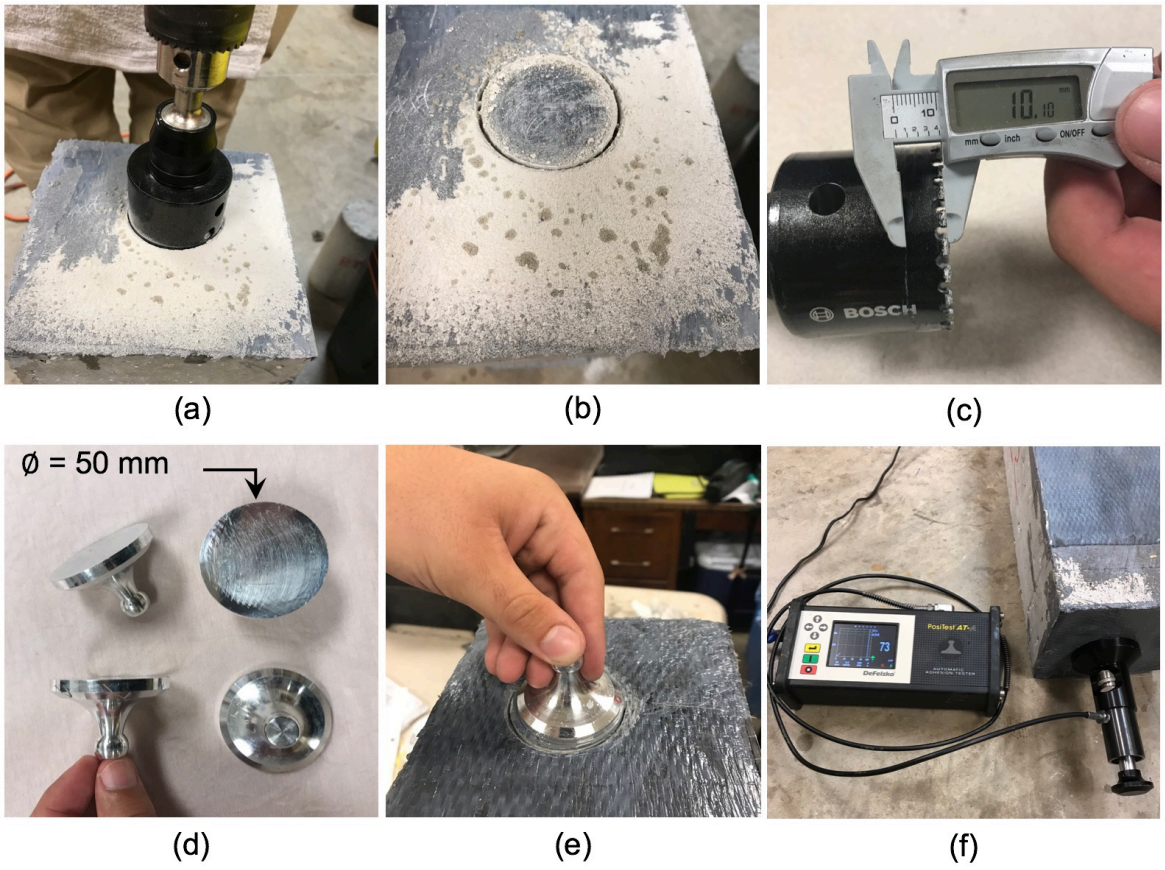

Figure 3-25 Procedures of the pull-off test

3.6.2 Flexural test

The flexural strength of the CFRP that was bonded to a concrete beam with no steel reinforcement was evaluated, using a three-point loading test in accordance with

ASTM C78 (ASTM, 2018). The geometry, loading, CFRP laminate, and support conditions are shown in Figure 3-26.

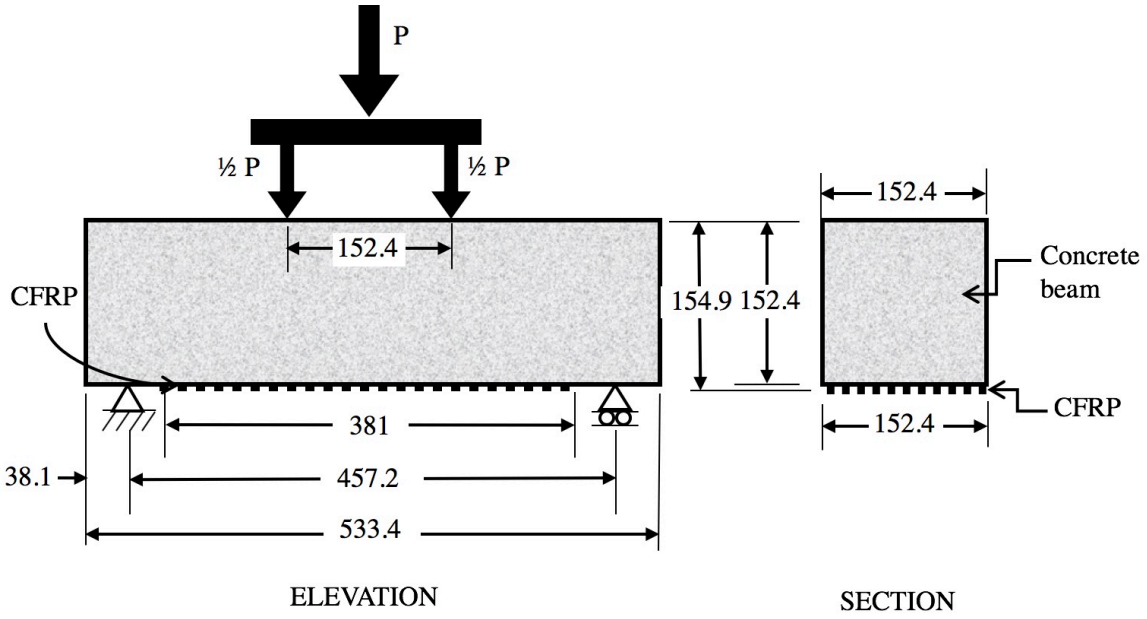

(a) Dimensions in mm

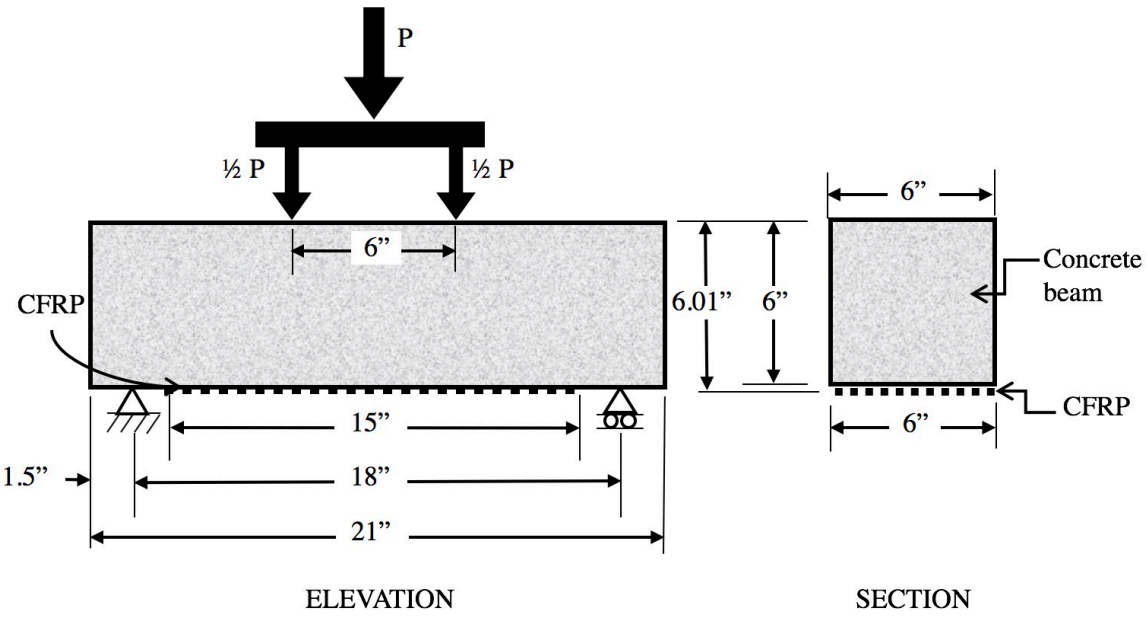

(b) Dimensions in inches

Figure 3-26 Schematic of the simply supported beam with CFRP external reinforcement

Prior to conducting the flexural test, two resistance-based foil strain gauges, Tokyo-Sokki FLA-5-350, with a resistance of 350 Ω, and a gauge length of 5 mm were attached to the mid-length of the tension side (bottom) of the laminate, using a cyanoacrylate-based epoxy, TokyoSokki CN adhesive, to capture the strain response. One resistance-based foil strain gauge, Tokyo-Sokki PL-60-11, with a resistance of 120 Ω, and a gauge length of 60 mm, was also attached to the mid-length of each concrete beam to capture the strain response.

After the CFRP and concrete strain gauges were attached, the specimen was placed on the simply supported mount, and two linear variable displacement transducers (LVDT) were used to measure the deflection. The LVDTs were mounted in the middle of the long span of the specimen, as shown in Figure 3-27. The test was conducted, using the material test system MTS 810 at a loading rate of 1 mm/min (0.04 in/min) and was monitored by the MultiPurpose TestWare (MPT) application.

Figure 3-27 Schematic of flexural testing apparatus for three-point loading test

Chapter 4. Experimental Results and Discussions

4.1 Data Analysis of CFRP Coupons tests

The three basic mechanical parameters, tensile strength, strain, and tensile modulus are discussed in this section for each regime. To calculate the ultimate tensile stress, the maximum loading force was divided by the average cross-sectional area of the coupon sample, as shown in Eq. (4-1).

$$\sigma = {}^{P}/_{A} \tag{4-1}$$

where: σ = the tensile stress,

P = the maximum force before failure, and

A = the average cross-sectional area.

Eight samples were chosen as the control specimens of the experiment. The stress-strain diagram for the control samples is shown in Figure 4-1, and the stress-strain diagrams for all of the environmental conditioned samples are presented in Appendix A. The average failure stress of the control samples was 678 MPa (98.34 ksi) with a standard deviation of 47.39 MPa (6.87 ksi). The dimensions, thickness, and material properties obtained from the tensile test of the control and aged samples, i.e., RT, MT, and HT, are presented in Table 4-1, Table 4-2, and Table 4-3, respectively. The failure modes mentioned in the material tables are based on ASTM D3039 (ASTM, 2017), as shown in Figure 4-2. In the next subsections, tensile strength, strain performance, and modulus of elasticity are discussed for each regime and duration.

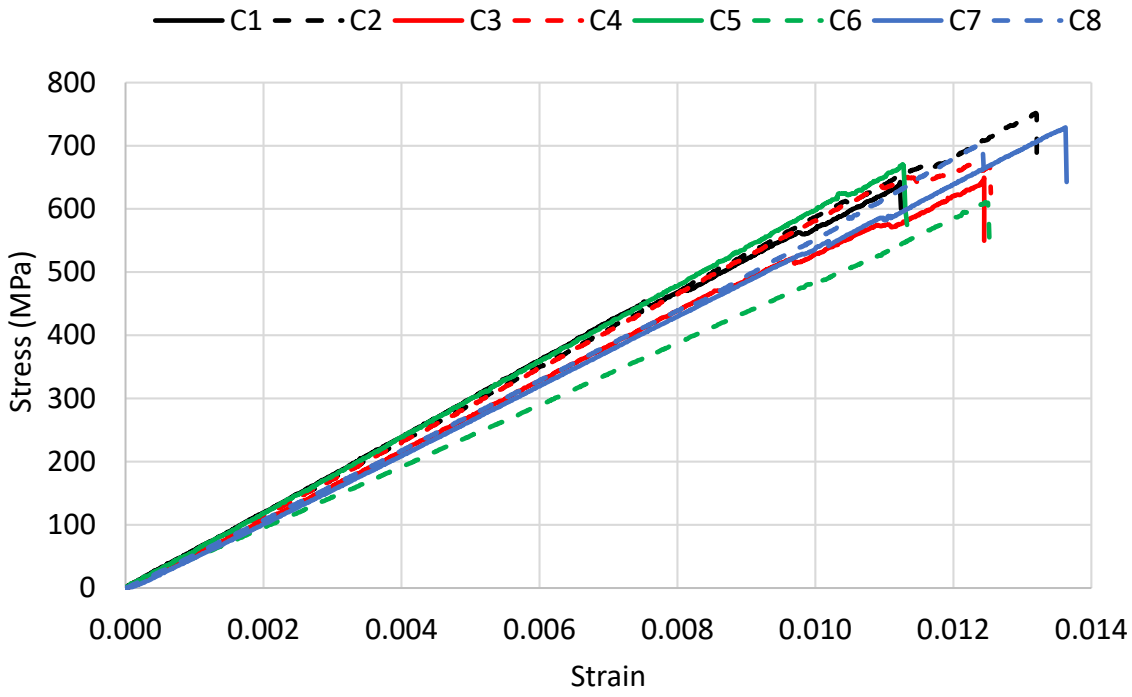

Figure 4-1 Stress-strain diagram for control CFRP samples

Table 4-1 Tensile test results for control CFRP samples

Sample ID	Width (mm)	Thickness (mm)	Area (mm^2)	Fail Stress (MPa)	Fail Strain	Modulus of elasticity (MPa)	Failure mode
C1	14.840	0.795	11.798	642.5	0.0112	59924	SGM
C2	14.680	0.851	12.493	751.7	0.0132	58031	MVV
C3	14.510	0.814	11.811	648.3	0.0124	54473	SGM
C4	14.180	0.801	11.358	667.2	0.0125	57791	SWM
C5	14.730	0.834	12.285	670.7	0.0113	59559	LAB
C6	13.810	0.827	11.421	609.3	0.0125	48276	SGM
C7	12.360	0.876	10.827	728.9	0.0136	52988	LAM
C8	13.660	0.785	10.723	703.6	0.0124	54642	SMM
Average	14.096	0.823	11.589	677.8	0.0124	55711	

Table 4-2 Tensile test results for CFRP coupon samples immersed in water tanks at room temperature (RT)

Sample ID	Exposure time (days)	Width (mm)	Thickness (mm)	Area (mm^2)	Fail stress (MPa)	Fail Strain	Modulus of elasticity (MPa)	Failure mode
RT1		13.94	0.804	11.21	626	0.012	54154	SGM
RT2		13.56	0.847	11.49	614	0.012	51017	SGM
RT3	28	13.93	0.801	11.16	560	0.011	51377	GAB
RT4		14.45	0.852	12.31	698	0.013	51928	AGM
RT5		14.33	0.888	12.73	688	0.012	52028	LIT
RT6		13.85	0.861	11.92	612	0.013	47218	SGM
RT7		14.20	0.879	12.48	613	0.013	46542	GAT
RT8	56	14.45	0.820	11.85	623	0.012	50830	SMT
RT9		14.95	0.798	11.93	690	0.013	52193	XGM
RT10		12.65	0.941	11.90	523	0.012	42449	GAT
RT11		13.77	0.900	12.39	555	0.011	54251	SGM
RT12		14.18	0.933	13.23	555	0.011	51562	GIB
RT13	84	13.91	0.923	12.84	629	0.012	52966	AMV
RT14		14.32	0.891	12.76	613	0.012	51354	SGM
RT15		14.84	0.932	13.83	555	0.011	49709	SGM
RT16		14.57	0.941	13.71	531	0.010	53899	LIT
RT17	112	14.92	0.897	13.38	558	0.011	54295	SGM
RT18		14.45	0.982	14.19	603	0.014	44477	SGM
RT19		14.33	0.938	13.44	512	0.009	58047	GAT
RT21		11.67	0.946	11.04	519	0.013	38892	MVV
RT22		11.82	0.931	11.00	459	0.010	47976	SGM
RT23	224	10.62	1.069	11.35	440	0.010	43875	SGM
RT24		13.06	0.976	12.75	591	0.012	48313	XGM
RT25		12.84	0.892	11.45	521	0.011	49309	SGM

Table 4-3 Tensile test results for CFRP coupon samples immersed in water tanks at moderate temperature (MT)

Sample ID	Exposure time (days)	Width (mm)	Thickness (mm)	Area (mm^2)	Fail stress (MPa)	Fail Strain	Modulus of elasticity (MPa)	Failure mode
MT1	28	14.89	0.822	12.24	595	0.011	52833	SMV
MT2		14.53	0.853	12.39	647	0.012	51817	GAB
MT3		13.71	0.840	11.52	594	0.011	51089	SGM
MT4		14.44	0.846	12.22	579	0.011	56145	XWT
MT6	56	14.10	0.847	11.94	598	0.012	52021	LAB
MT7		14.37	0.874	12.56	543	0.012	47890	GIB
MT8		14.30	0.879	12.57	586	0.012	50192	AMV
MT9		14.25	0.819	11.67	594	0.012	51975	AVB
MT10		14.40	0.869	12.51	638	0.014	47146	LIT
MT11	84	12.81	0.925	11.85	490	0.011	46782	LAT
MT12		14.25	0.973	13.87	530	0.012	45781	SGM
MT13		12.81	0.966	12.37	530	0.014	38062	GAT
MT14		13.66	0.865	11.82	630	0.013	48590	LIT
MT15		13.49	0.934	12.60	585	0.017	38559	LAT
MT16	112	14.03	0.959	13.45	548	0.013	44201	XGT
MT17		14.81	0.904	13.39	585	0.012	49853	SGM
MT18		13.71	0.927	12.71	459	0.010	45612	MGT
MT19		14.64	0.952	13.94	542	0.013	42968	SGM
MT21	224	10.81	0.948	10.25	505	0.011	48007	SGM
MT22		12.84	1.109	14.24	504	0.014	35926	SGM
MT23		14.31	0.901	12.89	542	0.012	45933	GAB
MT24		12.20	1.012	12.35	372	0.008	36337	SGM
MT25		11.66	0.904	10.54	540	0.010	52400	SGM

Table 4-4 Tensile test results for CFRP coupon samples immersed in water tanks at high temperature (HT)

Sample ID	Exposure time (days)	Width (mm)	Thickness (mm)	Area (mm^2)	Fail stress (MPa)	Fail Strain	Modulus of elasticity (MPa)	Failure mode
HT1		14.82	0.886	13.13	685	0.011	56159	LAB
HT2		13.78	0.923	12.72	549	0.012	48924	SVM
HT3	28	14.42	0.871	12.56	548	0.012	46039	XGM
HT4		13.86	0.890	12.34	623	0.012	51502	SGM
HT5		13.91	0.881	12.25	478	0.010	44189	SGM
HT6		15.18	0.886	13.45	636	0.013	48044	SGM
HT7		14.04	0.889	12.48	489	0.012	41187	LAB
HT8	56	14.05	0.890	12.50	511	0.010	50969	SGM
HT9		15.03	0.812	12.20	577	0.011	51282	SGM
HT10		15.10	0.852	12.87	580	0.013	45065	LMV
HT11		14.69	0.980	14.40	529	0.012	43388	SGM
HT12		14.82	0.902	13.37	531	0.012	46707	SGM
HT13	84	14.72	0.929	13.67	544	0.013	42963	LIV
HT14		14.97	0.894	13.38	566	0.013	43913	GAT
HT15		14.65	0.988	14.47	538	0.015	35432	XGM
HT16		14.86	0.960	14.27	495	0.012	39727	LAV
HT17	112	14.91	0.961	14.33	504	0.010	48827	LIB
HT18		14.98	0.943	14.13	480	0.010	47503	SGM
HT19		15.27	0.946	14.45	547	0.012	45067	LAB
HT21		12.89	0.877	11.30	451	0.011	42128	GAT
HT22		11.62	0.945	10.98	538	0.011	46908	SGM
HT23	224	11.34	1.116	12.66	482	0.012	41559	SGM
HT24		11.09	0.989	10.97	469	0.012	40078	SGM
HT25		11.29	1.033	11.66	346	0.010	36242	GAT

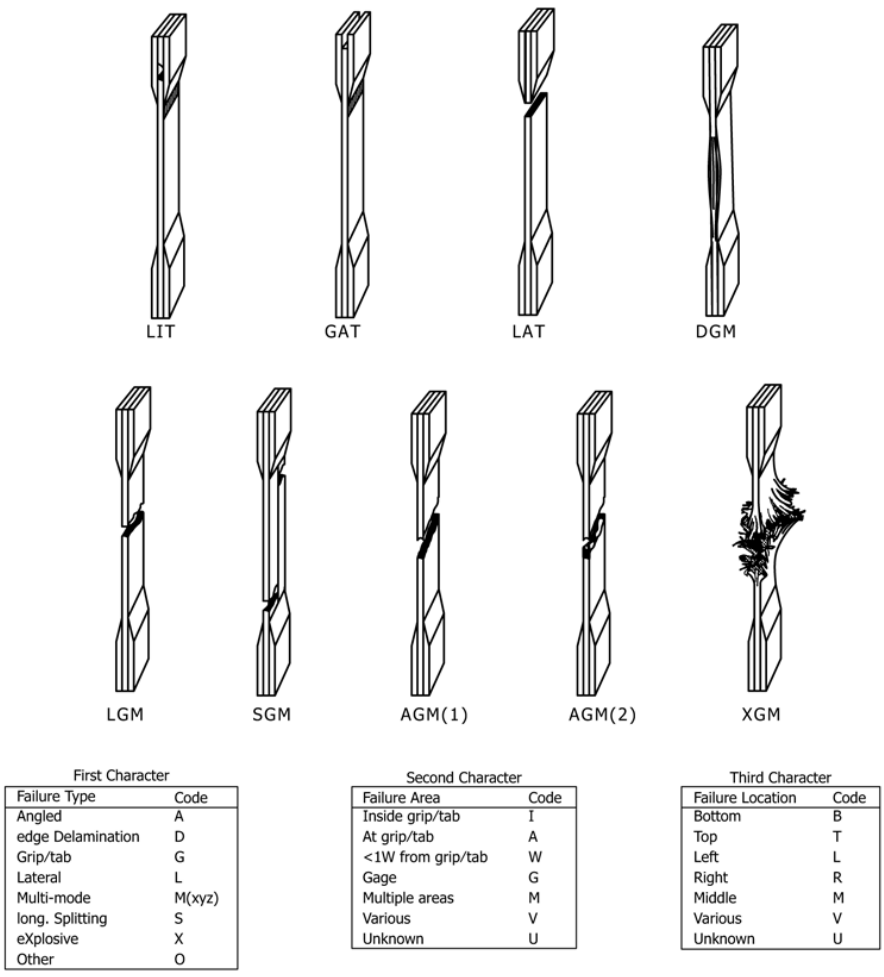

First Character

Failure Type	Code
Angled	A
edge Delamination	D
Grip/tab	G
Lateral	L
Multi-mode	M(xyz)
long. Splitting	S
eXplosive	X
Other	O

Second Character

Failure Area	Code
Inside grip/tab	I
At grip/tab	A
<1W from grip/tab	W
Gage	G
Multiple areas	M
Various	V
Unknown	U

Third Character

Failure Location	Code
Bottom	B
Top	T
Left	L
Right	R
Middle	M
Various	V
Unknown	U

Figure 4-2 Tensile test failure modes ASTM D3039 (2017)

4.1.1 Tensile Strength of CFRP Laminate

The evolution of the tensile strength of the CFRP specimens, along with the process of immersion in different temperatures and for different durations, is presented in Figure 4-3. As indicated and reported by other researchers (Lu and Xian, 2018; Xie et al., 2019), a continual decrease in the tensile strength of the CFRP specimens occurred as the exposure duration increased. On the 224th day of exposure, the reduction in tensile strength of the CFRP specimens, when compared with their initial tensile strength, was about 25%, 27%, and 33% at 23, 45, and 60 °C, respectively. Clearly, water immersion

at 60 °C was damaging to the tensile strength of the CFRP specimens, and higher immersion temperatures accelerated the degradation of tensile strength markedly.

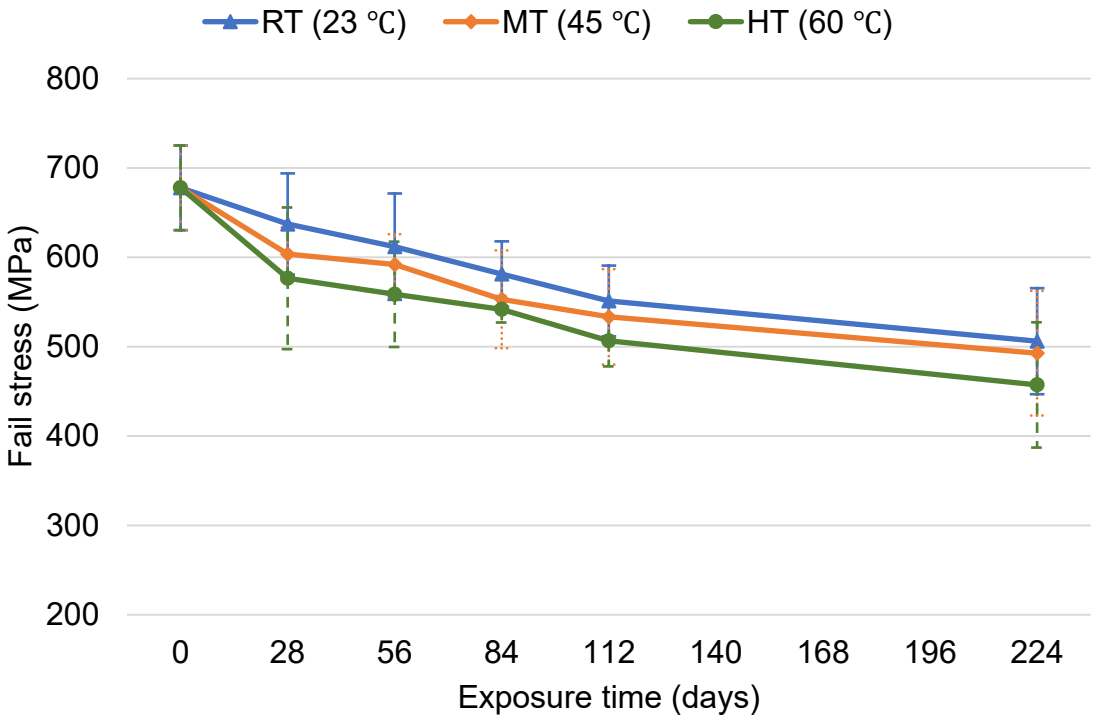

Figure 4-3 Ultimate tensile strength of CFRP samples versus exposure time

The interquartile range (IQR) was used as a statistical approach for measuring the dispersion of the numerical data sets. IQR is the difference between the third quartile (Q_3) and the first quartile (Q_1) and is equal to the length of the box in the boxplot (box-and-whisker). Data sets that fall below $Q_1 - 1.5 \times IQR$ or above $Q_3 + 1.5 \times IQR$ are called outliers. The IQR method was used to measure how the data set of the tensile stress spread out, as shown in Figure 4-4. There was a good distribution of the fail stress data, and even though some mild outliers were observed, discarding them did not change the mean value of the data sets, so they were considered.

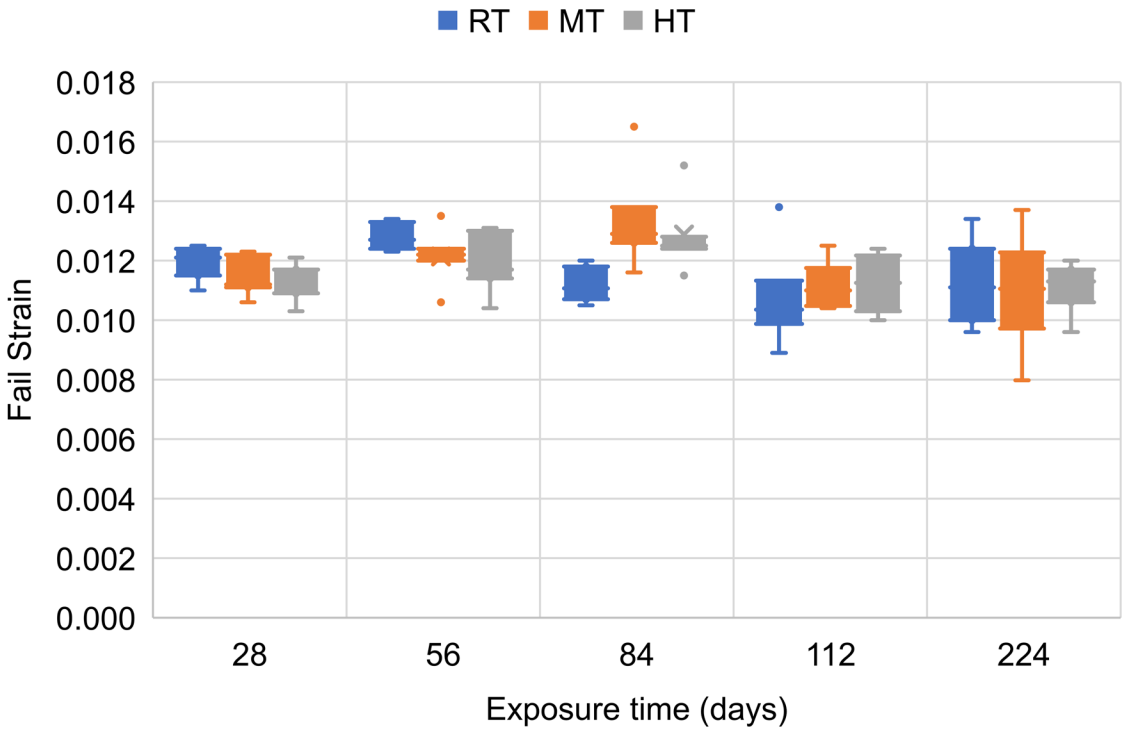

Figure 4-4 Boxplot of fail stress of CFRP samples versus exposure time

4.1.2 Strain Performance of CFRP Laminate

The change in the ultimate strain of the CFRP specimens as a function of the exposure duration is illustrated in Figure 4-5. The strain performance showed an insignificant fluctuation during exposure. The strain behavior increased and then decayed at all temperatures, confirming the case study presented by Xie et al. (2019). On the 224th day of exposure, the reductions in the fail strain of the CFRP specimens, when compared with their initial fail strain, were 9%, 12%, and 11% at 23, 45, and 60 °C, respectively. However, by comparing the fail strain results on the 56th day of exposure with their corresponding initial fail strain, it was found that the elongation increased by 3% and 1% at 23 and 45 °C, respectively, which was attributed to the plasticization effect of the moisture ingress (Hassan et al., 2015).

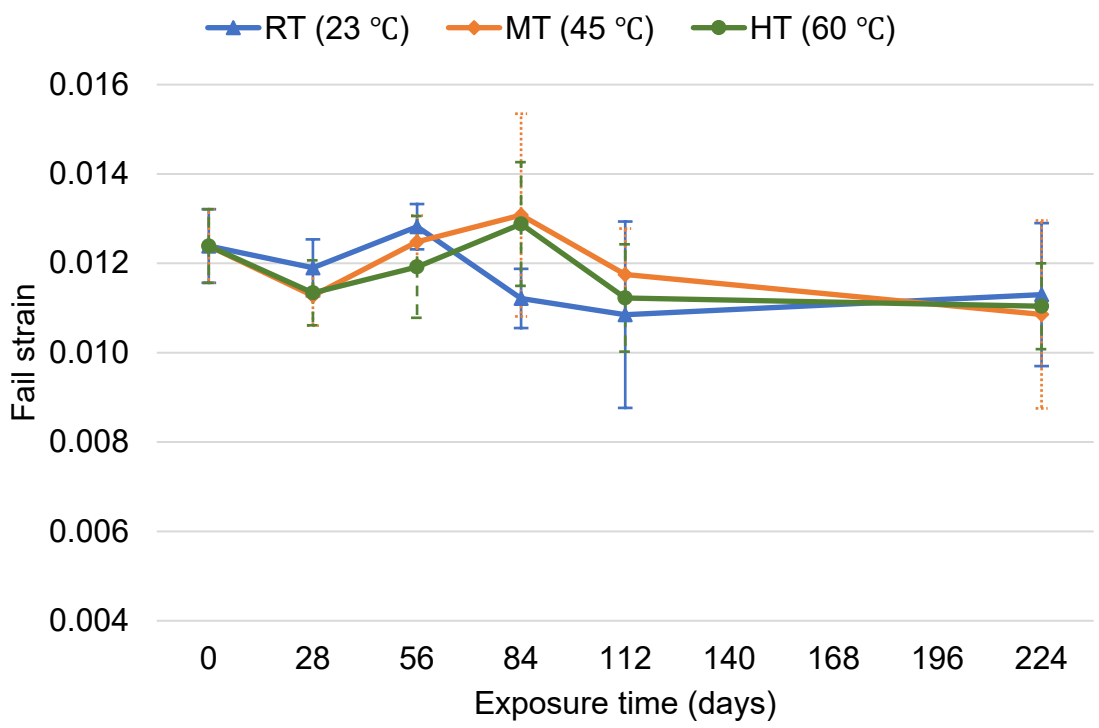

Figure 4-5 Fail strain of CFRP samples versus exposure time

4.1.3 Tensile Modulus of CFRP Laminate

A graph depicting the tensile modulus of the CFRP specimens after exposure to elevated temperatures in the water tanks is presented in Figure 4-6 and shows that the tensile modulus trend is similar to that of the tensile strength. While ACI 440.2R (2017) assumes that the modulus of elasticity is not affected by environmental conditions, the CFRP laminates were affected, especially for the 60 °C condition, which dropped about a quarter of their initial modulus of elasticity. This phenomenon was also observed in other studies (Böer et al., 2013; Borrie et al., 2015; Pan et al., 2015; Xie et al., 2019). The modulus of elasticity of the CFRP specimens dropped 20%, 22%, and 26% at 23, 45, and 60 °C, respectively, from their initial values on the 224th day of exposure. It is worth noting

that the elevated temperatures of the water tanks degraded the tensile modulus of the CFRP specimens.

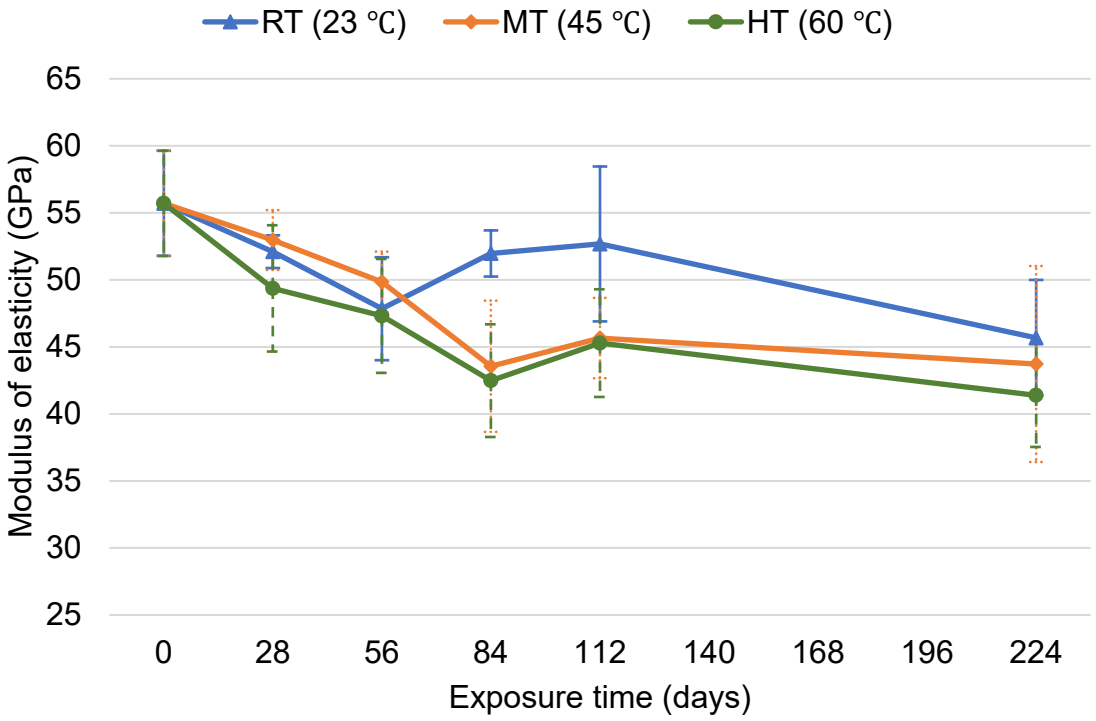

Figure 4-6 Tensile modulus of CFRP samples versus exposure time

4.2 Prediction Model of Long-Term Effects

Predicting the long-term effects and service life of FRP composites is challenging for those who use them in civil infrastructures, as only short-term, limited data is available. The Arrhenius life relationship is widely used in such cases to show first-order effects, due to its accurate results (Karbhari and Abanilla, 2007). The degradation rate proposed by Nelson (2009), is shown in Eq. (4-2):

$$k = A \times \exp\left(\frac{-E_a}{RT}\right) \tag{4-2}$$

where: k = degradation rate (1/time),

A = constant of the material and degradation process,

E_a= activation energy associated with the set of mechanism,

R = universal gas constant (8.3143 10^{-3} kJ/mol K), and

T = temperature in Kelvin.

The main hypothesis of the Arrhenius method is that the single dominant degradation mechanism does not change with temperature and time; however, when the temperature is increased, the degradation rate accelerates. Eq. (4-2) can be converted into Eqs. (4-3) and (4-4), as follows:

$$\frac{1}{K} = \frac{1}{A} \times \exp\left(\frac{E_a}{RT}\right) \tag{4-3}$$

$$ln\left(\frac{1}{K}\right) = \frac{E_a}{RT} - ln(A) \tag{4-4}$$

In Eq. (4-3), the degradation rate, *k*, is expressed as the inverse of the required time to reach a given value of a property of a material. In Eq. (4-4), the required natural logarithmic time for a property of a material to reach a given value is a linear relation of $1/T$ with a slope of E_a/R.

4.2.1 Prediction Procedure

Following the procedure adopted by Chen et al. (2006), the relationship between tensile strength retention, Y, of CFRP laminates and the exposure time was calculated from experimental results obtained for each exposure temperature, as defined in Eq. (4-5):

$$Y = 100 \times \exp\left(\frac{-t}{\tau}\right) \quad (4\text{-}5)$$

where: Y = the percentage of the tensile strength retention, i.e., the percentage of residual strength divided by the original tensile strength,

t = the exposure time, and

τ = fitted parameter, $\tau = 1/k$, as expressed in Eq. (4-3).

As shown in Figure 4-7, the relationship between the tensile strength retention and the exposure time was obtained by regression analysis. The fitted parameter, τ, and the correlation coefficients, R^2, of the curves of each exposure temperature are summarized in Table 4-5.

The Arrhenius relationships of tensile strength retention were obtained by plotting the natural logarithmic time required to reach 60, 70, 80, and 90% of the tensile strength of CFRP laminates versus the inverse of the exposure temperature, as shown in Figure 4-8. Parallel straight lines were fitted to the data using Eq. (4-4); the slopes of the straight lines, E_a/R, and the correlation coefficients, R^2, are listed in Table 4-6. All temperature regression curves should have approximately equal slopes, with correlation coefficients greater than 0.80 (Bank et al., 2003).

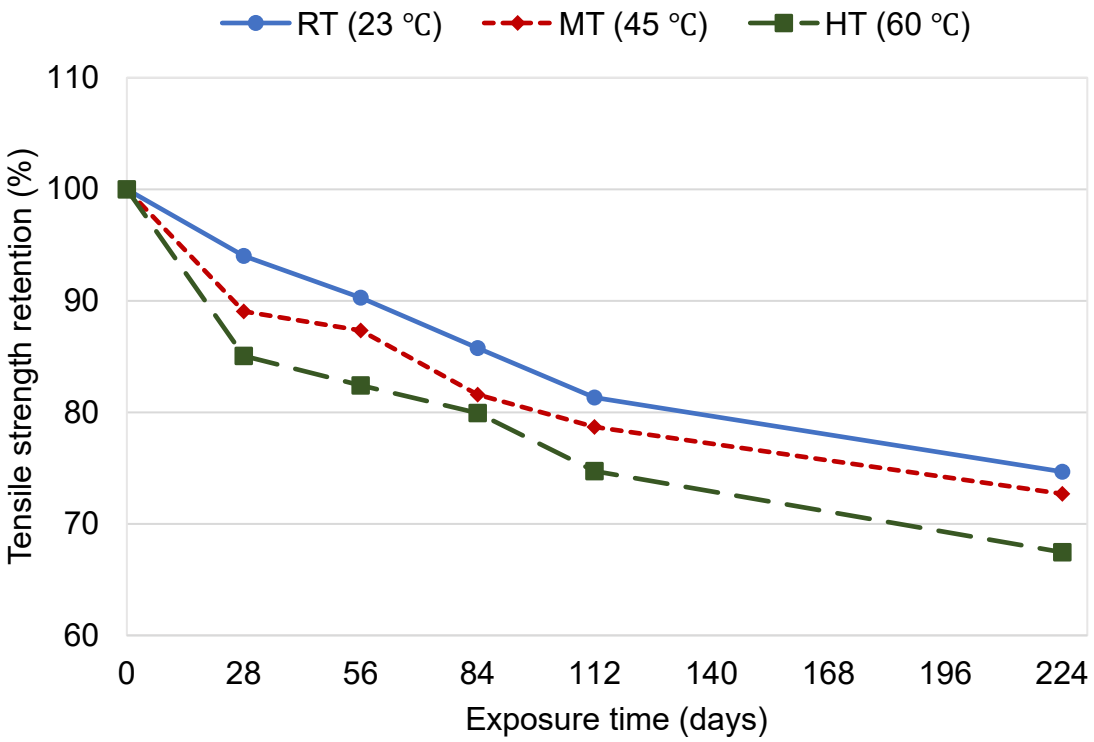

Figure 4-7 Tensile strength retention of CFRP samples versus exposure time

Table 4-5 Correlation coefficients (R^2) and fitted parameters for CFRP tensile strength retention

Water temperature (°C)	Fitted parameter, τ	R^2
23	554	0.99
45	494	0.94
60	434	0.88

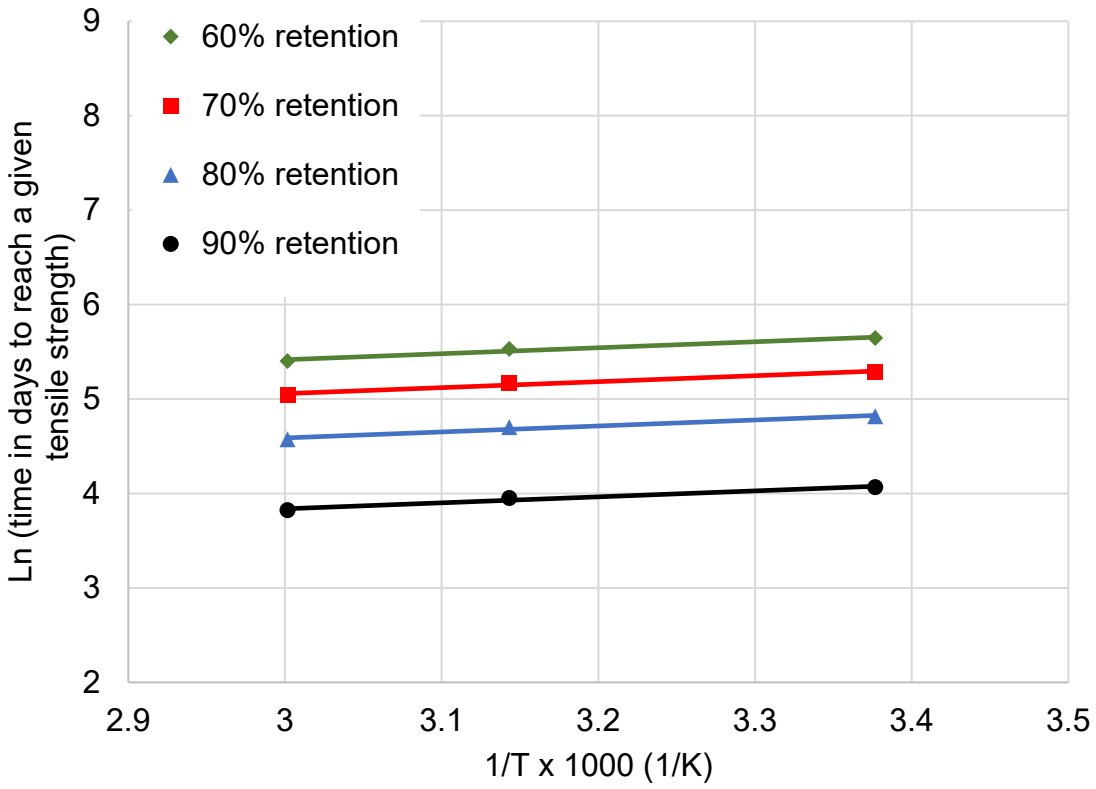

Figure 4-8 Arrhenius plots of tensile strength retention

Table 4-6 The correlation coefficients (R^2) of Eq. (4-4)

Tensile strength retention (%)	E_a/R	R^2
60	632.8	0.97
70	632.8	0.97
80	632.8	0.97
90	632.8	0.97

The time-shift factor (TSF), initially used by Dejke (2001), was based on the ratio of the time required for a material property to reach a given value of strength retention at two different temperatures. The TSF can be expressed as:

$$TSF = \frac{t_0}{t_1} = \frac{{}^{c}/_{k_0}}{{}^{c}/_{k_1}} = \frac{k_1}{k_0} = \frac{A\ exp\left(\frac{-E_a}{RT_1}\right)}{A\ exp\left(\frac{-E_a}{RT_0}\right)} = exp\left[\frac{E_a}{R}\left(\frac{1}{T_0} - \frac{1}{T_1}\right)\right] \quad (4\text{-}6)$$

where: t_1 and t_0 = the required times for a property to reach a given value at temperatures of T_1 and T_0, respectively,

c = a constant, and

k_1 and k_0 = the degradation rates at temperatures of T_1 and T_0, respectively.

The field data was obtained from State Highway 183 bridge over MacArthur Blvd. in Irving, TX. Thus, the temperature used in calculating the TSF values, shown in Table 4-7, are the mean annual temperatures for Irving (18.92 °C).

Table 4-7 Time shift factor for the mean annual temperature for Irving, Texas

Environmental exposure	Mean annual temperature for Irving, Texas (18.92 °C)[1]
RT (23 ℃)	1.03
MT (45 ℃)	1.19
HT (60 ℃)	1.31

[1] Data obtained from (WorldClimate.com, 2020)

The tensile strength retention value of the mean annual temperature for Irving, TX was obtained by multiplying the exposure times at 23, 45, and 60 °C by the corresponding TSF values, as shown in Figure 4-9. By regression analysis, a linear line was fitted to the data with a correlation coefficient, R^2, greater than 0.8, which confirmed the validity of this procedure.

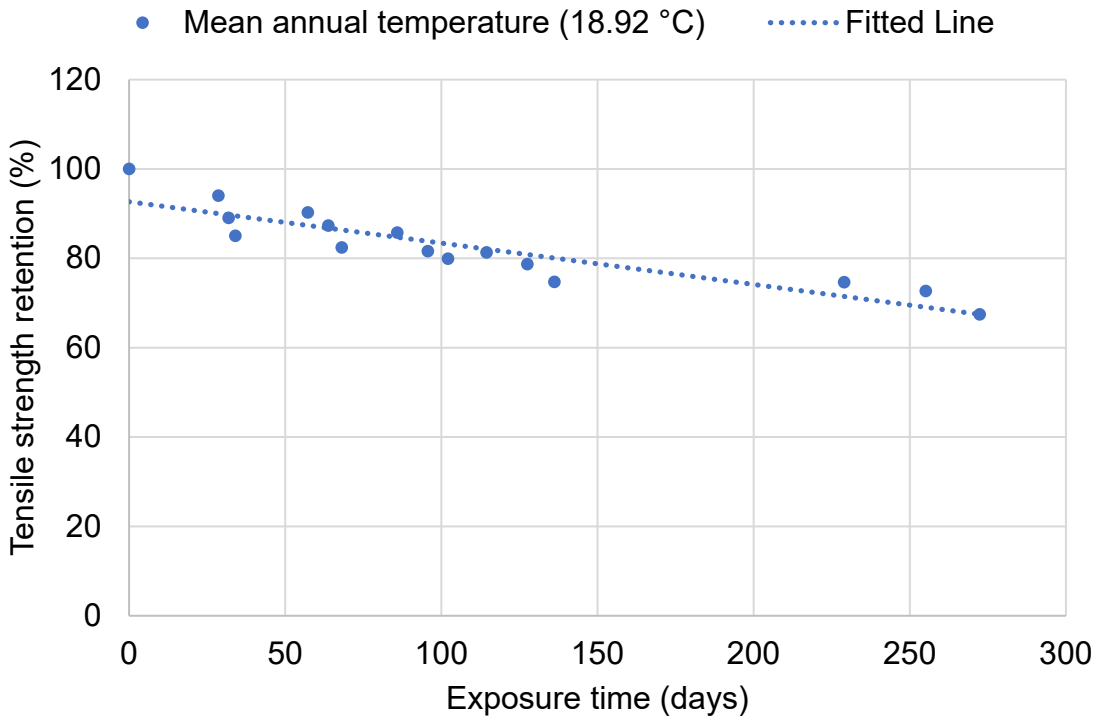

Figure 4-9 Tensile strength retention for mean annual temperature

A predictive equation was used to estimate the long-term performance of the tensile strength of CFRP, using the Arrhenius method (Karbhari and Abanilla, 2007; Li et al., 2017). The predictive equation can be expressed as in Eq. (4-7):

$$f(t) = \frac{f_0}{100}[A\,ln(t) + B],\ \ (t > 0) \tag{4-7}$$

where: $f(t)$ and f_0 = the performance attributes at time t (in days), and 0 (i.e., in the unexposed condition), respectively,

A = a constant denoting degradation rate, and

B = a material constant, which reflects the early effects of post-cure progression.

The value of $B = 100$ indicates that the material is fully cured prior to being subjected to environmental exposure. The predictive Eq. 4-7 for the mean annual

temperature of Irving, Texas was utilized by regression analysis obtained from Figure 4-9. As shown in Figure 4-10, the prediction model, which was based on the mean annual temperature for Irving, was plotted using Eq. (4-8).

$$f(t) = -0.92\, ln(t) + 100 \tag{4-8}$$

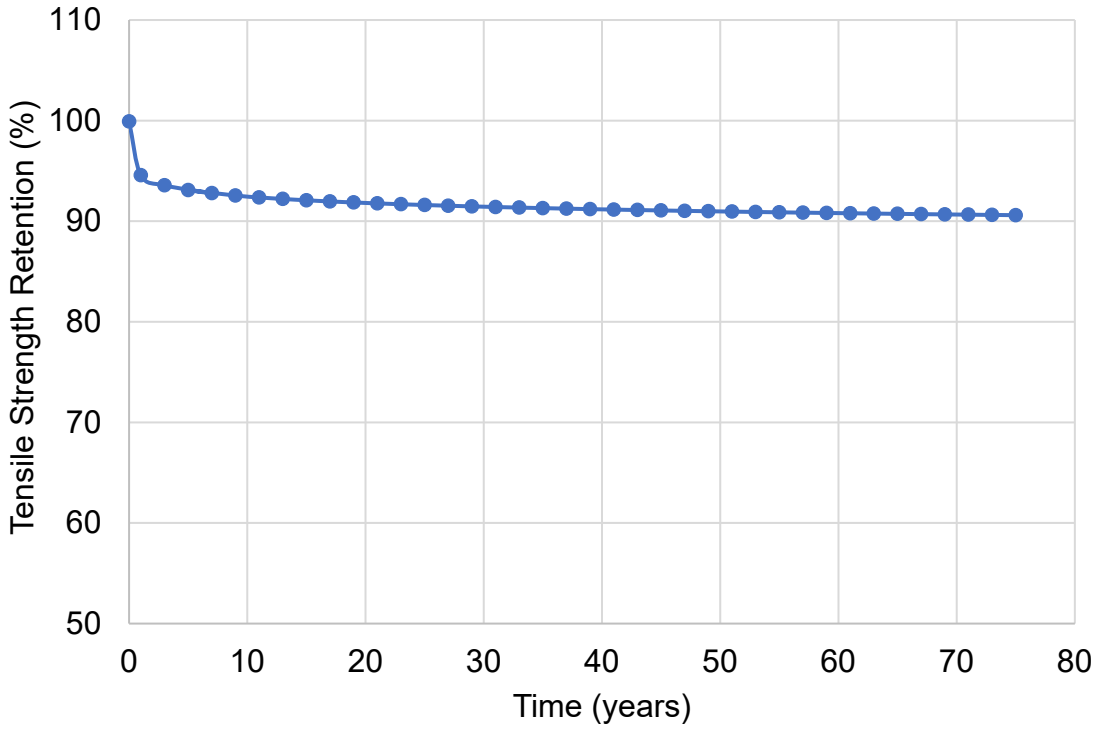

Figure 4-10 Prediction model based on the mean annual temperature for Irving, TX

4.2.2 Calibrated Prediction Model

It is essential to calibrate the model with real data from the field after predicting the long-term behavior of CFRP laminate. Thus, the predictive Eq. (4-7) was modified to correspond with the field data obtained from studies conducted by Timilsina et al. (Timilsina, et al., 2020; Timilsina, 2018). Figure 4-11 shows the calibrated prediction model, using Eq. (4-9), along with the uncalibrated model.

$$f(t) = -2.44\,ln(t) + 100 \quad (4\text{-}9)$$

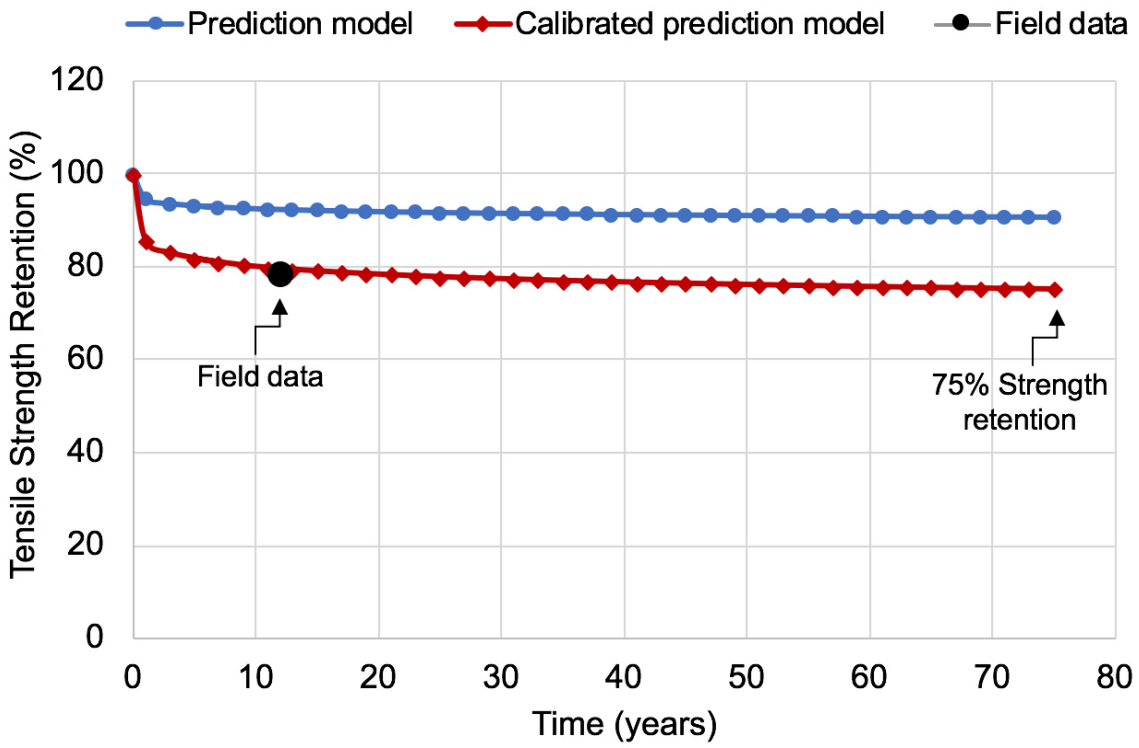

Figure 4-11 Calibrated prediction model with field data

4.2.3 Comparison Between Prediction Models

Four prediction models were calibrated with the real data from Timilsina et al. (Timilsina, et al., 2020; Timilsina, 2018) and compared to each other. The first prediction model was based on the study conducted by Bank et al. (2003), which successfully predicted the service life of glass fiber concrete by plotting the property retention of accelerated aging data versus time in the logarithmic scale. It was also used to predict the long-term performance of GFRP bars embedded in concrete (Robert et al., 2009). Limitations of this model were reported by Davalos et al. (2012) and Wang et al. (2014 and 2017), however, as the test data was only represented phylogenomically, without

considering any degradation mechanism. The tensile strength retention, Y, of the model was utilized as in Eq. (4-10) and approached infinity at time zero, which obviously contradicted the real test data. As shown in Figure 4-12, the Arrhenius plots fitted by using this model were not parallel to each other, which violated the primary hypothesis, so no further investigation was conducted.

$$Y = a\,log(t) + b \tag{4-10}$$

where: a and b are regression constants.

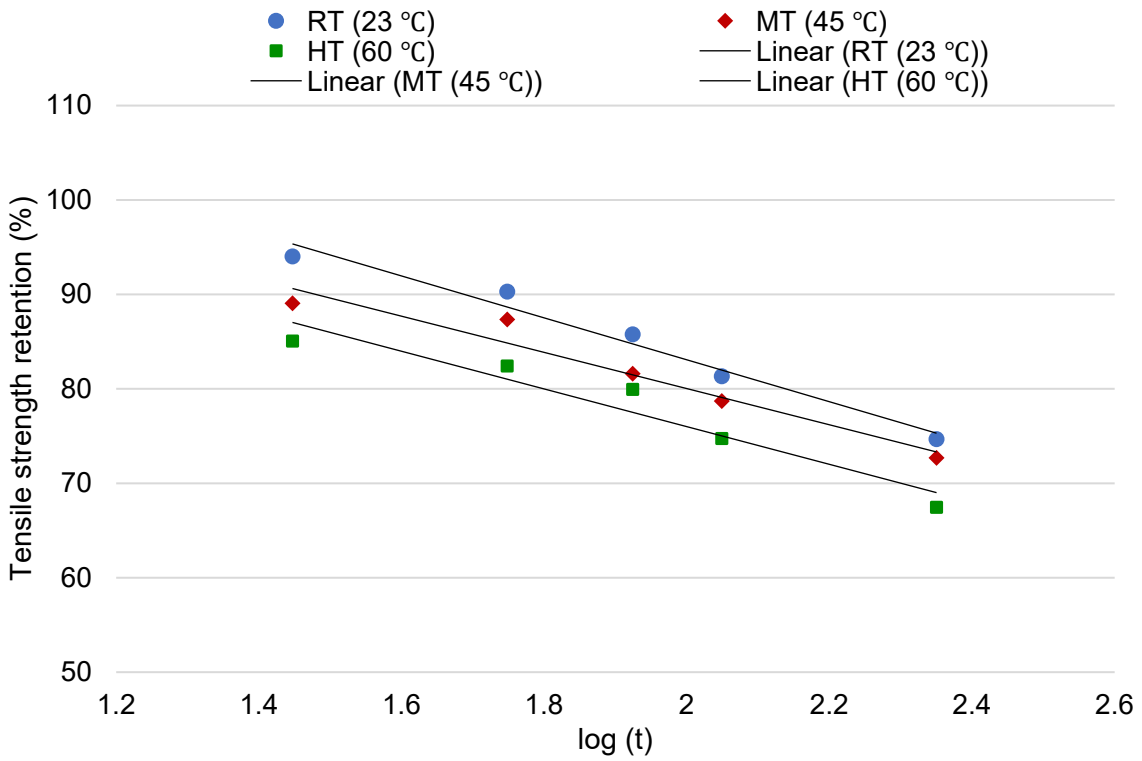

Figure 4-12 Fitted curves for tensile strength retention versus logarithmic time

The second model was first proposed by Phani and Bose (1986) and later adopted by many researchers (Chen et al., 2006; Wang et al., 2014, 2017). The procedures followed for this model were similar to those described in Section 4.2.1 except for the final

step, which was to use Eq. (4-5), rather than Eq. (4-7), as the predictive equation. Figure 4-13 shows the second model's prediction, which was based on the mean annual temperature for Irving, TX, and was plotted using Eq. (4-11). In order to calibrate this model with the real data, Eq. (4-11) was converted to Eq. (4-12) as follows:

$$Y = 100 \times \exp\left(\frac{-t}{878}\right) \tag{4-11}$$

$$Y = 100 \times \exp\left(\frac{-t}{17544}\right) \tag{4-12}$$

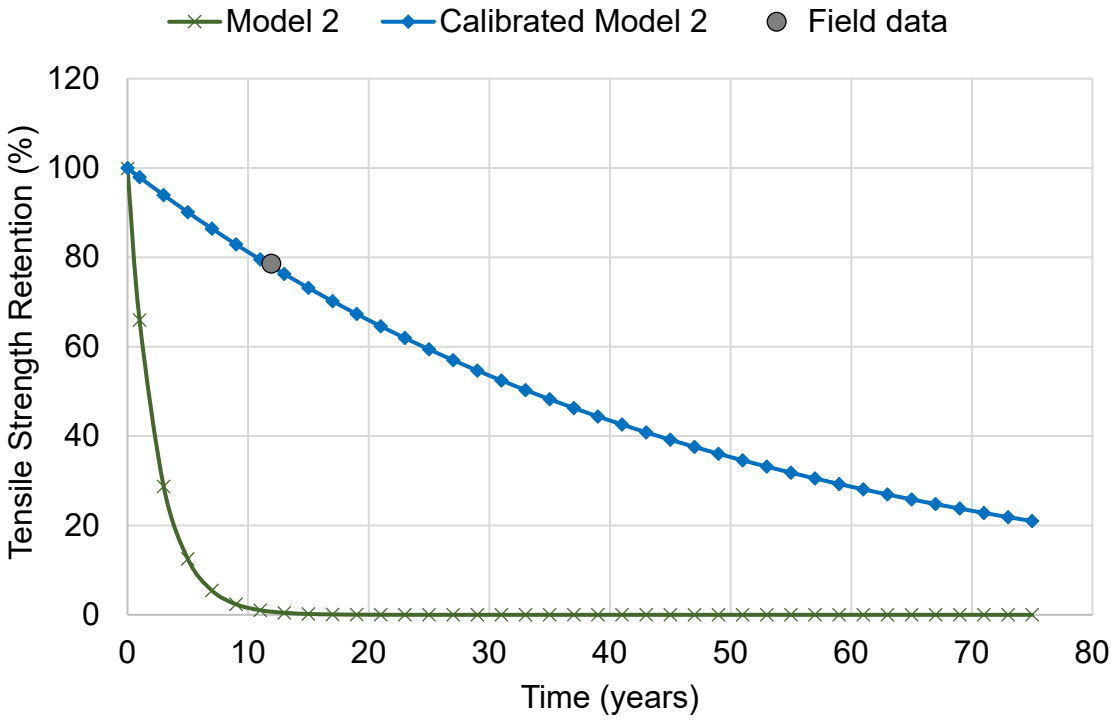

Figure 4-13 Model 2 calibrated with field data

Model 2 approached zero strength retention after 10 years of service life (Figure 4-13), and after being calibrated with real data, the strength retention approached 20% after 75 years. According to Wang et al. (2017), Model 2 was sensitive to temperature

ranges. Chen et al. (2006) predicted the long-term behavior of GFRP bars for 900 days, and the tensile strength retention reached zero after 20 years of service life. Therefore, it can be concluded that this model greatly underestimates the performance of the FRPs.

Model 3, introduced by Phani and Bose (1987), modified the predictive Eqs. (4-5) to (4-13) and requires assuming a level of performance that directly influences the location of the asymptote.

$$Y = (100 - Y_\infty)\exp(-t/\tau) + Y_\infty \quad (4\text{-}13)$$

where: Y_∞ = the tensile strength retention (%) at the exposure time of infinity.

Davalos et al. (2012) used a value of Y_∞ of 45% and 38% for unloaded and loaded concrete with GFRP bars, respectively; thus 45% of Y_∞ was implemented in this model. As shown in Figure 4-14, the prediction of this model was plotted using Eq. (4-14), and the equation was transformed into Eq. (4-15) in order to calibrate it.

$$Y = 55\exp\left(\frac{-t}{2273}\right) + 45 \quad (4\text{-}14)$$

$$Y = 55\exp\left(\frac{-t}{9000}\right) + 45 \quad (4\text{-}15)$$

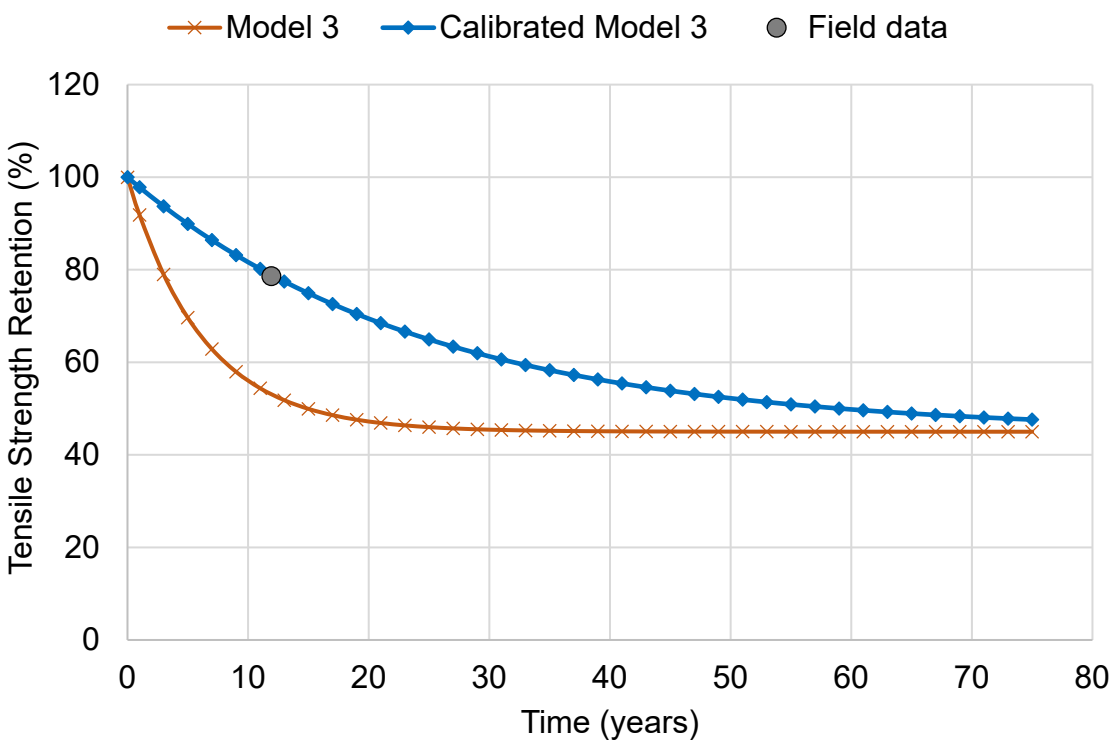

Figure 4-14 Model 3 calibrated with field data

The fourth prediction model, described in Section 4.2.1, was proven to be accurate in studies conducted by Karbhari and Abanilla (2007) and Li et al. (2017) and is suitable for predicting the long-term performance of FRPs (more than 50 years). According to the AASHTO LRFD Bridge Design Specifications, the design life of a highway bridge is 75 years (AASHTO, 2017). Thus, it was essential to compare the three calibrated prediction models after 75 years of service life. Figure 4-15 shows the comparison between the calibrated prediction modes in linear and logarithmic scales. Model 4 was the most appropriate model for prediction of CFRP laminate due to the following reasons:

1) Model 4 has fewer errors than the uncalibrated model.

2) Models 2 and 3, cited in the literature, were suitable for FRPs bars, but not laminate.
3) Model 2 greatly underestimated the strength retention after 75 years of service life.
4) Model 3 was based on the assumption of strength retention at time zero, which made it subjective and influenced the long-term performance.

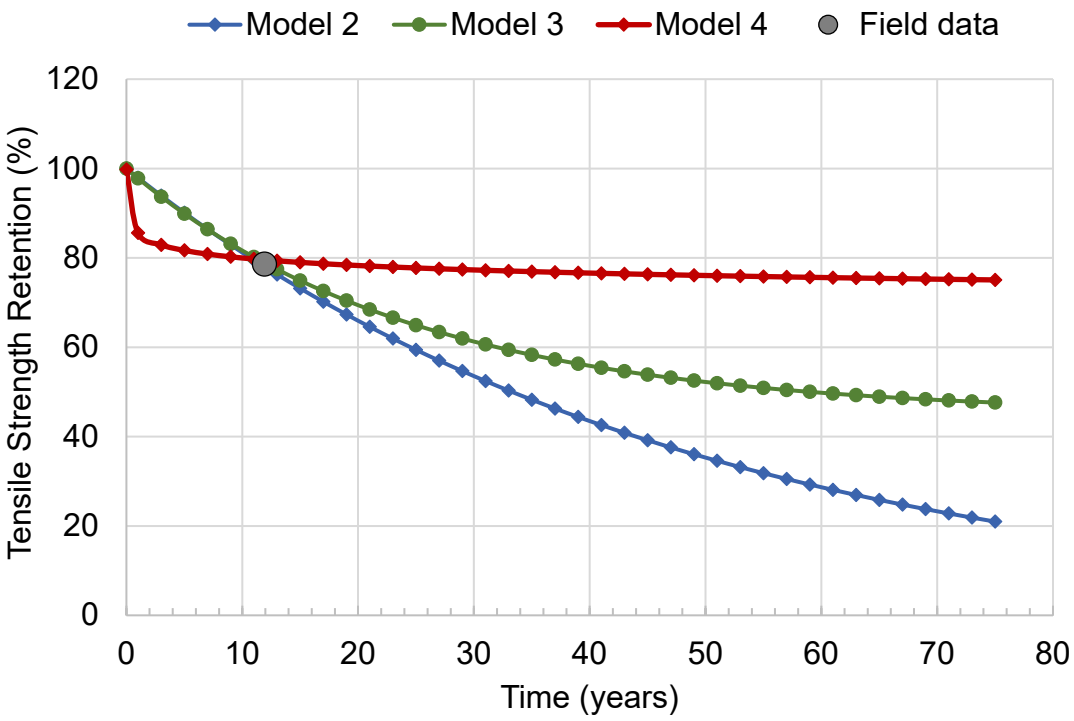

(a) Tensile strength retention versus time in linear scale

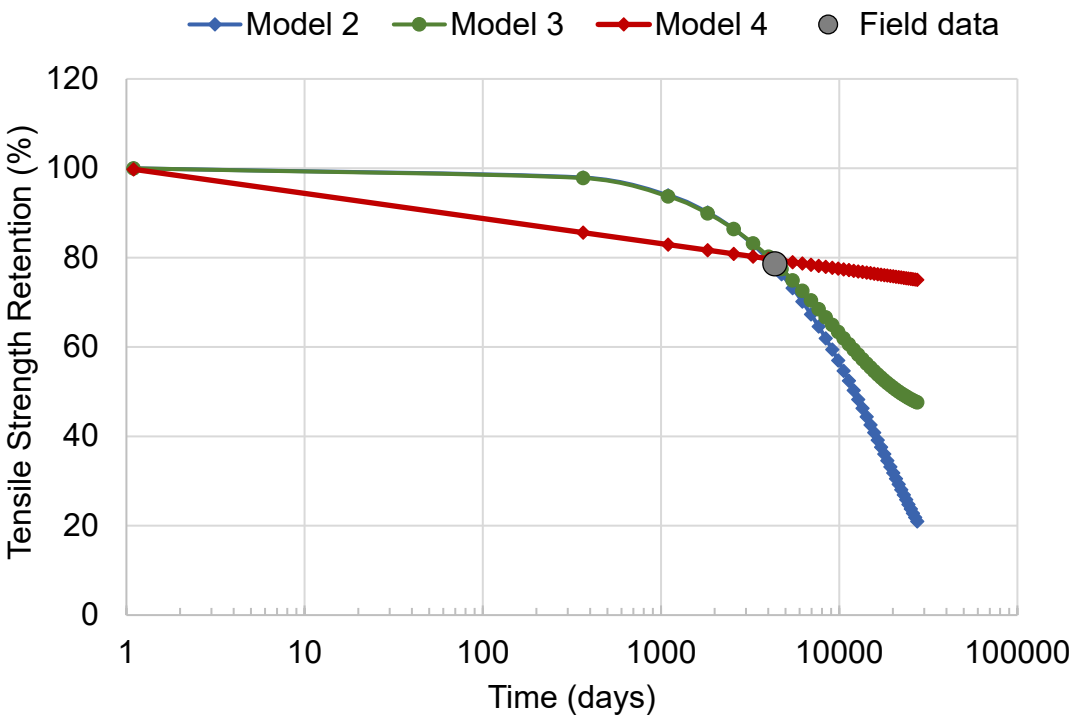

(b) Tensile strength retention versus time in a logarithmic scale

Figure 4-15 Comparison between three calibrated prediction models

4.2.4 Determination of Environmental Reduction Factor

When determining the design value for any material, it is important to consider the likelihood of deterioration due to environmental exposure. Hence, it was imperative to consider the long-term performance of CFRP laminate over the design life of the structure by reducing the tensile strength by such a factor.

ACI 440.2R (2017) proposes that the design ultimate strength, f_{fu}, be determined by modifying the strength reported by the manufacturer, f_{fu}^{*}, by the environmental reduction factor, C_E, as defined in Eq. (4-16):

$$f_{\mathrm{fu}} = C_E \times f_{\mathrm{fu}}^{*} \tag{4-16}$$

where

$$f_{\mathrm{fu}}^{*} = \bar{f}_{\mathrm{fu}} - 3\sigma \tag{4-17}$$

where: $\bar{f}_{\mathrm{fu}}$ = the mean ultimate strength, and

σ = the standard deviation.

For exterior bridge exposure similar to that described by Timilsina, et al., (Timilsina, et al., 2020), the environmental reduction factor, C_E, was 0.85 for the CFRP material. While the UK code (TR55, 2012) gives no explicit environmental reduction factors, characteristic material properties are divided by additional safety factors to determine the appropriate design value, f_{fd}, as defined in Eq. (4-18):

$$f_{\mathrm{fd}} = \frac{f_{\mathrm{fm}} - 2\sigma}{\gamma_{\mathrm{mf}}\,\gamma_{\mathrm{mm}}} \tag{4-18}$$

where: f_{fm} = the mean ultimate strength,

γ_{mf} = the fiber strength at the ultimate limit state, and

γ_{mm} = the method of manufacture and application.

For wet lay-up CFRP laminate, the values of γ_{mf} and γ_{mm} are 1.4, respectively.

Guidelines from the Chinese code (GB 50608-2010, 2010) suggest that allowable ultimate design strength be defined as in Eq. (4-19):

$$f_{\mathrm{fd}} = \frac{f_{\mathrm{fk}}}{\gamma_{\mathrm{f}}\ \gamma_{\mathrm{E}}} \tag{4-19}$$

where: $f_{\mathrm{fk}} = \mu_{\mathrm{f}} - \ 1.645\ \sigma_{\mathrm{f}}$

μ_{f} = the mean ultimate strength,

σ_{f} = the standard deviation,

γ_{f} = the reliability index and the brittle failure behavior of FRP materials, and

γ_{E} = the environmental influence factor.

For wet lay-up CFRP laminate, the values of γ_{f} and γ_{E} are 1.4 and 1.2, respectively.

The European (FIB Bulletin 14, 2001) suggests that the design tensile strength can be calculated using Eq. (4-20):

$$f_{\mathrm{fd}} = \frac{f_{\mathrm{fk,}}}{\gamma_{\mathrm{f,fib}}}\frac{\varepsilon_{\mathrm{fue}}}{\varepsilon_{\mathrm{fum}}} \tag{4-20}$$

where: $\gamma_{\mathrm{f,fib}}$ = the CFRP material safety factor and suggested to be 1.35 for wet lay-up, and

$\varepsilon_{\mathrm{fue}}$ and $\varepsilon_{\mathrm{fum}}$ = the effective and mean ultimate FRP strain, respectively.

The codes of the Italian National Research Council (2014) and the Egyptian Ministry of Housing and Utilities and Urban Utilities (2005) recommend environmental reduction factors identical to ACI 440.2R (2017). In order to facilitate comparisons between standard codes, reciprocal safety factors, (1/x), of TR55, GB 50608, and Fib

Bulletin 14 were considered as equivalent environmental reduction factors, as listed in Table 4-8.

Table 4-8 Comparison between environmental reduction factors of CFRP in different international standard codes

Title	Country	Publishing Institution	Year	Environmental factor for CFRP
ACI 440.2R	USA	American Concrete Institute (ACI)	2017	0.85
TR55	UK	The Concrete Society	2012	0.51
GB 50608	China	China Architecture & Building Press	2011	0.60
Fib Bulletin 14	Europe	International Federation for Structural Concrete (fib)	2001	0.74
CNR-DT 200	Italy	Advisory Committee on Technical Recommendations for Construction	2014	0.85
ECP 208	Egypt	Egyptian Housing and Building National Research Center	2005	0.85

4.2.5 Comparison of Calibrated Perdition Model with Environmental Reduction Factor

A comparison of the calibrated perdition model with the environmental reduction factor from ACI 440.2R (2017) was completed to evaluate the reasonability of the allowable design. According to the AASHTO LRFD Bridge Design Specifications, the design life of a highway bridge is 75 years (AASHTO, 2017). Thus, as seen from Figure 4-11, the tensile strength retention is 75% at 75 years, which is smaller than the environmental reduction factor, C_E, by 0.1. Clearly, the calibrated perdition model for the

tensile strength of CFRP material is inadequate in terms of the allowable strength design of ACI 440.2R (2017).

The environmental reduction factor of CFRP laminate of the UK standard code (TR55, 2012), 0.51, is the most conservative of the international strengthening guidelines, followed by the Chinese code (GB 50608-2010, 2010) of 0.60 and the European Fib Bulletin 14 (2001) of 0.74. The Italian (National Research Council, 2014) and the Egyptian (Ministry of Housing Utilities and Urban Utilities, 2005) codes are similar to the ACI 440.2R (2017) factor. Some fluctuations were noted in the values of the environmental reduction factor of CFRP in the six strengthening guidelines.

The comparative results showed that ACI 440.2R (2017) overestimated the tensile strength of CFRP material, which may result in structural failure before the completion of the designed service life. Therefore, based on the findings, a function of the design life (in days) of the environmental reduction factor, C_E, for CFRP material was proposed, as shown in Eq. (4-21). By implementing this function, a recommendation of 0.75 was made for the environmental reduction factor.

$$C_E = \frac{100 - 2.44\, ln(t)}{100} \tag{4-21}$$

4.3 Data Analysis of CFRP-Concrete-Bonded Beams tests

4.3.1 Pull-off Test Results

A total of 28 pull-off tests were performed on 14 differ specimens. The failure mode of each test was per ASTM D7522 (2012). A standard for the failure modes of the pull-off

test is shown in Figure 4-16, and a detailed description of each failure mode is listed in Table 4-9.

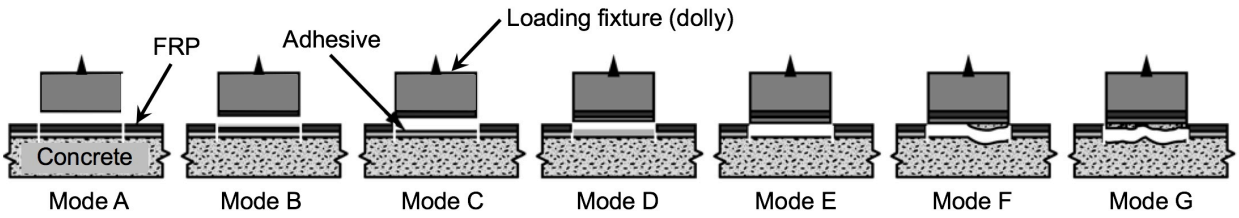

Figure 4-16 Failure modes for pull-off test, adopted from ASTM D7522

Table 4-9 Description of pull-off test failure modes (Pallempati et al. 2016)

Failure mode	Failure type	Possible causes of failure
A	Bonding epoxy failure at dolly (loading fixture)	Use of an inappropriate bonding epoxy system for affixing the dolly
B	Cohesive failure in FRP laminate	Incomplete epoxy saturation of the fibers or environmental degradation of the FRP material
C	Epoxy failure at FRP/epoxy interface	Improper selection of epoxy, contamination of epoxy, improper or incomplete epoxy curing, contamination or improper preparation or cleaning of adherent surfaces or environmental degradation
D	Cohesive failure in epoxy	Contamination of epoxy, incomplete curing, environmental degradation of the material
E	Epoxy failure at FRP/concrete interface	Improper selection of epoxy, contamination of epoxy, improper or incomplete epoxy curing, contamination or improper preparation or cleaning of concrete surfaces or environmental degradation
F	Mixed cohesive failure in concrete and epoxy at the epoxy/concrete interface	Inconsistent FRP-concrete adhesion. Failure is partly in epoxy and partly in concrete
G	Cohesive failure in concrete substrate	Proper adhesion of FRP–concrete. Desirable failure mode

The test results are presented in Table 4-10, which lists the pull-off bond strength and the failure mode from each test. Figure 4-17 shows a collection of failure mode results from the pull-off test.

Table 4-10 Summary of pull-off test results

Test ID	Exposure time (days)	Pull-off bond strength (MPa)	Pull-off bond strength (psi)	Failure mode
C1L	0	3.27	474	G
C2R		2.28	330	G
C3L		3.35	486	F (5% E, 95% G)
C4R		2.52	366	A
RT1L	28	3.51	509	G
RT1R		2.83	410	F (20% E, 80% G)
MT1L		1.60	232	A
MT1R		2.85	414	A
HT1L		3.16	459	G
HT1R		3.10	450	F (5% E, 95% G)
RT2L	56	2.43	352	G
RT2R		3.86	560	A
MT2L		2.63	381	F (50% E, 50% G)
MT2R		2.92	423	G
HT2L		3.66	531	A
HT2R		3.58	519	G
RT3L	84	3.08	447	A
RT3R		1.44	209	G
MT3L		2.63	381	A
MT3R		1.94	281	A
HT3L		3.48	505	A
HT3R		1.70	246	G
RT4L	112	2.09	303	G
RT4R		3.45	500	A
MT4L		2.20	319	A
MT4R		3.74	542	A
HT4L		3.41	495	G
HT4R		1.85	269	F (25% E, 75% G)

(a) (b)

Figure 4-17 (a) various observed failure modes, (b) dolly next to its original location

Bonding epoxy failure was observed at dolly, Mode A, and occurred in 43% of the samples, followed by 39% cohesive failure in the concrete substrate, Mode G. The failure mode least witnessed was mixed cohesive failure in concrete and epoxy at the epoxy/concrete interface, Mode F, which occurred in18% of the samples, as shown in Figure 4-18. The number of occurrences of each failure mode associated with each environmental exposure condition is shown in Figure 4-19.

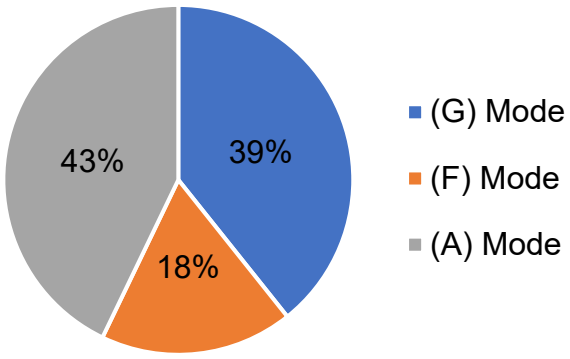

Figure 4-18 Summary of pull-off test failure modes

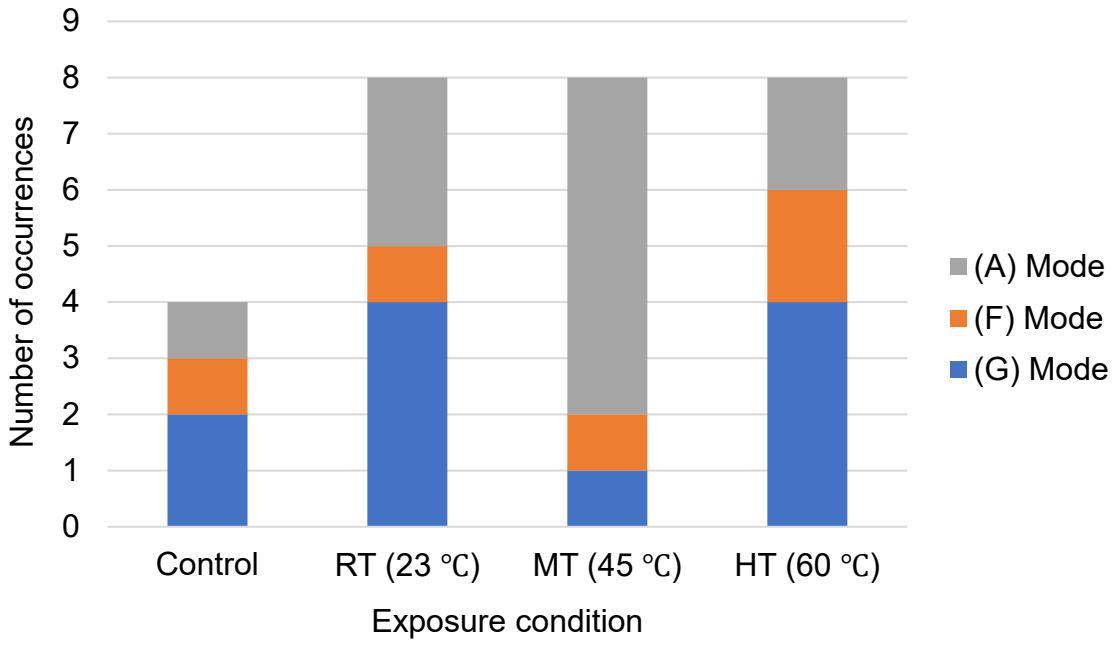

Figure 4-19 Distribution of failure modes to the environmental exposure

Mode A was the predominant failure mode, and some possible causes of failure included using an unsuitable bonding epoxy system for attaching the dolly, improper surface preparation, and inappropriate pull-off tester orientation and application. As seen from Figure 4-19, a moderate temperature MT (45 °C) was the main failure in Mode A, and it occurred in six out of eight tests. Although failure Mode A was considered an unsuccessful pull-off test mode, it was necessary to compare the bond strength with and without including failure Mode A, as shown in Figure 4-20. The pull-off stress failures showed an insignificant fluctuation during the exposure. In all the environmental conditions, the stress behavior increased, decayed, and then increased. The age-based environmental degradation is not a significant factor in the strength of the FRP-epoxy-concrete interface (Pallempati et al., 2016). The capacity of the adhesion tester was 3.86 MPa (560 psi), and some of the tests reached this value, which indicated an excellent CFRP-epoxy performance.

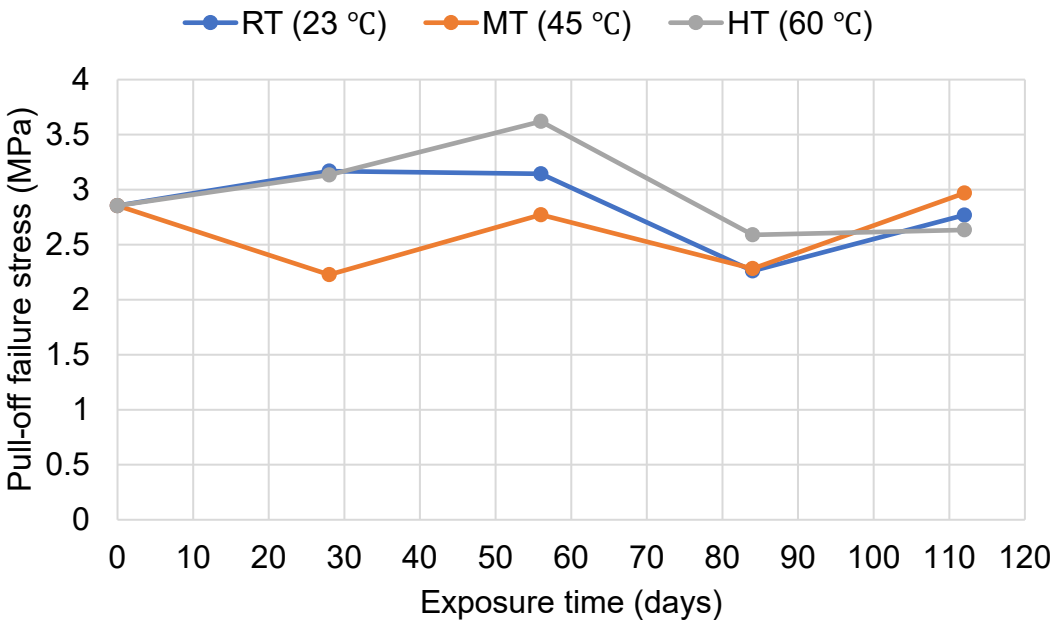

(a) All failure modes are included

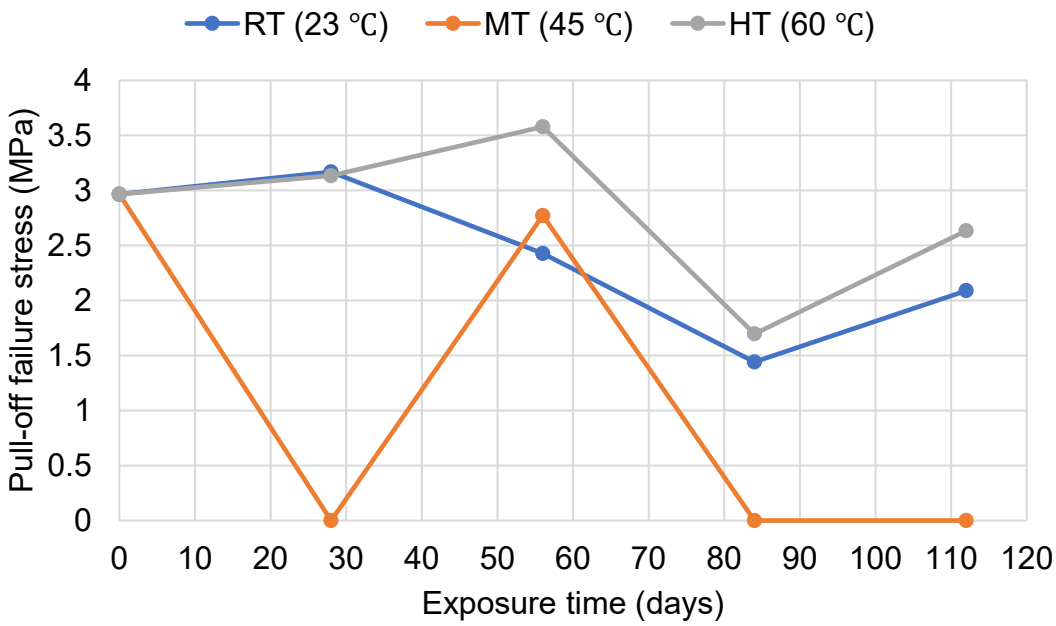

(b) Failure mode (A) is excluded

Figure 4-20 Pull-off stress versus exposure time of different environmental conditions including and excluding failure mode (A)

4.3.2 Flexural Test Results

4.3.2.1 Load-deflection behavior

The flexural strength of concrete beams with dimensions of 152 x 152 x 533 mm (6 x 6 x 21 in.) was evaluated using a three-point loading test in accordance with ASTM C78/C78M (2010). Loads versus deflections were plotted for specimens in control, room, moderate, and high temperatures specimens for different time periods, as shown in Figure 4-21. Inspection of the load-deflection curve can be divided into two sections. The first section is a linear relationship from zero loading up to pre-cracking of the beam, indicating a large increase in load with corresponding small deformations. The second section, with reduced stiffness, is for the post-cracking of the beam, signifying the contribution of the externally bonded CFRP laminate.

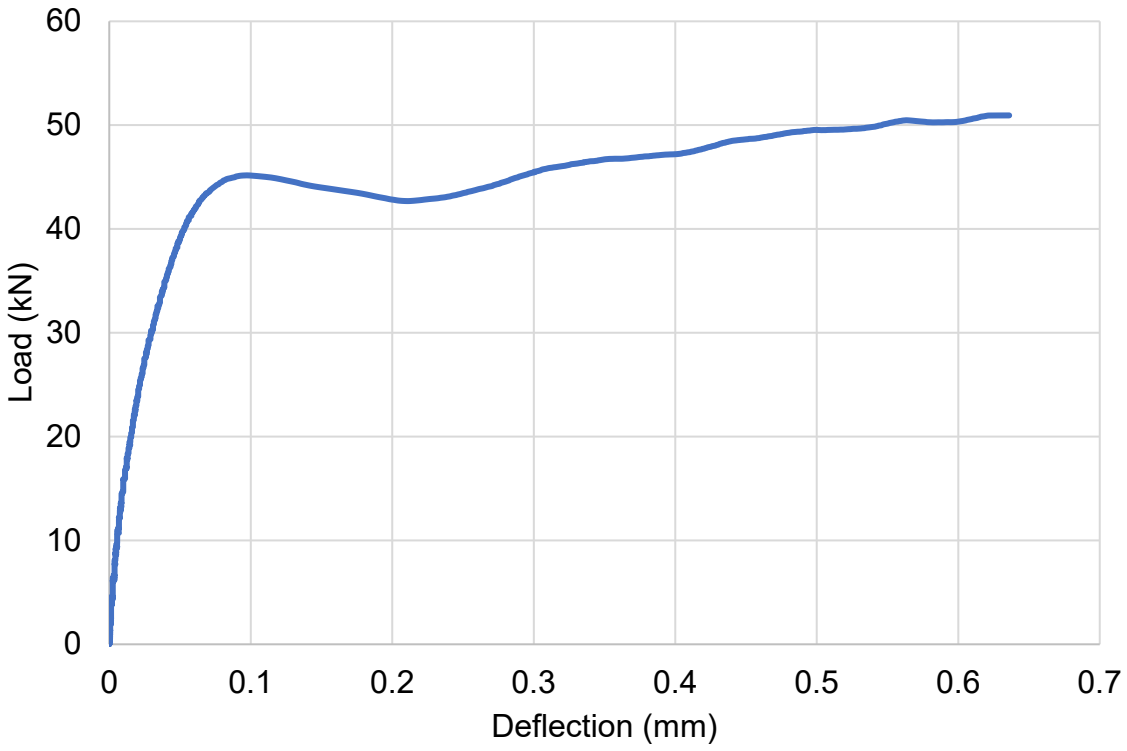

(a) Average control specimens

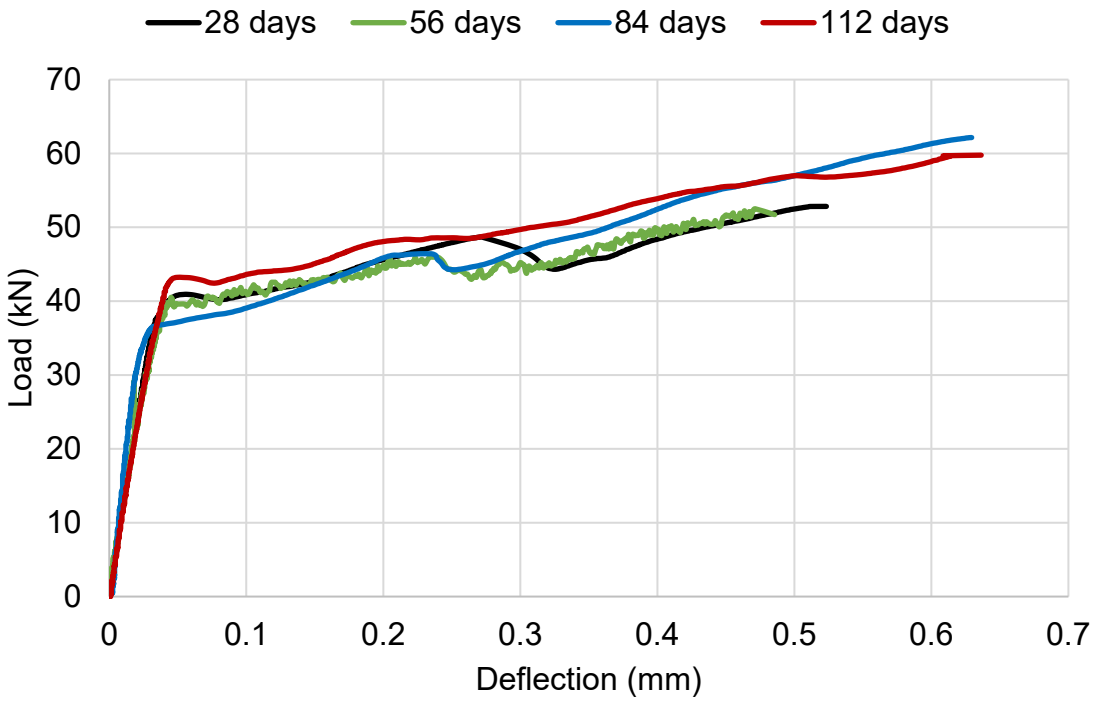

(b) Specimens immersed in room temperature (RT) for different durations

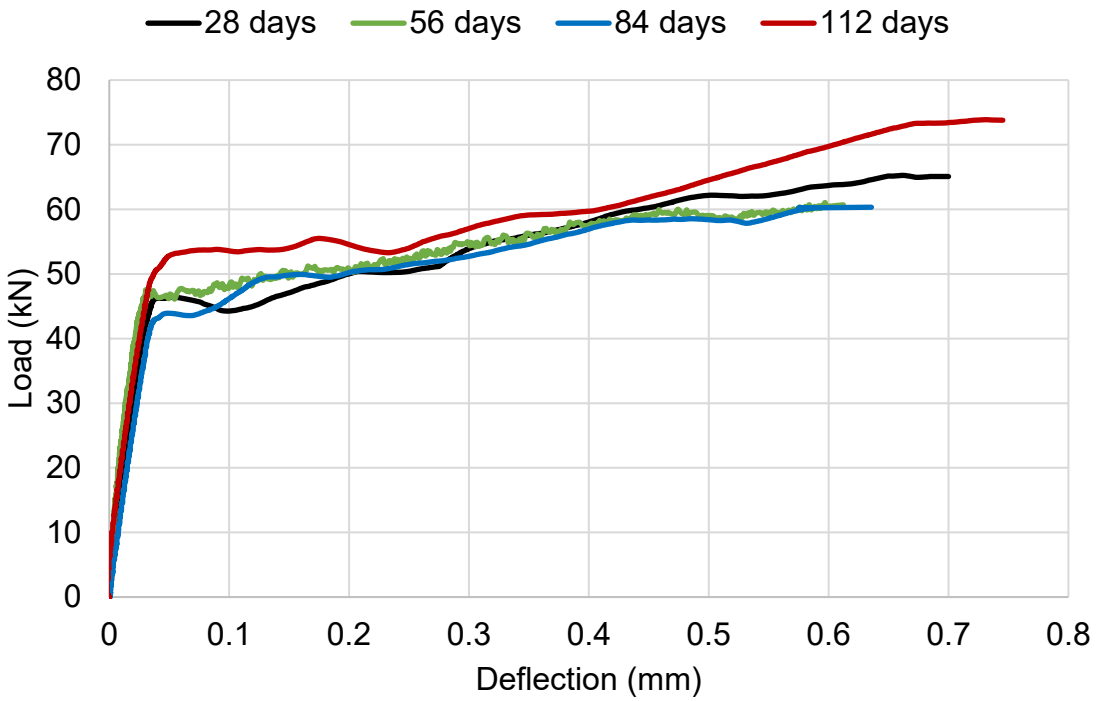

(c) Specimens immersed in moderate temperature (MT) for different durations

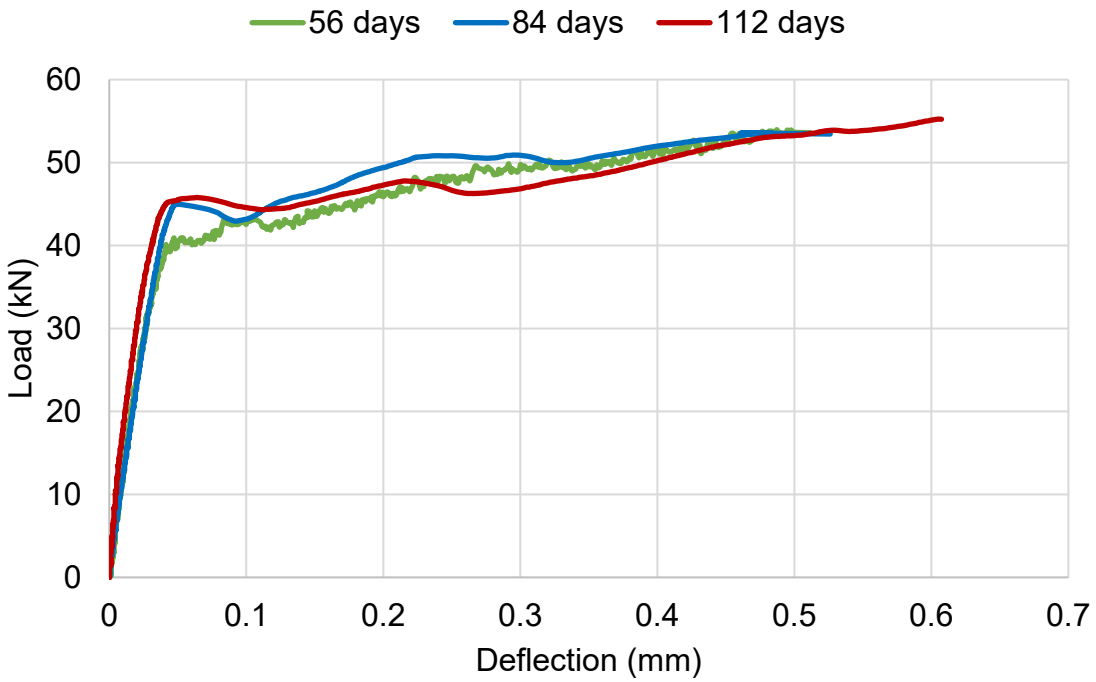

(d) Specimens immersed in high temperature (HT) for different durations

Figure 4-21 Failure load versus deflection of specimens immersed in different exposures and durations

4.3.2.2 Failure modes

A schematic representation of the typical failure modes observed in concrete beams externally bonded with CFRP is shown in Figure 4-22. The failure modes are termed (a) FRP rupture, (b) crushing of compressive concrete, (c) shear failure, (d) concrete cover separation at the end of the FRP laminate, (e) plate end interfacial debonding, and (f) intermediate-crack-induced interfacial debonding (Smith and Teng, 2002). The failure modes (a, b, and c) are similar to those in conventional reinforced concrete beams. The failure modes (d and e) are often referred to as premature debonding failure modes, which can be prevented by proper anchorage of the FRP laminate (ACI 440.2R-17, 2017).

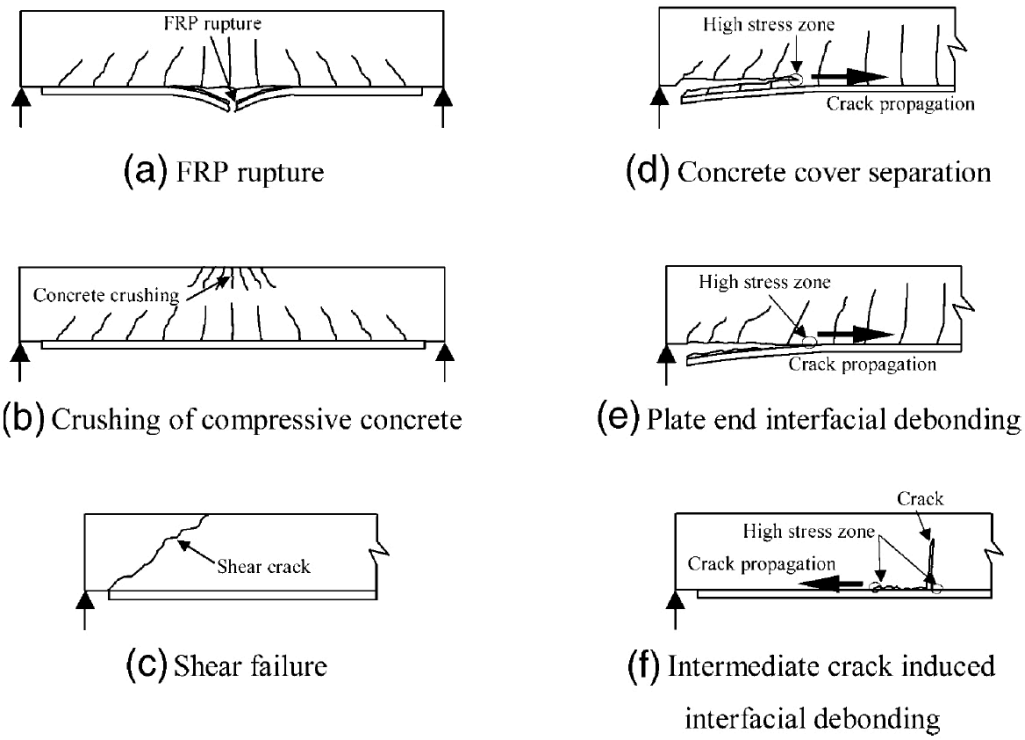

Figure 4-22 Failure modes of FRP-strengthened concrete beams (Smith and Teng, 2002)

The failure modes of the control specimens, revealed by the flexural tests, were mixed between the plate end interfacial debonding and concrete cover separation, as shown in Figure 4-23.

Figure 4-23 Failure modes from flexural tests of control specimens

Figure 4-24 shows the failure modes of specimens immersed in a room-temperature tank for 28, 56, 84, and 112 days. It can be noted that the failure modes associated with room-temperature specimens are plate end interfacial debonding or adhesive failure mode. Due to the abrupt termination of the FRP laminate, high interfacial

shear and normal stresses can develop at this region, which leads to the formation of a crack at or near the laminate end (Smith and Teng, 2002). Moderate temperature specimens also exhibited the plate end interfacial debonding, as shown in Figure 4-25.

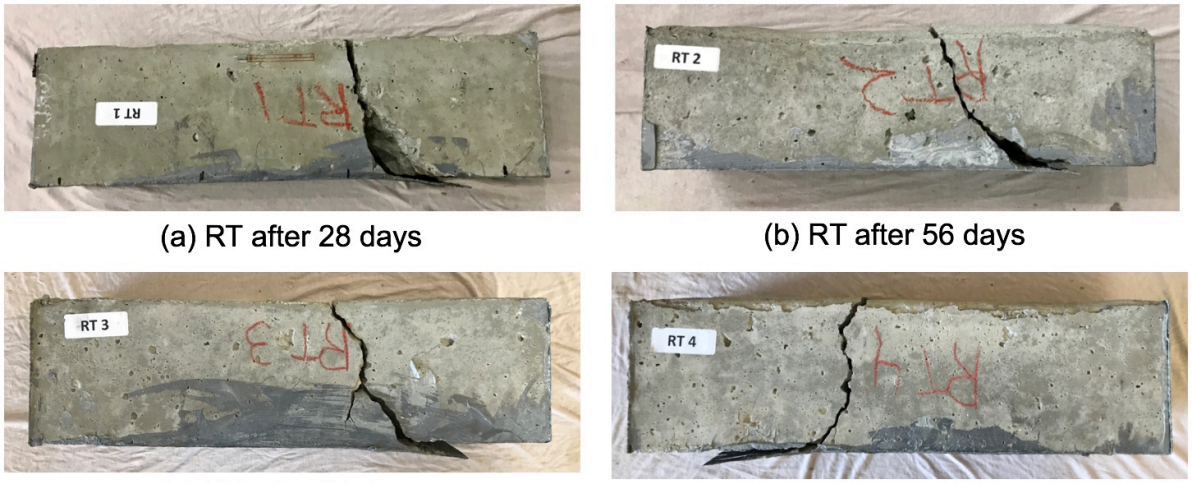

(a) RT after 28 days (b) RT after 56 days

(c) RT after 84 days (d) RT after 112 days

Figure 4-24 Failure modes from flexural tests of specimens immersed in room temperature for different durations

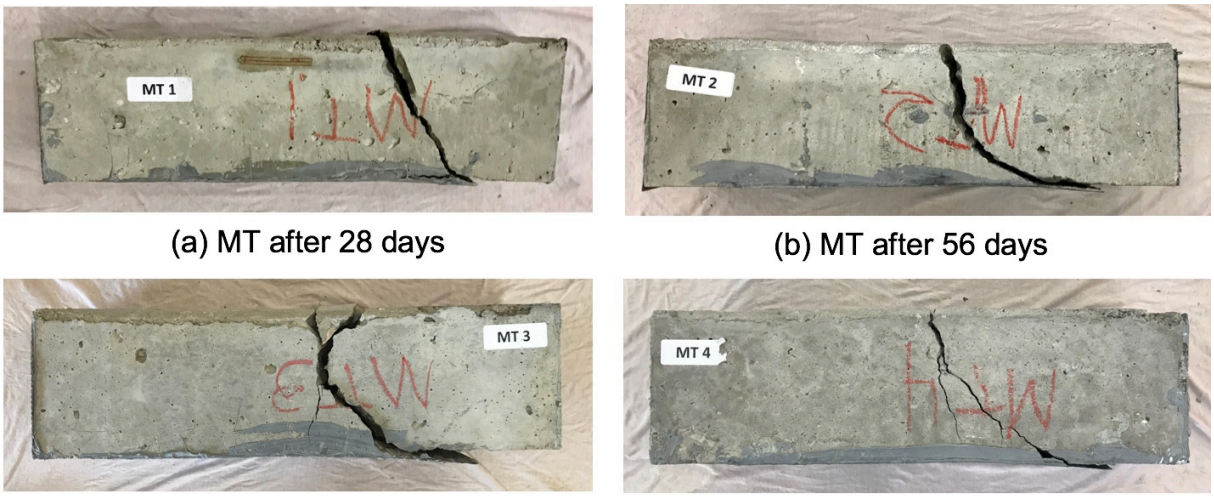

(a) MT after 28 days (b) MT after 56 days

(c) MT after 84 days (d) MT after 112 days

Figure 4-25 Failure modes from flexural tests of specimens immersed in moderate temperature for different durations

The failure modes revealed by the flexural tests for specimens immersed in the high-temperature tank for 28, 56, 84, and 112 days are shown in Figure 4-26. Due to the

lack of transverse reinforcements, shear failure was the most prevalent form of failure. To avoid shear failure, adequate shear strength should be provided to resist the applied shear forces. Additionally, FRP laminates oriented transversely to the section can be used to prevent shear failure (Esfahani et al., 2007).

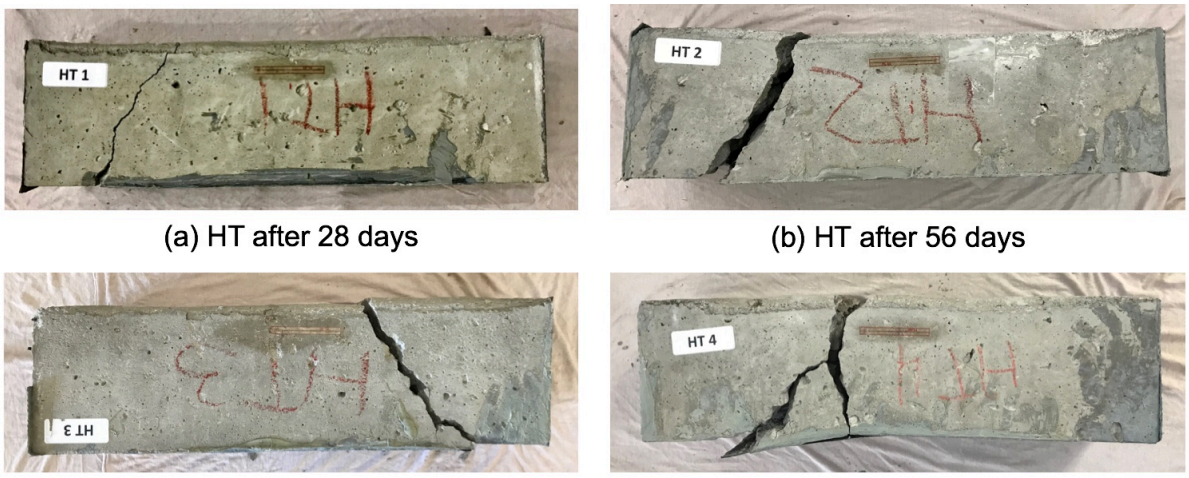

(a) HT after 28 days (b) HT after 56 days

(c) HT after 84 days (d) HT after 112 days

Figure 4-26 Failure modes from flexural tests of specimens immersed in high temperature for different durations

4.3.2.3 Comparison between theoretical and experimental loading capacity

The theoretical flexural capacity of each beam was calculated using ACI 440.2R (2017) provisions, as per Eq. (4-22). The manufacturer design values and the results obtained from CFRP coupons (subsection 4.1) were used. The calculated CFRP capacity was added to the concrete cracking moment to obtain the total beam capacity.

$$M_n = \Psi_f A_f f_{fe} \left(d_f - \frac{\beta_1 c}{2}\right) \quad (4\text{-}22)$$

where: M_n = nominal flexural capacity,

Ψ_f = CFRP strength reduction factor (0.85 for flexure),

A_f = area of CFRP external reinforcement,

f_{fe} = effective stress in the CFRP,

d_f = effective depth of CFRP flexural reinforcement

c = distance from extreme compression fiber to the neutral axis, and

β_1 = ratio of depth of equivalent rectangular stress block to depth of the neutral axis.

The comparison between theoretical and experimental loading capacity was obtained as listed in Table 4-11.The procedures of calculating the theoretical loading capacity is described in Appendix D. It can be seen from Table 4-11 that the theoretical loading capacity is underestimate the contribution of CFRP laminate towards concrete flexural capacity. Specimen immersed in MT (45 °C) for 112 days had 39% lower capacity than experimental result. Similar conclusion was found here (Yazdani et al., 2020).

Table 4-11 Comparison between theoretical and experimental loading capacity

Specimen	Experimental Failure Load		Theoretical Failure Load		Failure mode	% Difference
	kN	(kips)	kN	(kips)		
Control	50.9	(11.5)	50.1	(11.3)	CFRP delamination	-2%
Specimen immersed in RT (23 °C) for 112 days	59.8	(13.4)	53.0	(11.9)		-11%
Specimen immersed in MT (45 °C) for 112 days	73.8	(16.6)	48.4	(10.9)		-34%
Specimen immersed in HT (60 °C) for 112 days	55.2	(12.4)	51.9	(11.7)		-6%

4.3.2.4 Evaluation of modulus of rupture

The strength of concrete beams enforced with CFRP laminate was evaluated by the modulus of rupture (MOR) in accordance with ASTM Standard C78/C78M 2010. For the calculation of MOR, Eq. (4-23) was utilized:

$$MOR = \frac{PL}{bd^2} \tag{4-23}$$

where: MOR = modulus of rupture,

P = the maximum applied load indicated by the testing machine,

L = the span length between bottom supports,

b = the width of the specimen, and

d = the depth of specimen.

The comparison between the modulus of rupture for each exposure regime and exposure time is illustrated in Figure 4-27. On the 112th day of exposure, the improvements in modulus of rupture of CFRP bonded to concrete beams when compared with their initial value were 20%, 49%, and 11% at 23, 45, and 60 °C, respectively. The improvement in the modulus of rupture resulted from the concrete curing over time. Also, by comparing the failure modes of CFRP bonded to concrete beams, it was observed that the CFRP laminates remained intact at the failure moment.

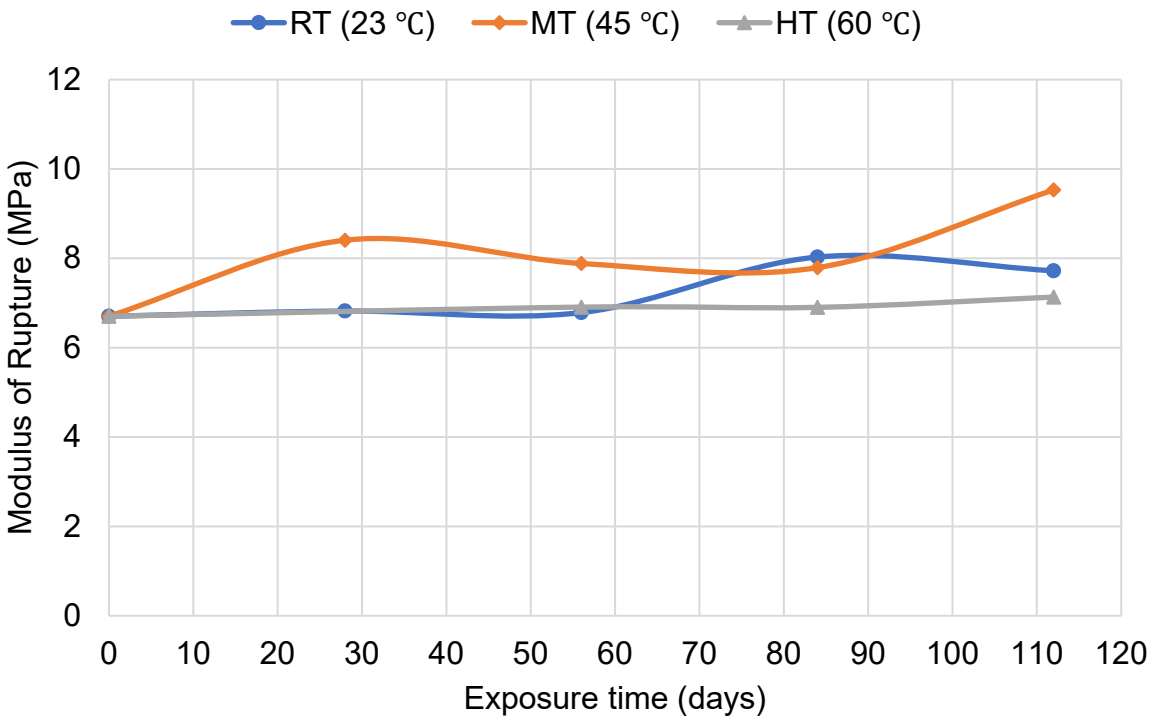

Figure 4-27 Modulus of rupture of the environmental conditions versus exposure time

4.3.3 Compression Test Results

The comparison between the compressive tests conducted on concrete cylinders for each exposure regime and exposure time is illustrated in Figure 4-28. On the 112th day of exposure, the enhancements in the compressive strength of the cylinders, when compared with their initial value, were 55% and 16% at 45 and 60 °C, respectively. However, the room-temperature cylinders exhibited almost the same strength as their initial value. It can be noted that the compressive strength of the moderate-temperature cylinders increased over time. The improvement in the compressive strength was a result of concrete curing over time. Figure 4-29 shows the compressive strength tests of some of the capped concrete cylinders before and after the test.

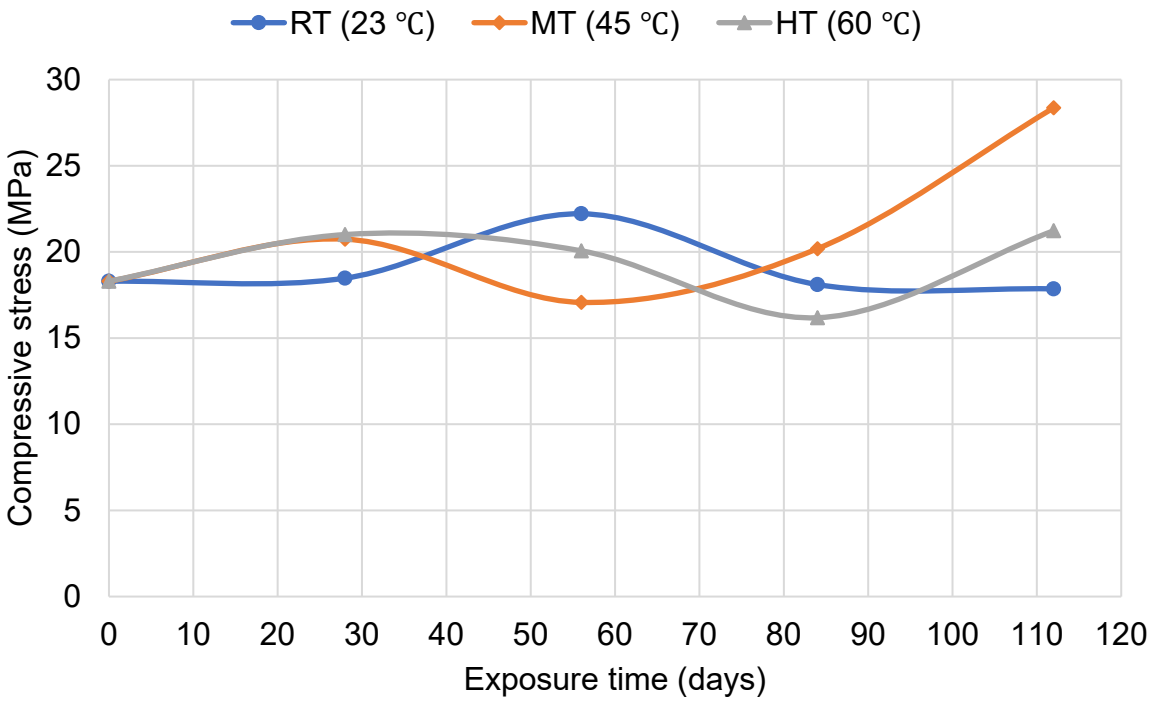

Figure 4-28 Ultimate compressive stress of concrete cylinders of different environmental conditions versus exposure time

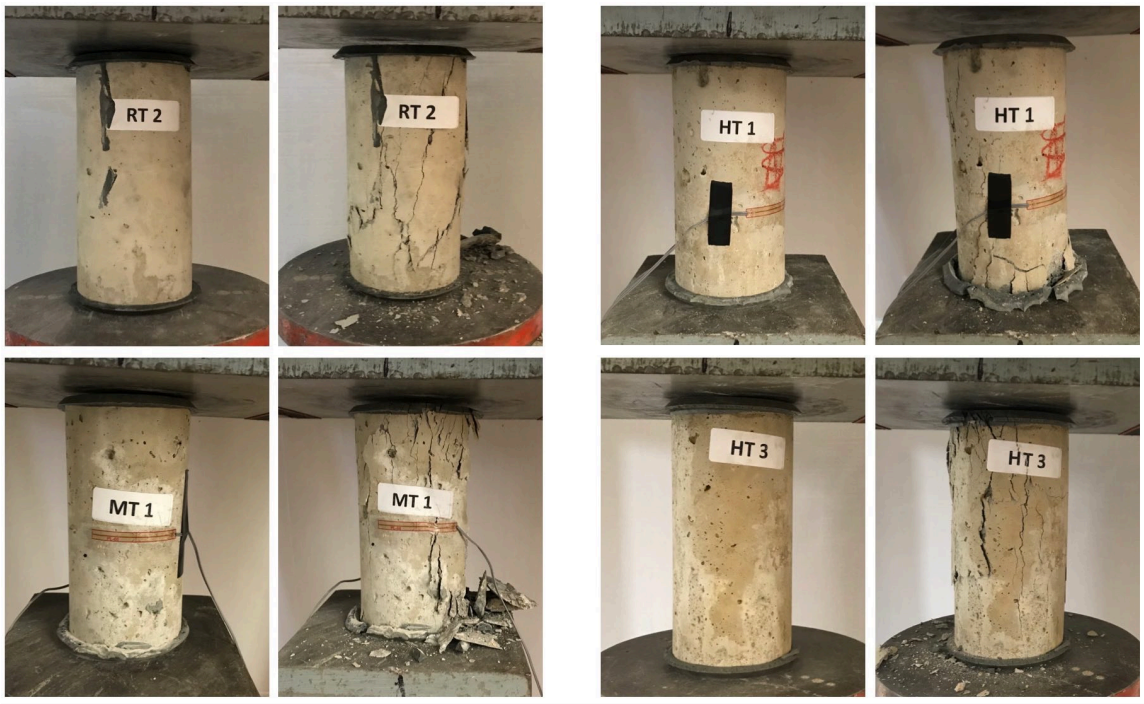

Figure 4-29 Concrete compressive strength test, before and after the test

4.3.4 Comparison Between Flexure, Pull-off, and Compression Results

The relationships between the results of the flexural, pull-off, and compressive tests for different environmental conditions and durations are presented in Figure 4-30. Overall, for room temperature exposure, the normalized strength for all test results seemed to be consistent over time, as seen in Figure 4-30 (a); however, minimal improvement in the flexural strength was observed after 112 days of exposure. For the moderate temperature condition, as shown in Figure 4-30 (b), there was a clear upward trend in the normalized strength of flexural and compressive results as exposure time increased. This was due to concrete curing over time. Conversely, for pull-off results, it can be seen that the normalized strength fell slightly from 28 to 84 days of exposure, which can be attributed to the presence of failure mode A during this period.

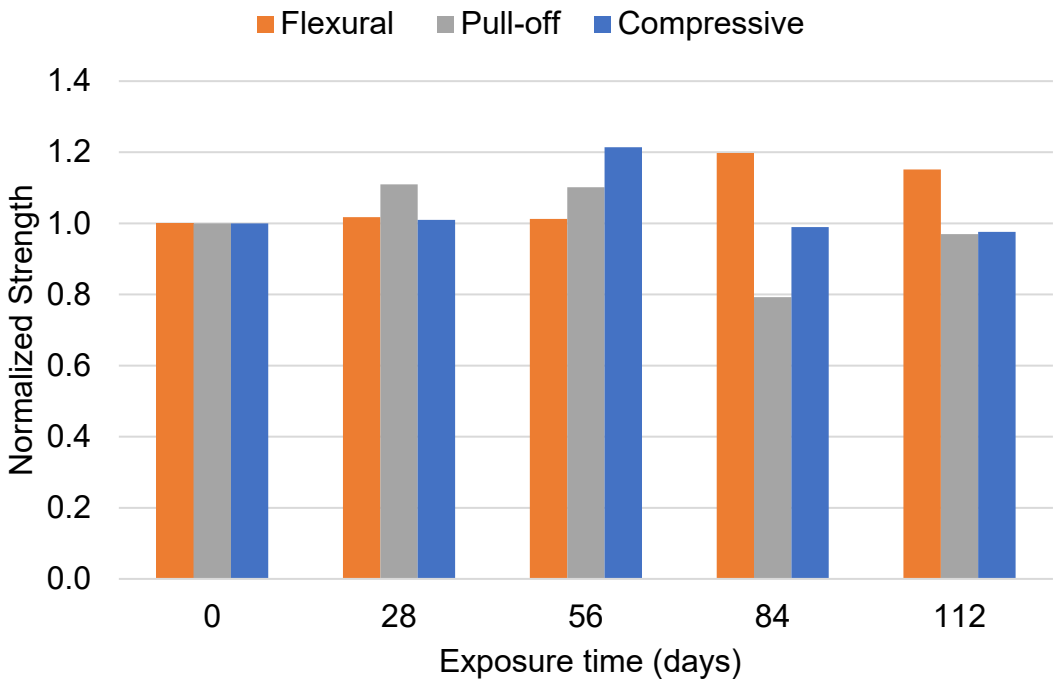

(a) Environmental condition: RT (23 °C)

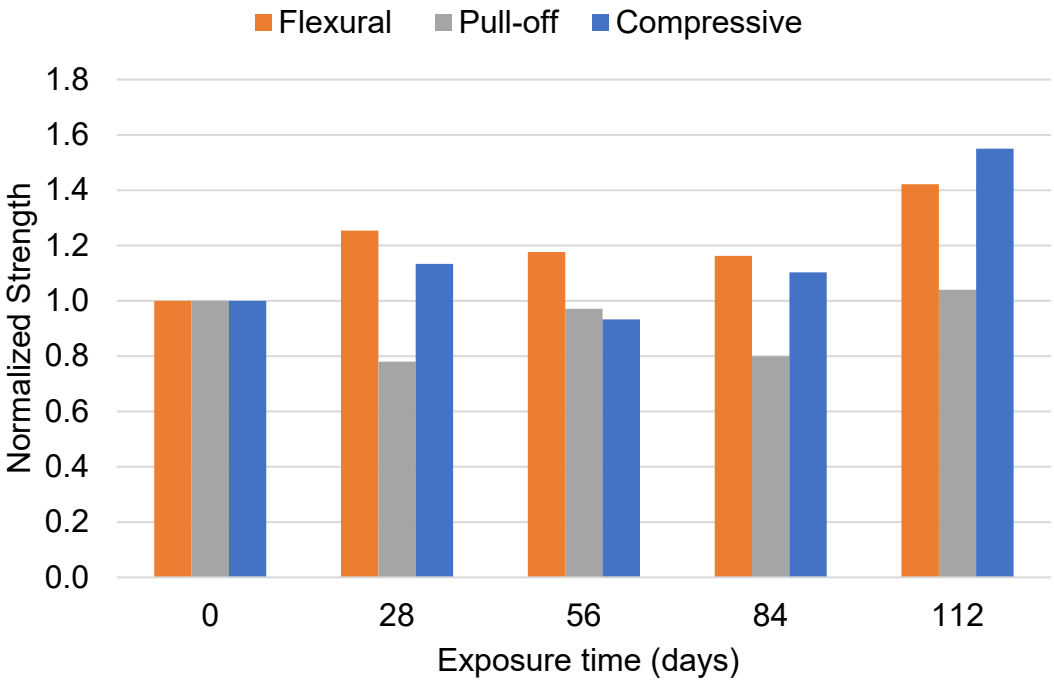

(b) Environmental condition: MT (45 °C)

The normalized strength portrayed by the results of the pull-off and compressive tests increased, then decayed, which showed its inconsistent behavior over time. However, the normalized strength of the compressive result showed a growth of 18% after 112 days. For flexural results, the was no clear trend over the exposure time.

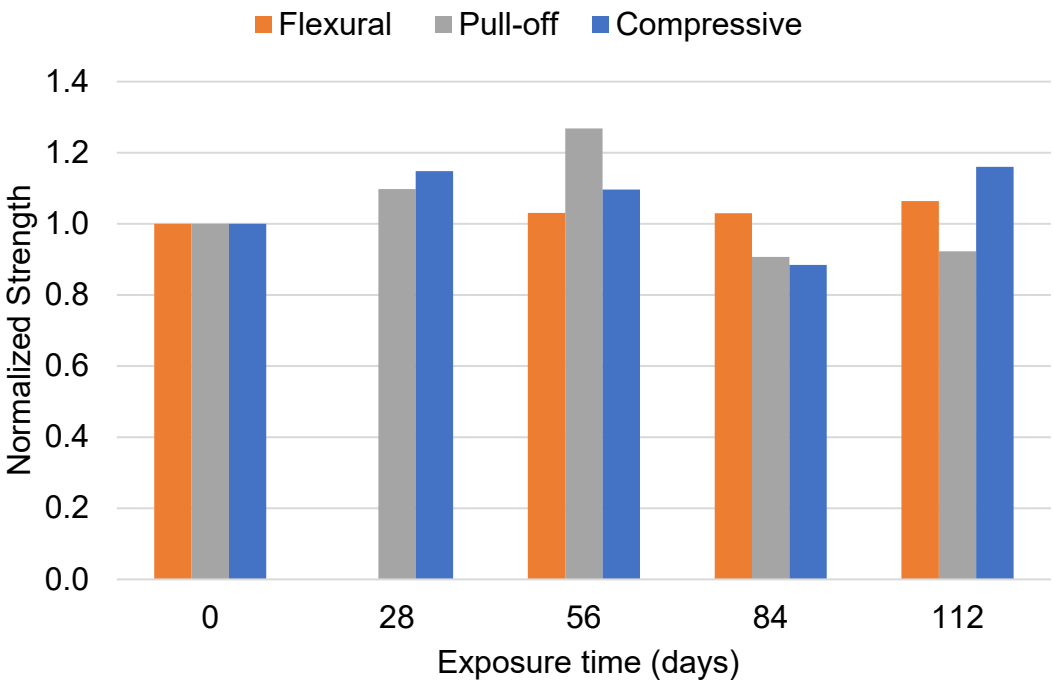

(c) Environmental condition: HT (60 °C)

Figure 4-30 Relationship between flexural, pull-off, compressive test results for different environmental conditions and durations

Chapter 5. Finite Element Modeling

A concrete beam externally bonded with carbon fiber reinforced polymer (CFRP) consists of three major components: concrete, CFRP, and adhesive matrix. The nonlinear analysis of the system is comprised of complications from concentrated stresses and cracks behavior. Hence, a complete analysis model of finite element (FE) software (ABAQUS) was implemented by selecting a suitable numerical approach, modeling each material according to precise rules, and modeling the interaction between the concrete surface and the CFRP. The following sub-sections provide information about each component.

5.1 Material Properties

5.1.1 Concrete

Several models have been used to characterize concrete behavior. One of the models is a smeared crack model, which is based on the principal tensile stress and tensile strength of the concrete (Pham et al. 2006). The concrete damage plasticity (CDP) model has also been used successfully to predict concrete behavior, as it simulates concrete that has two failure modes: compressive crushing and tensile cracking (Obaidat et al. 2010).

5.1.1.1 Concrete Compressive Behavior

The uniaxial stress-strain behavior of concrete in compression is shown in Figure 5-1. In this model, the stress of concrete is assumed to be linear with the strain until the value of initial yield, σ_{c0}. In the inelastic regime, the response is affected by stress hardening, as well as strain softening, beyond the ultimate stress, σ_{cu}, (Simulia, 2014).

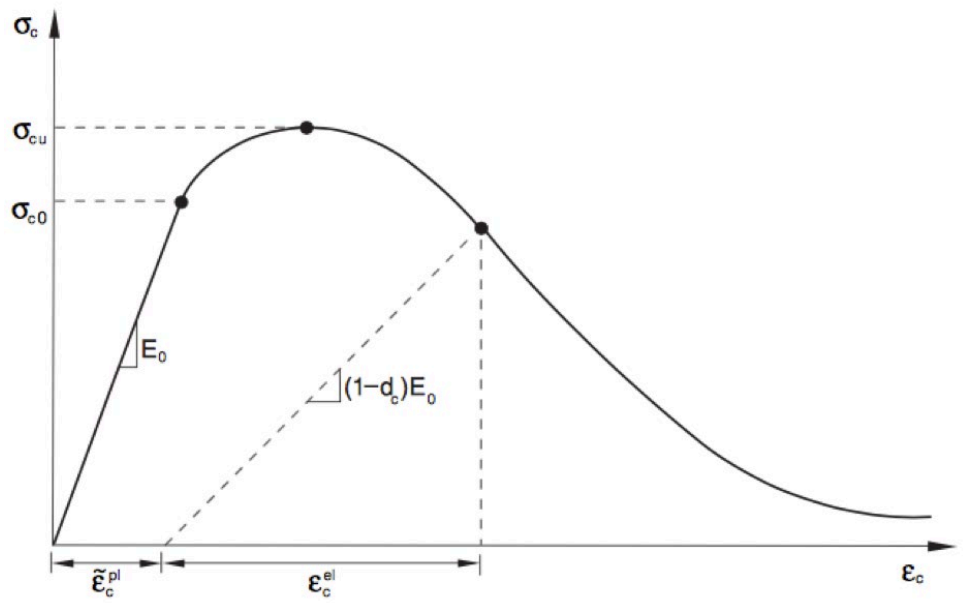

Figure 5-1 Response of concrete to uniaxial loading in compression (Simulia, 2014)

The material properties of concrete, used in the finite element model, were acquired from the experimental tests conducted in the laboratory. The average peak compressive strength of concrete, f_c', was 28.5 MPa (4.13 ksi). The initial tangential modulus, E_0, concrete modulus of elasticity (Young's modulus), was calculated by Eq. (5-1):

$$E_c = 4700\sqrt{f_c'} = 4700\sqrt{28.5} = 25091 \text{ MPa} = 3639 \text{ ksi} \quad (5\text{-}1)$$

5.1.1.2 Concrete Tensile Behavior

The uniaxial stress-strain behavior for concrete in tension is represented in Figure 5-2. Similar to the compression behavior, the tensile stress of concrete is assumed to be linear with the strain until the value of failure stress, σ_{t0}. The tensile failure stress corresponds to the beginning of micro-cracking in the concrete material. After the tensile failure stress, the development of micro-cracks is characterized by a softening stress-strain response (Simulia, 2014). The tensile strength, f_{ct}, can be calculated by Eq. (5-2):

$$f_{ct} = 0.33\sqrt{f_c'} = 0.33\sqrt{28.5} = 1.76\ MPa = 255\ psi \quad (5\text{-}2)$$

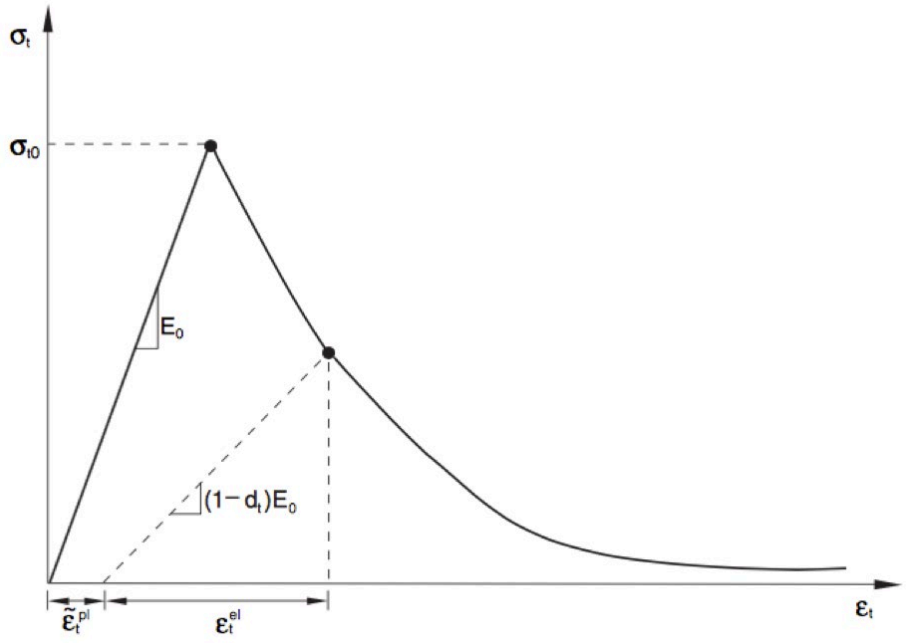

Figure 5-2 Response of concrete to uniaxial loading in tension (Simulia, 2014)

5.1.2 Fiber Reinforced Polymer (FRP)

Fiber reinforced polymer (FRP) composites consist of high strength fibers embedded in a binding agent or matrix resin, as presented in Figure 5-3. The strength and elasticity of the FRP depend on the mechanical properties of both the fiber and matrix, number of layers, fiber orientation within the matrix, and their volume relative to one another. The uniaxial behavior of the CFRP was assumed to be linear up to failure, as shown in Figure 5-4.

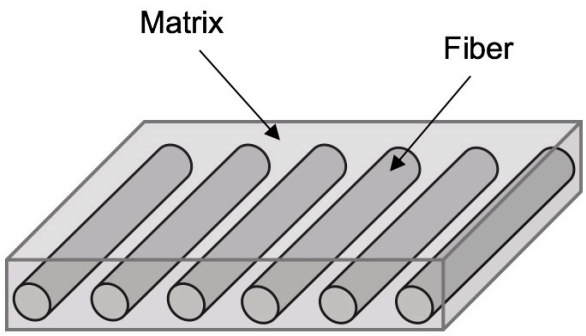

Figure 5-3 Schematic view showing the typical unidirectional FRP laminate

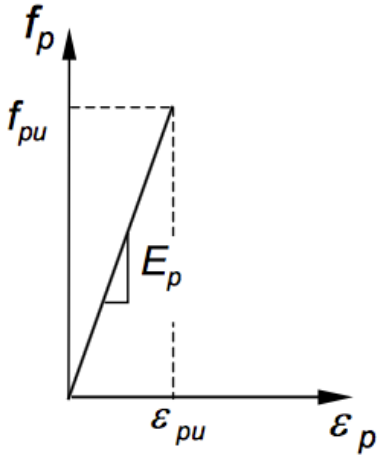

Figure 5-4 Idealized stress-strain relationship for CFRP composites (Breña et al. 2001)

5.1.2.1 Fiber selection: High strength carbon

The properties of high strength carbon fiber were found in the datasheet of SikaWrap® Hex-117C (Sika Corporation, 2018). Since the Poisson's ratio was not specified in the manufacturer datasheet, the number resulting from the research conducted by Krucinska & Stypka (1991) was used to measure the axial Poisson's ratio of single carbon fibers. The Poisson's ratio of carbon fiber was 0.27 based on an average of the same grade of fibers as was used in the research (Table 5-1). The effective elastic properties of unidirectional high strength carbon fiber are listed in Table 5-2.

Table 5-1 Mechanical properties of fibers (Krucinska and Stypka, 1991)

Type of Fiber	Mean diameter (μm)	Tensile strength (GPa)	Young's modulus (GPa)	Breaking strain (%)	Poisson's ratio
38/III	8.22	2.74	196.7	1.39	0.27
WS/2/3	7.68	4.70	224.0	2.10	0.26
Safril	7.61	3.03	194.2	1.56	0.28

Table 5-2 Effective elastic properties of unidirectional high strength carbon fiber

Property	Value
Tensile strength, σ_f	550,000 psi (3,793 MPa)
Longitudinal modulus of elasticity, E_{lf}	34 x 10^6 psi (234,000 MPa)
Transverse modulus of elasticity, E_{tf}	3 x 10^6 psi (20,700 MPa)
Longitudinal shear modulus, G_{lf}	4 x 10^6 psi (27,600 MPa)
Transverse shear modulus, G_{tf}	1 x 10^6 psi (6,890 MPa)
Fiber elongation at break, ε_f	1.5 %
Fiber density, ρ_f	0.065 lb./in^3 (1.8 g/cc)
Poisson's ratio, ν_f	0.27

5.1.2.2 Matrix selection: Epoxy

The properties of the selected matrix (epoxy) were based on information from the Sika Corporation, (2014), but some elastic properties were obtained from the research conducted by Naganuma et al. (1999), as shown in Table 5-3. The effective elastic and thermoelastic properties of the epoxy are listed in Table 5-4.

Table 5-3 Properties of the pure epoxy matrix (Naganuma et al., 1999)

	Glass particle	Epoxy matrix
Refractive index, n ($\lambda = 800$ nm)	1.536	1.537
Young's modulus, E/GPa	86	2.8
Poisson's ratio	0.24	0.37
Density, ρ/g · cm^{-3}	2.64	1.17
Thermal expansion coefficient, $\alpha/10^{-6}$ K^{-1}	4.3	68

Table 5-4 Effective elastic properties of the epoxy

Property	Value
Tensile Strength, σ_M	4,900 psi (33.8 MPa)
Elongation at Break, ε_M	1.2 %
Flexural Strength	8,800 psi (60.6 MPa)
Flexural Modulus, E_M	5.06 x 10^5 psi (3,489 MPa)
Modulus of Elasticity, E_M	406,105 psi (2,800 MPa)
Shear Modulus, G_M	148,228 psi (1,022 MPa)
Poisson's ratio, ν_M	0.37
Matrix Density, ρ_M	0.042 lb./in^3 (1.17 g/cc)

5.1.3 CFRP - Concrete interface

The interface of CFRP and concrete has been studied by many researchers (Lu et al. 2005; Obaidat et al. 2013) and was simulated in a traction-separation model (TSM). TSM is a linear elastic relationship between shear stress, τ, and slippage (separation), δ, followed by the initiation and evolution of damage, as shown in Figure 5-5. The initial stiffness, K_0, was utilized by Eq. (5-3):

$$K_0 = 0.16\frac{G_m}{t_m} + 0.47 \quad (5\text{-}3)$$

where t_m = the matrix thickness, and

G_m = the shear modulus of matrix.

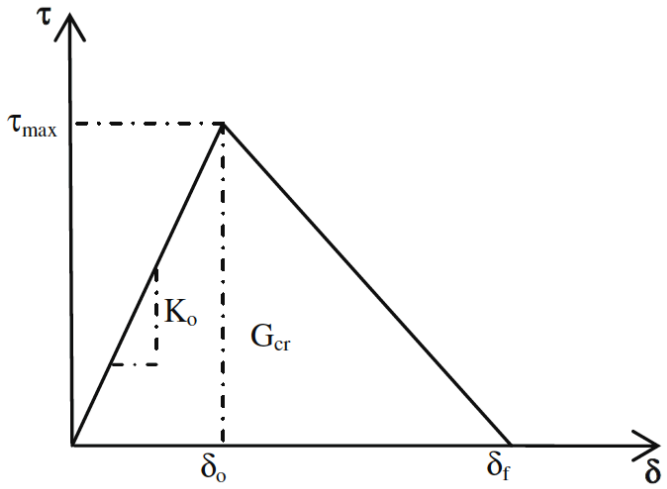

Figure 5-5 Bilinear traction - separation constitutive law (Obaidat et al, 2010)

The maximum shear stress, τ_{max}, and the corresponding slip, δ_0, were calculated by Eq. (5-4) and Eq. (5-5), respectively:

$$\tau_{max} = 1.46 \times {f_{ct}}^{1.033} \times {G_m}^{0.165} \quad (5\text{-}4)$$

$$\delta_0 = 0.0195\beta_w f_{ct} \quad (5\text{-}5)$$

where f_{ct} = the concrete tensile strength, and

β_w = the expression of the width ratio factor and given by Eq. (5-6):

$$\beta_w = \sqrt{\frac{2.25 - \frac{b_f}{b_c}}{1.25 + \frac{b_f}{b_c}}} \quad (5\text{-}6)$$

Where: b_f = the CFRP sheet width, and

b_c = the concrete width.

The interfacial fracture energy, G_f, needed for opening the crack can be calculated by Eq. (5-7):

$$G_f = 0.52 \times f_{ct}^{0.26} \times \mathrm{G}_m^{-0.23} \quad (5\text{-}7)$$

5.2 Element Types

The ABAQUS library has many types of elements, as shown in Figure 5-6. One of them is the eight-node linear brick element model (C3D8R) that was assigned to the concrete beam part. A four-node double curved thin shell (S4R) membrane element was selected for the CFRP part.

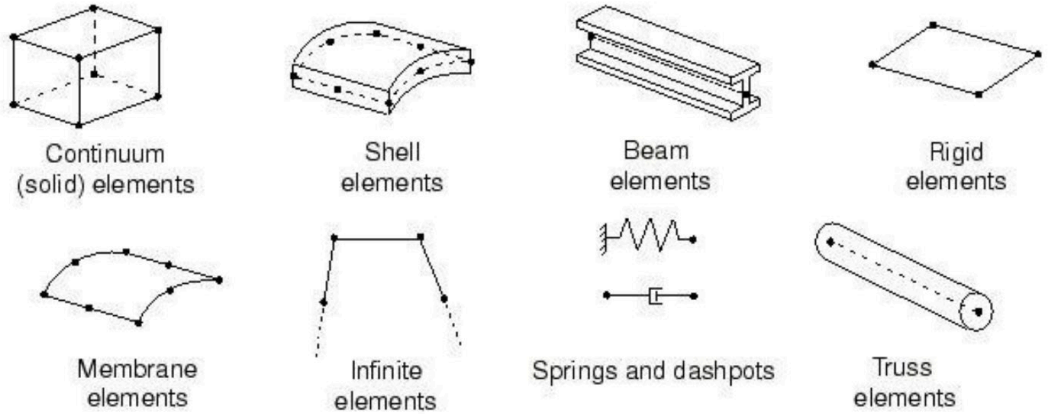

Figure 5-6 Various element types (Cohen, 2018).

5.3 Model Geometry

The geometries of the concrete beam and CFRP sheet modeled by ABAQUS were similar to the actual experiment conducted in the laboratory. A three-dimensional FEM model was created, as shown in Figure 5-7.

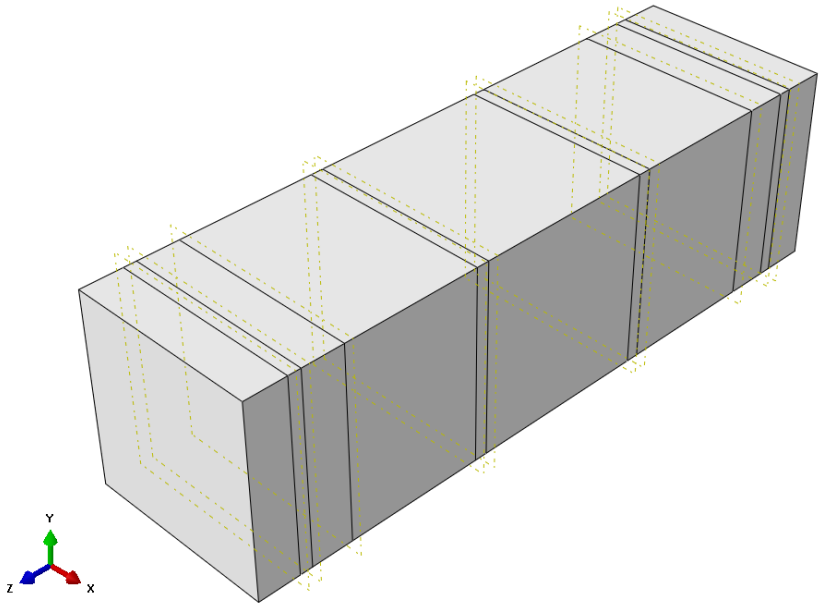

Figure 5-7 Geometry of ABAQUS model

5.4 Boundary Conditions and Loads

The CFRP bonded to the concrete beam was modeled as the experimental test (i.e., a simple support beam). The boundary conditions of the ABAQUS model were defined as a hinge for one side and a roller for the other side to simulate the experimental condition. Two concentrated loads of equal values were applied to one-third of the span, as shown in Figure 5-8.

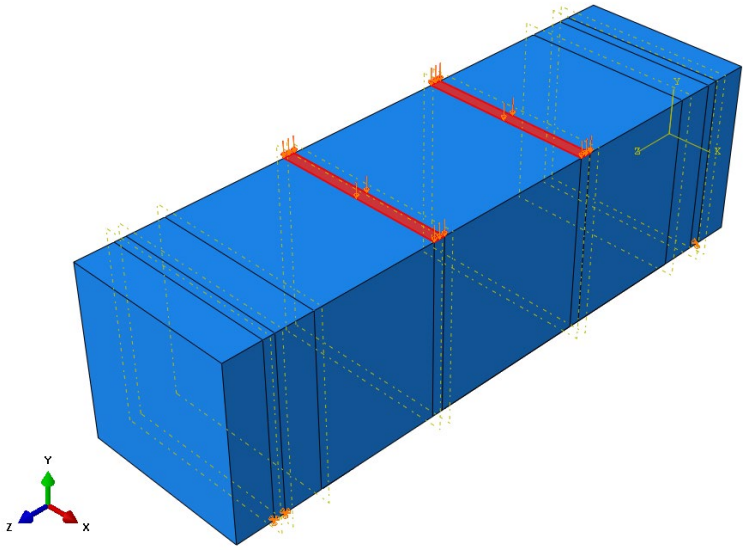

Figure 5-8 Boundary conditions and loading surface of the model

5.5 Meshing the Parts

Numerous attempts were made to choose the optimum element size. Fine mesh can accurately simulate experimental results, but ABAQUS could abort during the analysis. Therefore, a mesh size of 12 mm (0.47 inch) was implemented in the model for both the concrete beam and the CFRP, as shown in Figure 5-9.

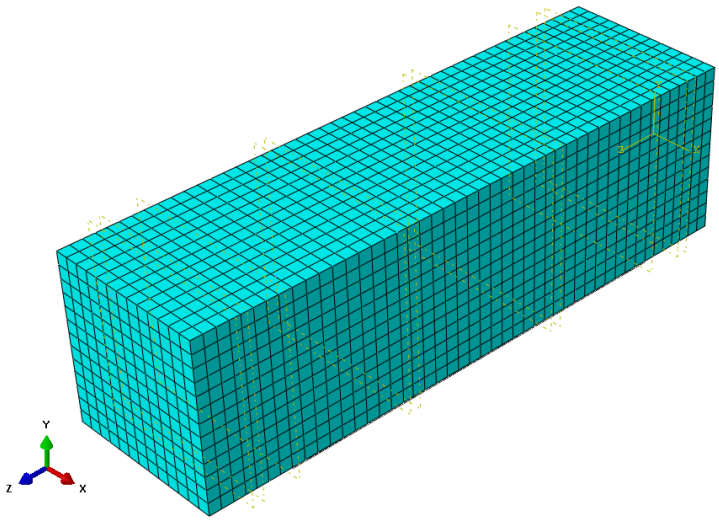

(a) Finite element mesh used for the concrete beam

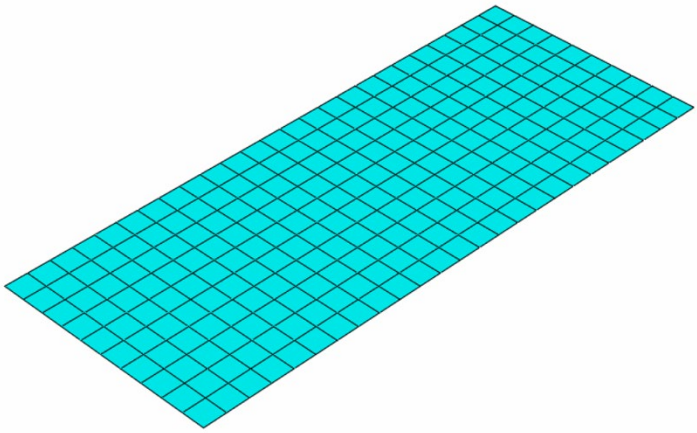

(b) Finite element mesh used for the CFRP sheet

Figure 5-9 Finite element mesh used for the parts

5.6 Analysis Outputs and Implementation

A static-general step was created to perform the nonlinear solution. The time period was the default value of one second, and the initial increment time was 1×10^{-3} second. The minimum increment time used in the model was 1×10^{-15} second to avoid a diverged solution. The geometric nonlinearity setting was turned on during the step to include the nonlinear effects of large deformations and displacements. After the model was submitted and completed, the results for the output history were obtained and compared with the experimental results for calibration purposes.

5.7 Model Adjustment and Calibration

The preliminary model was based on theoretical values acquired from previous studies; the actual experimental results were not taken into consideration. It was, therefore, essential to adjust the finite element model to accurately reflect each of the elements used in the experiment.

5.7.1 Calibration of Concrete Material

The properties of the concrete were the first part of the model to be calibrated. Thus, five concrete cylinders were tested to find the compressive strength of the control specimens, as per ASTM C39 (2010). Table 5-5 lists the results of the compressive strength of the control cylinders.

Table 5-5 Compressive strength of control specimens

Specimen	Compressive strength (ksi)	Compressive strength (MPa)
C1	2.66	18.32
C2	2.87	19.79
C3	4.13	28.48
C4	2.71	18.68
C5	4.15	28.61
Average	3.30	22.78

The average peak compressive strength of the concrete, f_c', was 22.78 MPa (3.3 ksi). Later, another 20 concrete cylinders were tested to determine the effects of the exposure conditions. According to ACI 318R (2014), the initial tangential modulus, E_c, concrete modulus of elasticity (Young's modulus), was calculated by Eq. (5-8):

$$E_c = 4700\sqrt{f_c'} = 4700\sqrt{22.78} = 22432 \text{ MPa} = 3254 \text{ ksi} \quad (5\text{-}8)$$

5.7.2 CFRP Calibration

The properties of the CFRP were the second part of the model to be calibrated. A unidirectional fibrous composite consists of a fiber sheet bonded with two layers of epoxy matrix, as exhibited in Figure 5-10. The thickness of the carbon fiber fabric and the CFRP laminate were measured to calculate the fiber concentration (c), as shown in Figure 5-11.

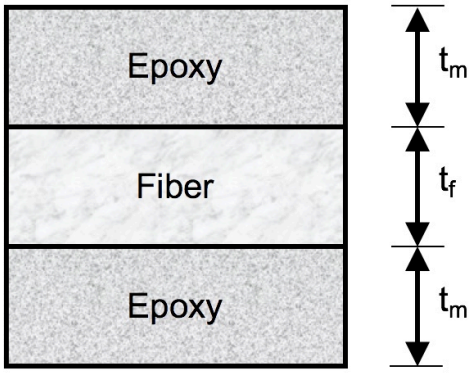

Figure 5-10 One-layer scheme of the CFRP laminate

(a) (b)

Figure 5-11 Thickness measurement: (a) measure the carbon fiber sheet, (b) measure the CFRP laminate after failure

The fiber concentration (c) can be calculated by Eq. (5-9):

$$c = \frac{V_f}{V} \tag{5-9}$$

where: V_f = the volume occupied by fiber, and

V = the total volume.

Since a unidirectional fibrous composite can be treated as a lamina, the width and depth can be neglected in calculating the fiber concentration. Hence, Eq. (5-9) can be modified to Eq. (5-10) as follows:

$$c = \frac{t_f}{t} \tag{5-10}$$

where: t_f = the fiber thickness, and

t = the total thickness of the laminate.

By measuring the thickness of the fiber sheet and CFRP laminate, it was found that the fiber concentration was 44.4%. The main purpose of calculating the fiber concentration was to obtain the exact value of modulus of elasticity from Figure 5-12.

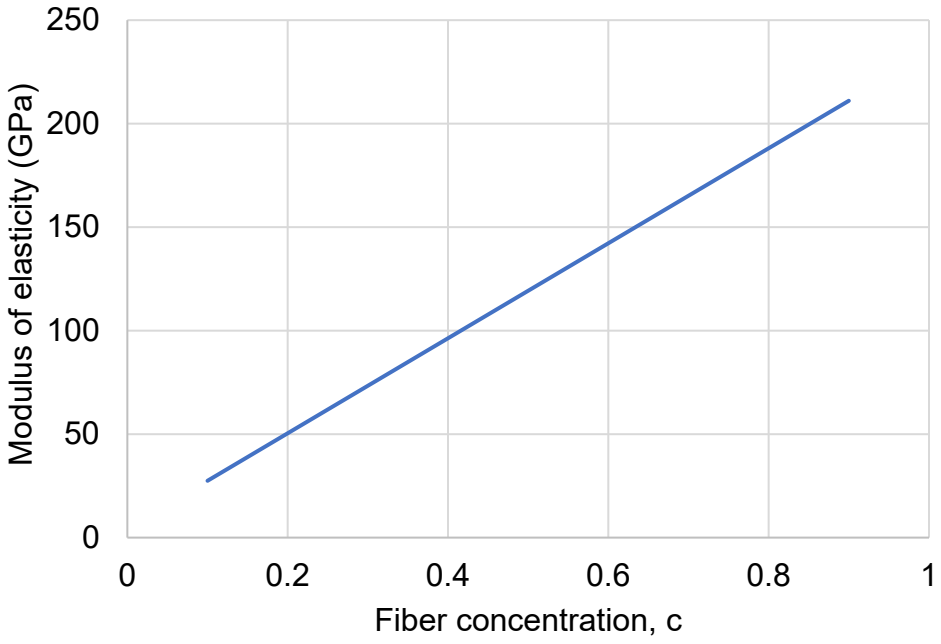

Figure 5-12 Longitudinal Young modulus vs fiber concentration

5.8 Comparison with Experimental Results

A series of iterations were performed to calibrate the load-deflection curves of the model with experiment results. For each iteration, the parameter values were adjusted to reach a comparable failure load and deflection corresponding to the experimental results. The load-deflection curves obtained for the control specimen and FEM analysis are shown in Figure 5-13. In terms of failure load and maximum displacement, it can be noted that there was good agreement between the FEM and experimental results. The load-deflection curves obtained for room, moderate, and high temperatures specimens after 112 days of exposure and FEM analyses are shown in Figure 5-14. RM, MT, and HT are denoted for room, moderate, and high temperatures, respectively.

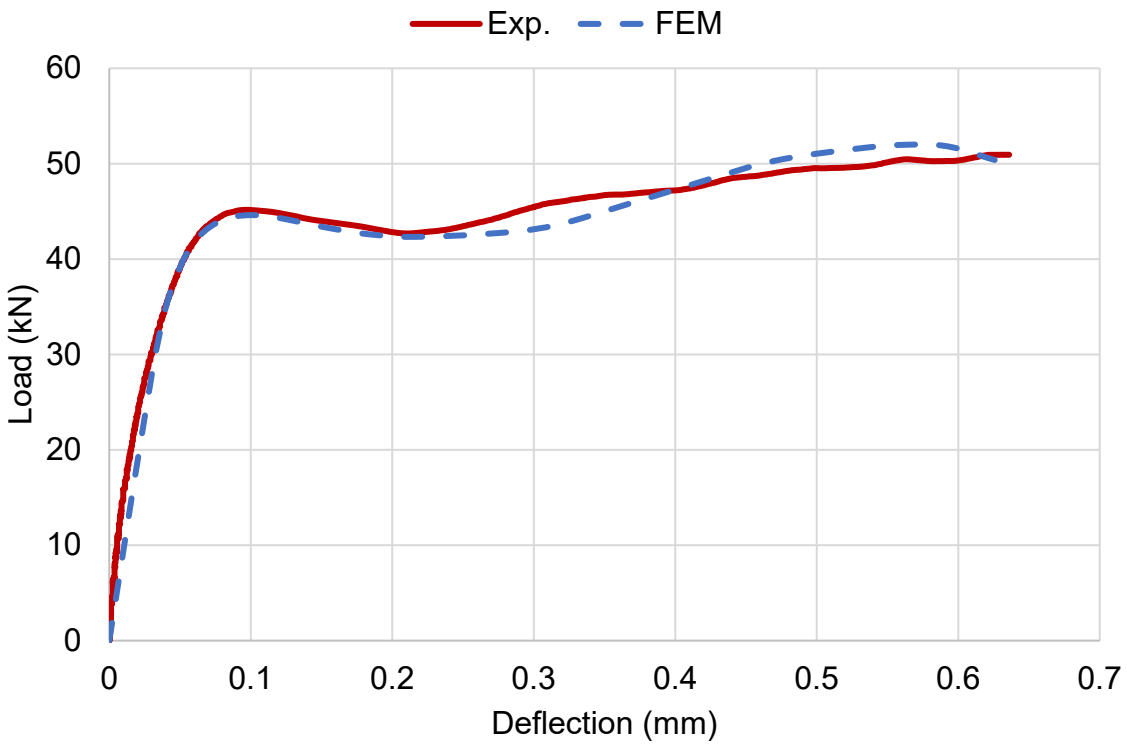

Figure 5-13 Load-deflection curves of experimental control specimen and FEM

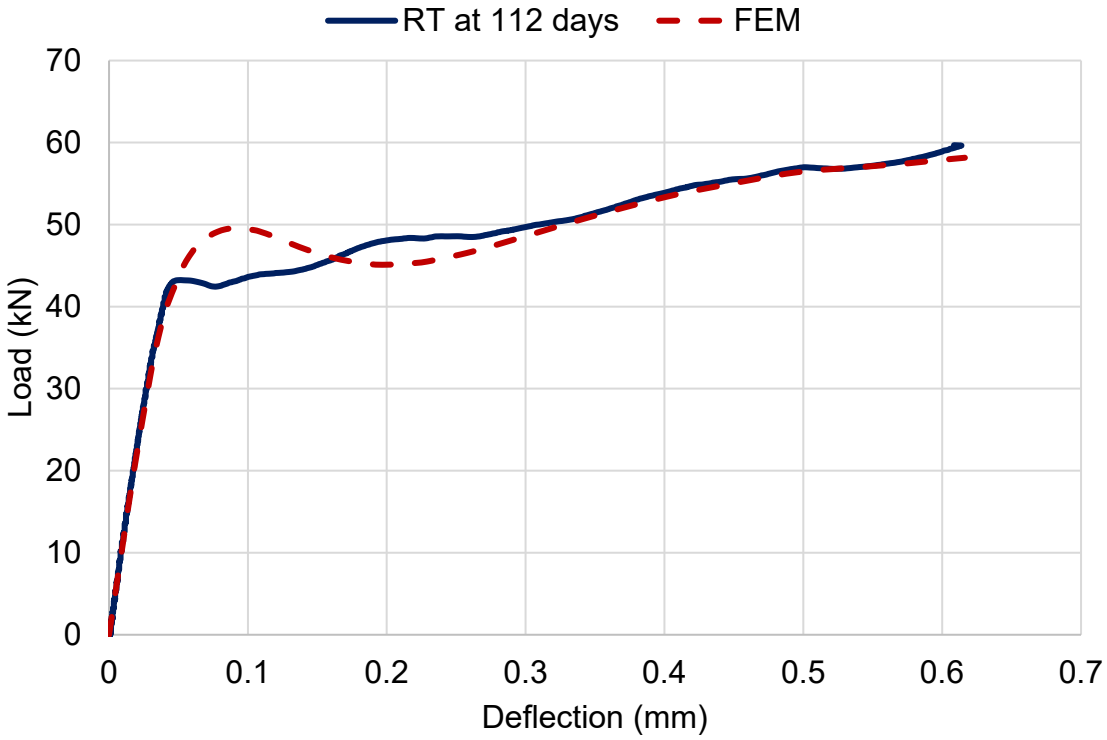

(a) Load-deflection curves of specimen aged in RT for 112 days and FEM

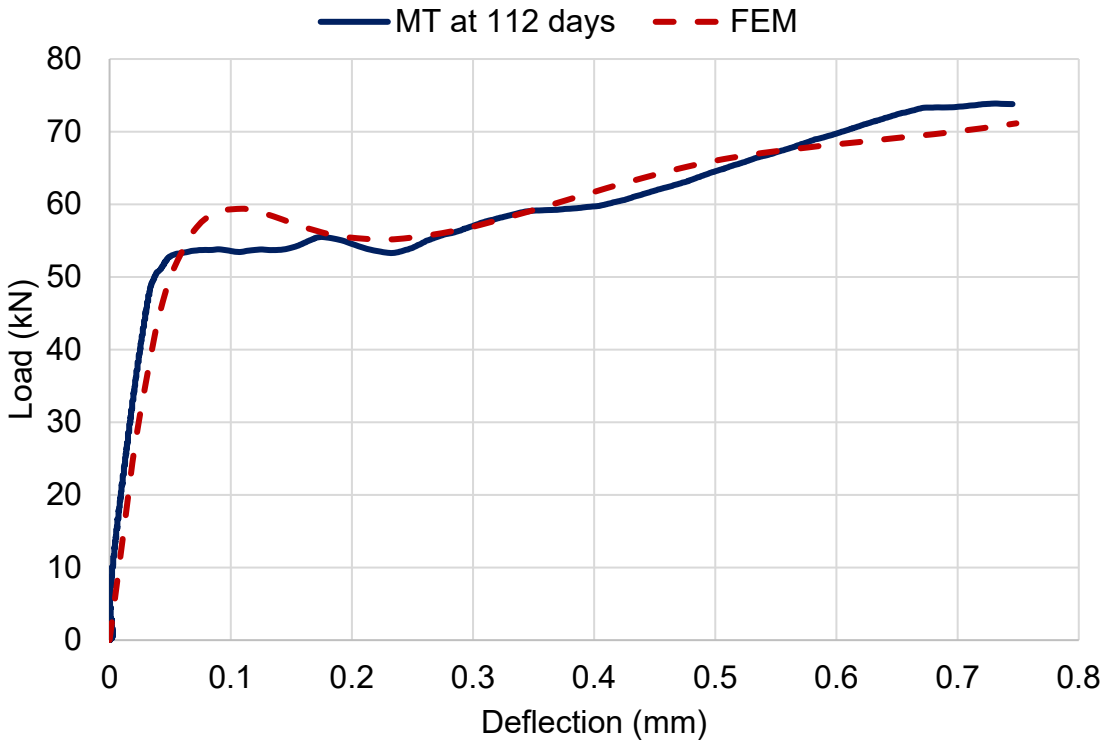

(b) Load-deflection curves of specimen aged in MT for 112 days and FEM

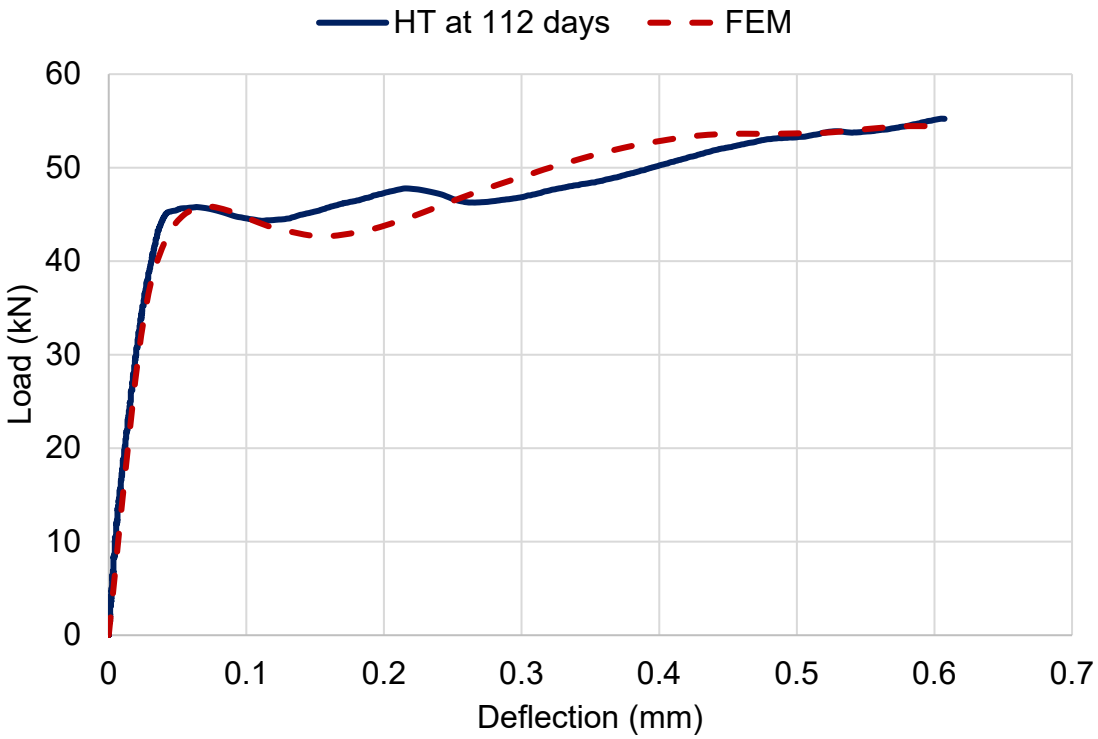

(c) Load-deflection curves of specimen aged in HT for 112 days and FEM

Figure 5-14 Load-deflection curves of experimental specimens submerged in different environmental conditions for 112 days and FEM results

5.9 Convergence Analysis and Mesh Verification

A convergence analysis is based on the principle that the approximation error in FEM results gradually decreases as the number of elements increases, and the exact solution can be obtained when the element size approaches zero (Kim, et al. 2018). The process of the convergence analysis is to change the element sizes and check how the FEM results change as a function of the number of elements or element size, as illustrated in Figure 5-15. However, this technique cannot provide an error estimation because several sets of the elements that are not converged. Thus, another technique for estimating the exact solution is needed.

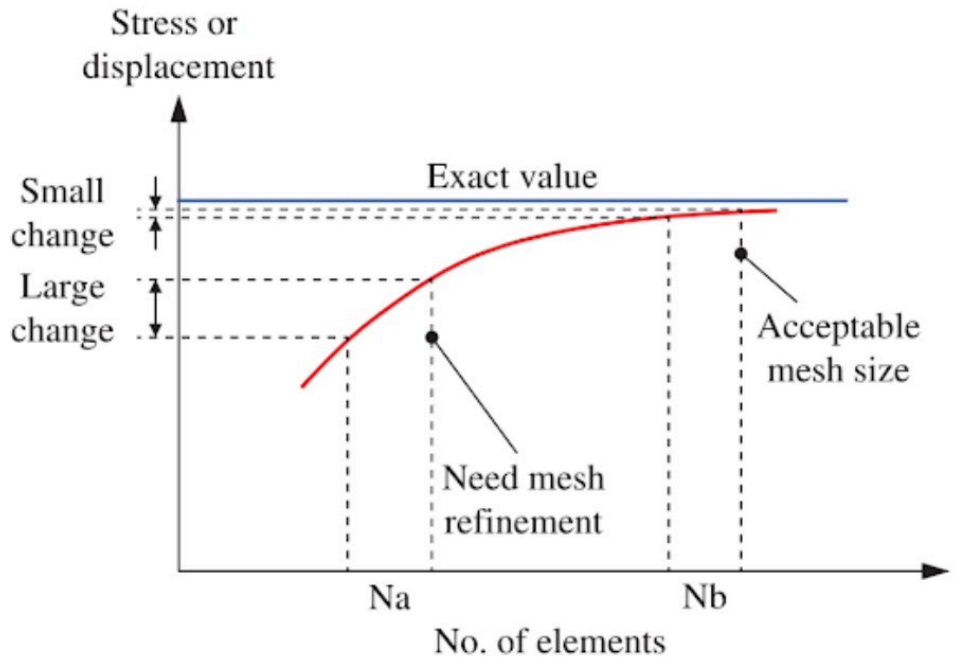

Figure 5-15 Converging to the exact solution with mesh refinement (Kim, et al. 2018)

Richardson's extrapolation is one of the methods of estimating an exact solution in finite element analysis. It is a technique that is used to accelerate the rate of convergence by estimating the exact solution, using FE solutions from three sets of un-converged meshes. The procedures of Richardson's extrapolation are as follows:

1) Choose three elements with different lengths (l).
2) Obtain the deflection result from the FE analysis of the control point (Δ) for each element length.
3) Calculate the characteristic length of the element (h) by using Eq. (5-11):

$$h = \sqrt{l^2 + l^2} \tag{5-11}$$

4) Plot the deflection (Δ) versus the characteristic length of the element (h) raised to the (q) power.

5) Iterate the (q) power until a straight line is plotted.

6) After plotting a straight line, calculate the exact solution of deflection (Δ_∞) with an infinitely fine mesh by using Eq. (5-12).

$$\Delta_\infty = \frac{\Delta_n \times (h_{n+1})^q - \Delta_{n+1} \times (h_n)^q}{(h_{n+1})^q - (h_n)^q} \tag{5-12}$$

where n is element number.

7) Calculate the error between the infinitely fine mesh deflection and other deflections by using Eq. (5-13):

$$e_n = \left|\frac{\Delta_n - \Delta_\infty}{\Delta_\infty}\right| \times 100 \tag{5-13}$$

Three element lengths (l), 30, 20, and 12 mm, were used in the Richardson's extrapolation. Figure 5-16 shows the deflection (Δ) versus the characteristic length of the element (h) raised to the (q) power. The (q) value and exact solution of deflection (Δ_∞) with an infinitely fine mesh used in the model were eight and 0.614 mm, respectively. Table 5-6 lists a comparison of Richardson's extrapolation values and the errors of each mesh size. The error between the infinitely fine mesh and the model containing the 12 mm lengths was 0.54%, which represents an accurate model.

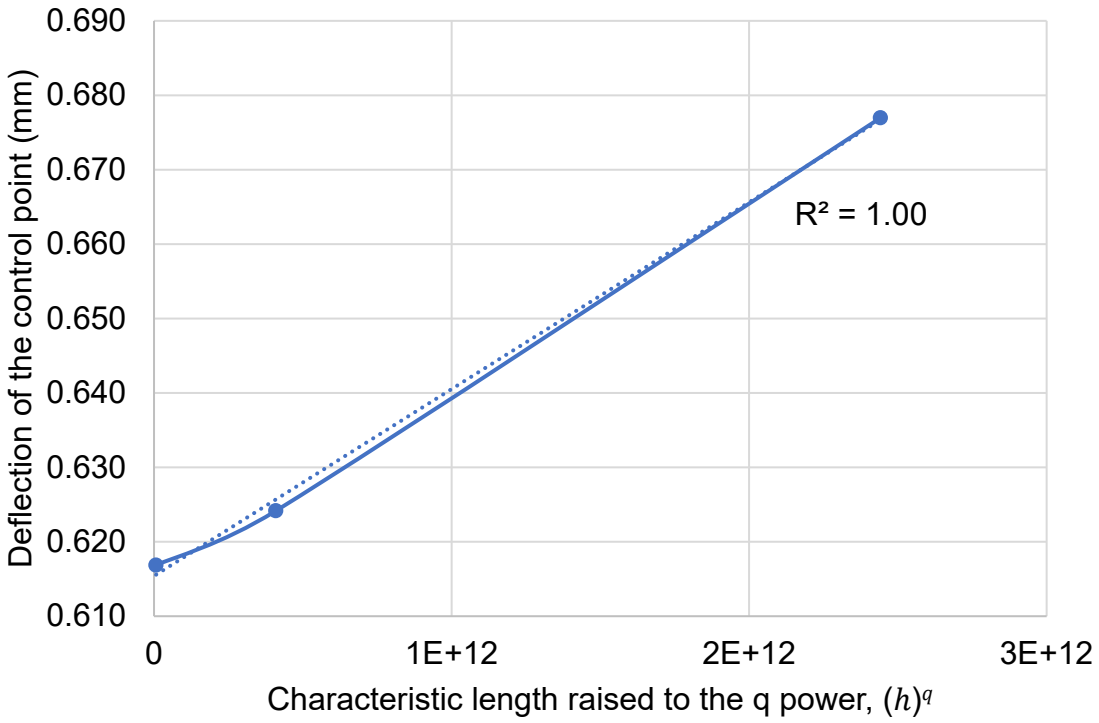

Figure 5-16 Deflection versus characteristic length raised to the (q) power

Table 5-6 Comparison of three meshes using Richardson's extrapolation

	Element (1)	Element (2)	Element (3)
Length of one element (mm)	25	20	12
Deflection of the control point (mm)	0.677	0.624	0.617
"Characteristic length" of the element	35.36	28.28	16.97
Characteristic length raised to the (q) power	2.44E+12	4.10E+11	6.88E+09
The error (%)	10.34	1.73	0.54

5.10 Evolution of Cracks

In a finite element analysis, a concrete crack is assumed to initiate at the points where the maximum principal plastic strain is positive (Lubliner et al., 1989). A comparison between the plastic strain distribution acquired from the finite element analysis and the crack pattern obtained from the experiment is presented in Figure 5-17. The crack acquired from the simulation and the experiment were comparable, which indicates that the FEM can capture the fracture mechanism in the beam.

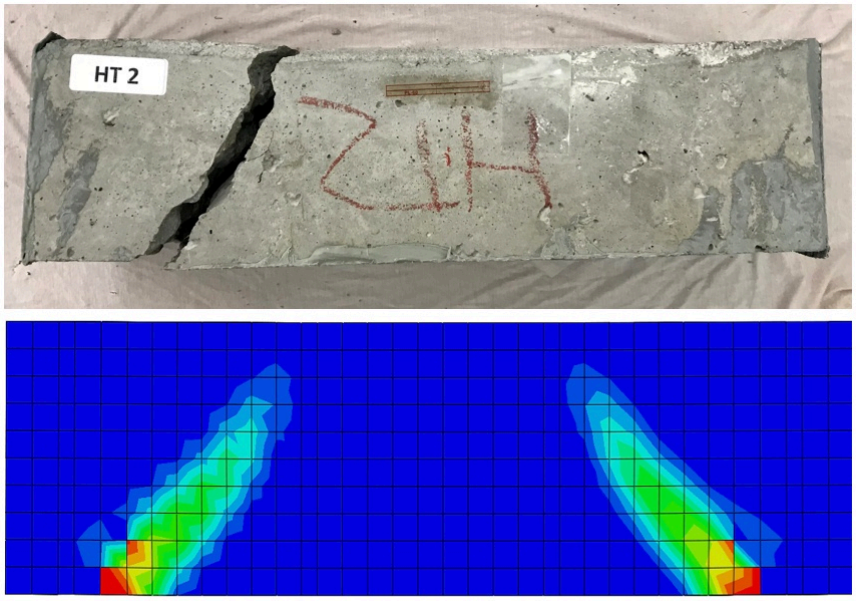

Figure 5-17 Comparison between plastic strain distribution obtained from the finite element analysis and crack pattern obtained from the experiment

5.11 Failure Mode

Interfacial debonding is a common failure mode for a concrete beam bonded to CFRP laminate. This failure mode is initiated by high interfacial shear and normal stresses

near the laminate end that exceed the strength of the concrete (Smith and Teng, 2002). As shown in Figure 5-18, the FEM can represent the interfacial debonding failure.

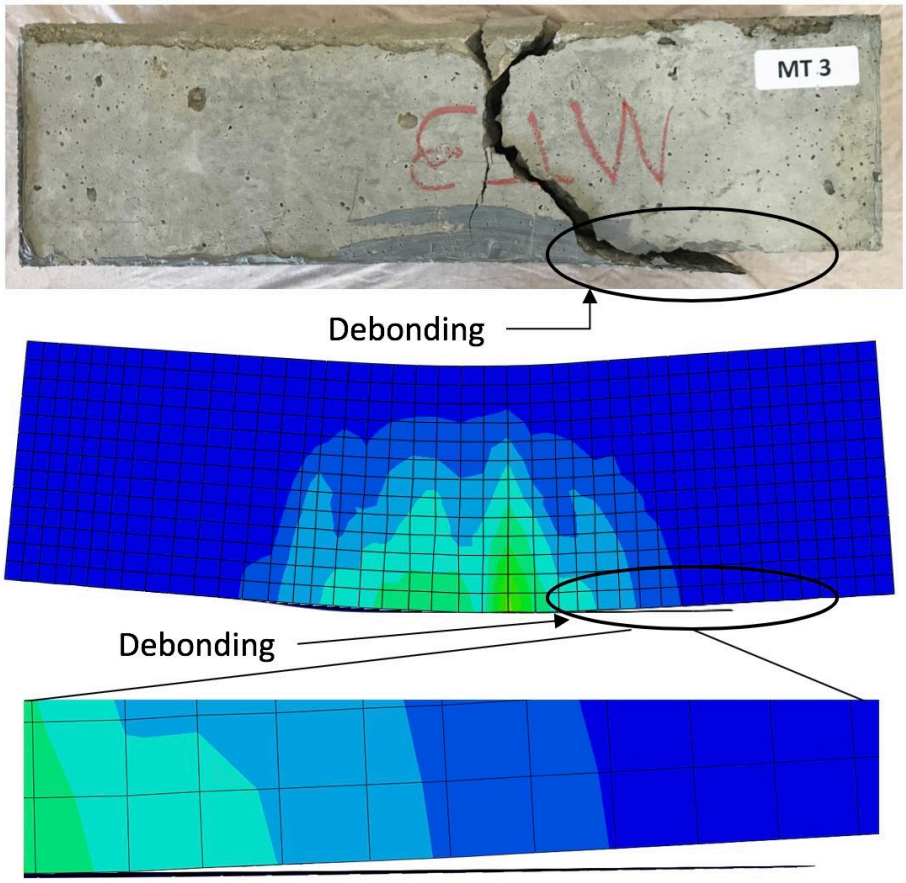

Figure 5-18 Comparison of failure mode from FEM analysis and experiment

5.12 Parametric Study

The numerical analyses were extended to investigate the effect of common physical and mechanical parameters in order to gain a better understanding of how each parameter contributed to the whole system of externally bonded CFRP-concrete beams. The findings of these analyses may provide some implications for future design guidelines. The studied parameters were concrete compressive strength, the number of laminate layers, laminate thickness, and type of FRP laminate, as listed in Table 5-7. The

effect of each parameter was demonstrated by comparing the load-deflection curve to the control model. The following subsections provide the numerical results of each parameter.

Table 5-7 Summary of variables and range of variations used in the parametric study

Study Mode	Parameters (Variables)	Range of Variation
I	Concrete compressive strength, MPa	20 25.65 28.5 (control) 40 45.6
II	Number of the laminate layers	1 (control) 2 3
III	Laminate thickness, mm	0.49 1.0 (control) 1.56 2.08
IV	Type of the FRP laminate	CFRP (control) AFRP GFRP

5.12.1 Effect of Concrete Compressive Strength

The influence of concrete compressive strength on an externally bonded CFRP-concrete beam was studied by changing the value of f_c', while maintaining all the other physical and mechanical properties. Five values of compressive strength of concrete were utilized in this study mode (I): 20, 25.65, 28.5, 40, and 45.6 MPa. Accordingly, the material properties of concrete including tensile, compressive, Youngs's modulus, and damage evolution parameters were updated to each selected range of f_c'. As shown in Figure 5-19, the load-deflection curve of each model was compared to the control model.

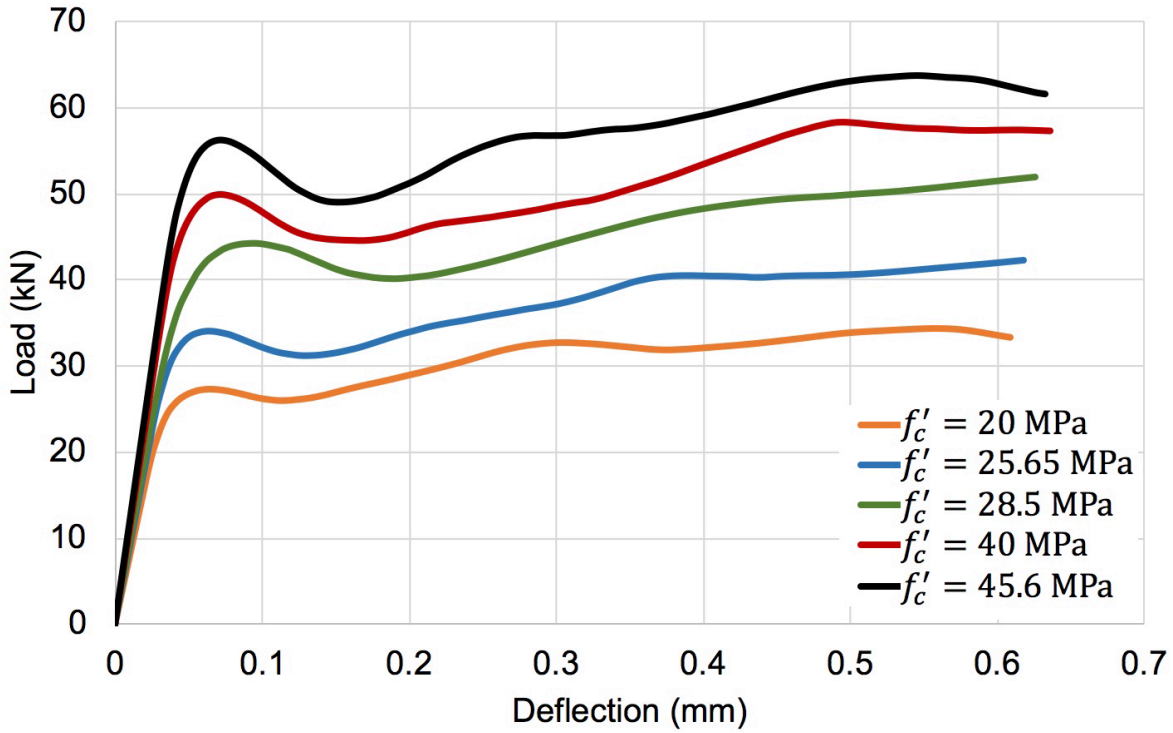

Figure 5-19 Effect of concrete compressive strength on the load-deflection curve

It can be noted from Figure 5-19 that the compressive strength of concrete had a weighty impact on the load capacity of the CFRP concrete beam. As expected, there was an improvement in the load carrying capacity with an increase in the compressive strength of concrete. The use of $f_c' = 45.6\ \text{MPa}$ revealed a growth of 19% in the ultimate load; on the other hand, the ultimate load decreased by 36% when $f_c' = 20\ \text{MPa}$. It was observed that the improvements in flexural capacities due to an increase in compressive strength of concrete are nearly constant. This can be attributed to the enhanced tensile strength of the concrete, which is respectively associated with the value of f_c'. The relationship between the flexural loading capacity and the concrete compressive strength is shown in Figure 5-20.

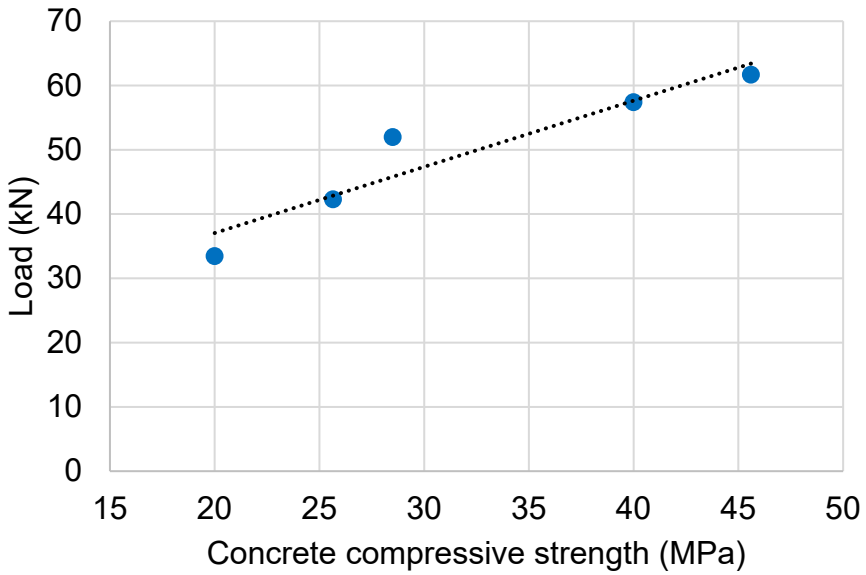

Figure 5-20 Relationship between flexural load and concrete compressive strength

5.12.2 Effect of Number of Laminate Layers

The effect of the number of CFRP laminate layers on the performance of the externally bonded CFRP concrete beam was investigated by increasing the number of ply in the laminate. One (control), two, and three ply CFRP laminate were developed in this study mode (II), as exhibited in Figure 5-21. The load-deflection curves of the two and three ply CFRP laminate models were compared to the one-ply control model, as shown in Figure 5-22. As seen, the load capacity increased with an increase in the number of CFRP laminate layers. The ultimate loads increased by 11% and 12% for the two and three ply CFRP laminates, respectively. However, it seems that the relationship between the load capacity and the number of CFRP laminate layers was not linear.

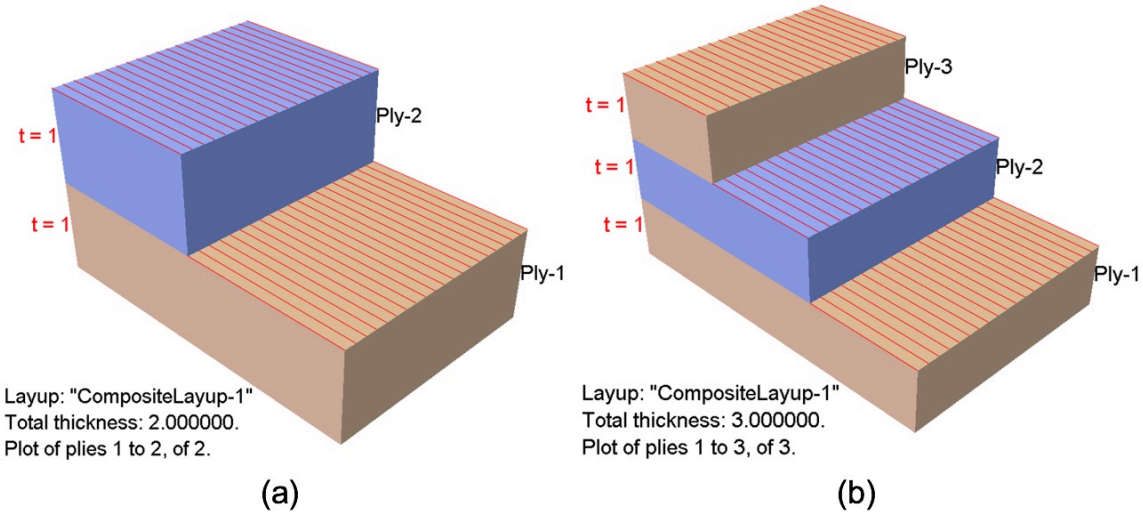

Figure 5-21 Stack view of CFRP laminate; (a) two ply, (b) three ply

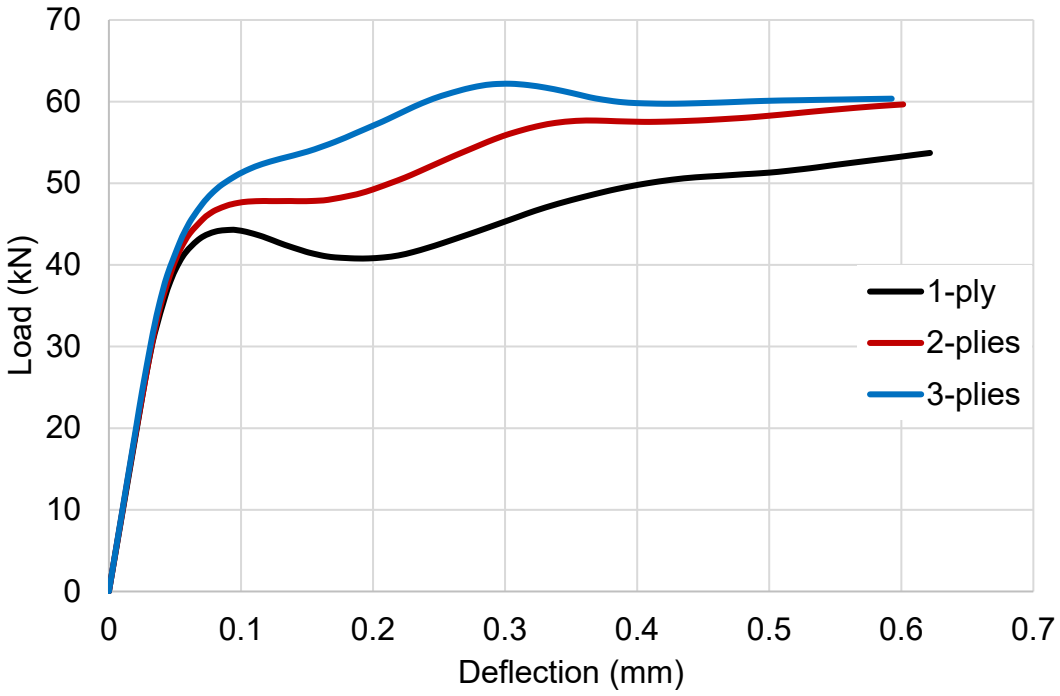

Figure 5-22 Effect of the laminate layer on the load-deflection curve

5.12.3 Effect of Laminate Thickness

The effect of laminate thickness on externally bonded CFRP concrete beams was investigated by varying the thickness of the dry carbon fiber sheet, which was based on

the manufacturer's data sheet. Hence, by maintaining the fiber concentration of 0.365, four values of laminate thickness, 0.49 mm, 1.0 mm, 1.56 mm, and 2.08 mm, were used. These values were utilized in each model, while all the other mechanical and geometric properties remained unchanged. The load-deflection curves of each laminate thickness were plotted, as displayed in Figure 5-23, where it is evident that the load capacity increased as the thickness of the CFRP laminate increased. Compared to the control model of 1.0 mm laminate thickness, the ultimate load capacities were decreased and increased by 14% for 0.49 mm and 2.08 mm laminate thickness models, respectively. Moreover, the relationship between the flexural loading capacity and the laminate thickness seems to be linear, as depicted in Figure 5-24.

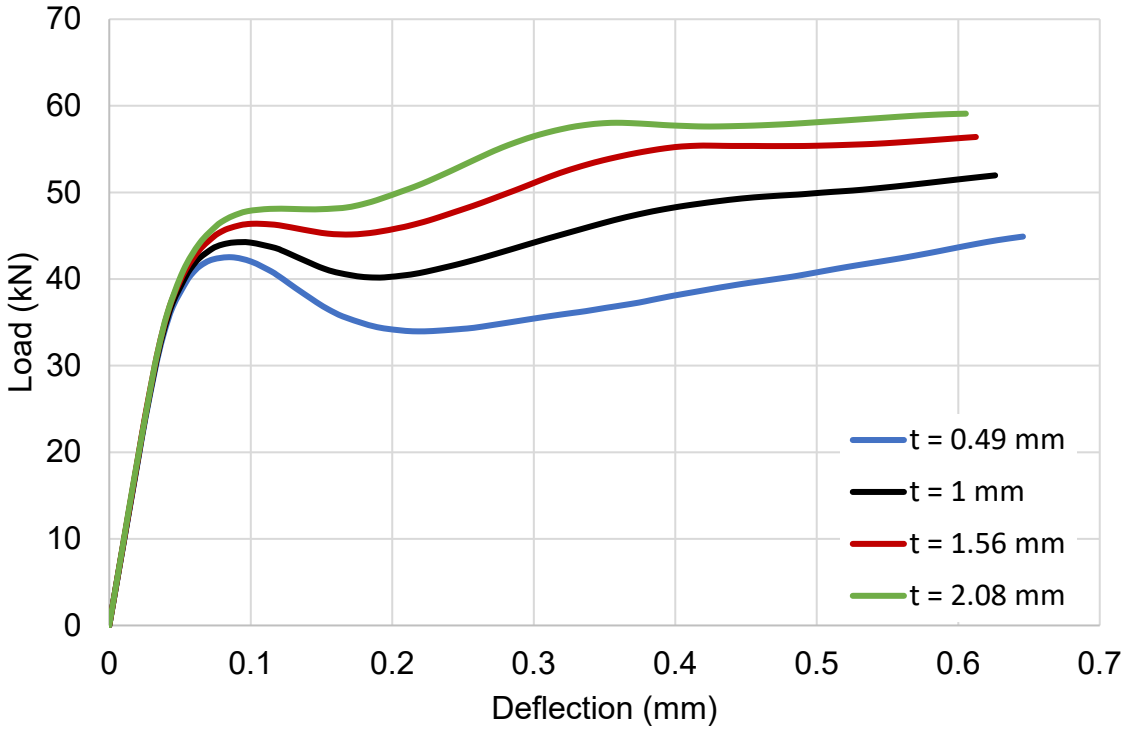

Figure 5-23 Effect of laminate thickness on the load-deflection curve

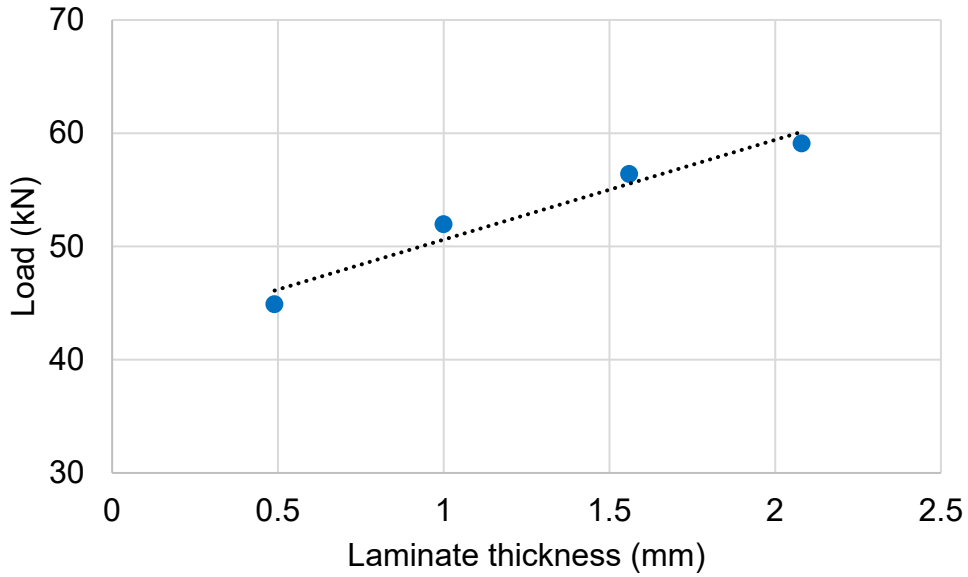

Figure 5-24 Relationship between flexural load and the laminate thickness

5.12.4 Effect of Laminate FRP Type

The study on the effect of the type of laminate FRP on the externally bonded FRP-concrete beam was evaluated by changing the base fiber of the laminate. The base fibers were carbon, aramid, and glass, where the resin matrix was assumed as epoxy for all the FRP types. The control model was the CFRP type, while AFRP and GFRP were selected as the parameters in this study mode (IV). The physical and mechanical characteristics of AFRP and GFRP were obtained from the literature. The load-deflection curves of the laminate FRP types are shown in Figure 5-25. Compared to CFRP, the ultimate loads were decreased by 21% and 33% for AFRP and GFRP, respectively. This can be attributed to the high modulus of elasticity of CFRP.

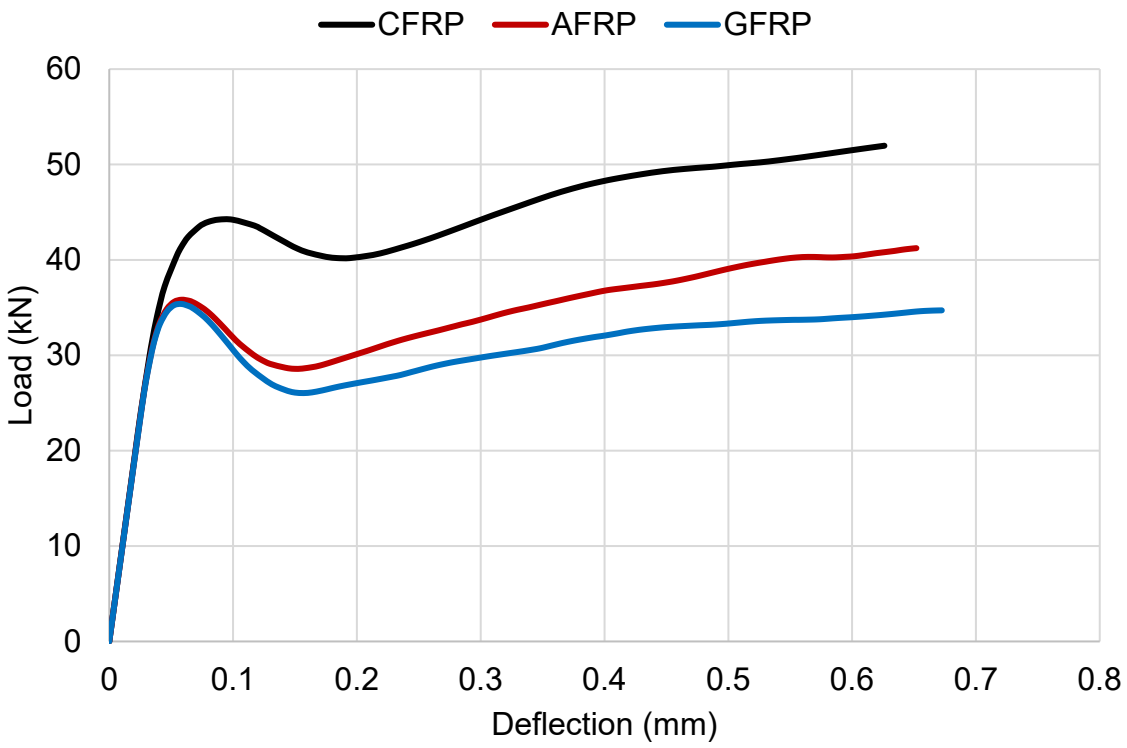

Figure 5-25 Effect of laminate FRP type on the load-deflection curve

Chapter 6. Conclusions and Recommendations

The feasibility of strengthening deteriorated concrete structures with FRP composites has been widely validated through laboratory experiments and field tests. Questions and concerns remain, however, related to the long-term performance and service life of the FRP system. This purpose of this study, conducted in four phases, was to respond to these challenges.

The first phase involved evaluating the deterioration trends of CFRP laminate under environmental conditions for periods up to 32 weeks. The tensile strength, strain performance, and tensile modulus of the laminates were obtained through a series of mechanical tests conducted after specific environmental exposure times.

In the second phase, four models were developed to predict the long-term performance of CFRP laminates. They were calibrated with real data from the field (Timilsina, et al., 2020; Timilsina, 2018), and the most applicable prediction model was used to evaluate the environmental reduction factor, C_E, from ACI 440.2R (2017). Hence, an equation to estimate the environmental reduction factor, C_E, from ACI 440.2R (2017) was proposed.

The third phase utilized direct tension pull-off and three-point flexural tests to evaluate the durability of externally bonded CFRP concrete beams under specific environmental conditions.

Numerical analyses were performed in the fourth phase to simulate the flexural test of externally bonded CFRP concrete beams using ABAQUS, a non-linear finite

element software. The numerical analyses were calibrated with the experimental results and other parameters were studied.

6.1 Summary of Findings and Conclusions

The following observations and recommendations resulted from this study:

- Immersing CFRP laminates in elevated-temperature water tanks degrades their mechanical properties. The most serious degradation occurred when the laminates were immersed in 60 °C for 224 days and the tensile strength retention was only 67%. It was concluded that the degradation rate increases with an increase in the temperature of the water.
- The strain performance of CFRP laminates reduces as the environmental exposure increases. The variations in temperature had a negligible effect on the strain behavior, and the strain degradation rates for all the environmental conditions were less severe than those observed for the tensile strength.
- Although ACI 440.2R (2017) assumes that the modulus of elasticity is not affected by environmental conditions, the values of CFRP laminates were affected, especially for the 60 °C condition, which resulted in a loss of about a quarter of their initial modulus of elasticity.
- The prediction models of the long-term behavior of CFRP laminates were proposed using the Arrhenius method. They were calibrated with real data from the field and compared with the environmental reduction factor from ACI 440.2R (2017) and other international strengthening guidelines. The results showed that ACI 440.2R (2017) overestimated the tensile strength of CFRP material, which

may result in unsafe conditions before the end of the designed service life. Hence, a function of the design life of the environmental reduction factor, C_E, from the ACI 440.2R (2017) for CFRP was proposed, and a recommendation of 0.75 was made for the environmental reduction factor.

- A total of 28 pull-off tests were performed on 14 different specimens. The most prevalent failure mode observed was bonding epoxy failure at dolly, which occurred in 43% of the samples and was followed by 39% cohesive failure in the concrete substrate. The smallest failure mode witnessed was a mixed cohesive failure in concrete and epoxy at the epoxy/concrete interface, which occurred in 18% of the samples. The possible causes of bonding epoxy failure include using an unsuitable bonding epoxy system for attaching the dolly, improper surface preparation, and inappropriate pull-off tester orientation and application.
- The pull-off stress showed an insignificant fluctuation during the exposure time. In all the environmental conditions, the stress behavior increased, decayed, and then increased again. It was concluded that the environmentally caused degradation of the FRP-adhesion-concrete interface is not affected by the exposure time.
- The results of the flexural test of the externally bonded CFRP concrete system showed that the failure strength of the specimens subjected to 23, 45, and 60 °C increased after 112 days of exposure by 20%, 49%, and 11%, respectively. The improvement in the failure strength is attributed to concrete curing over time, and a comparison of the failure modes showed that the CFRP laminates remained intact at failure.

- Flexural tests revealed that plate end interfacial debonding was the failure mode associated with specimens immersed in water with temperatures of 23 and 45 °C. It was caused by high interfacial shear and normal stresses that developed in the region and led to the formation of a crack at the laminate end. For specimens immersed in 60 °C water, shear failure was the most prevalent when the concrete substrate failed cohesively due to the degradation of the tensile strength of the concrete. To avoid shear failure, adequate shear strength should be provided to resist the applied shear forces. Additionally, FRP laminates oriented transversely to the section can be used to prevent shear failure.
- Numerical analyses were performed using ABAQUS, and the finite element models and the experimental results were in good agreement with the failure load and maximum displacement.
- Concrete compressive strength, the number of laminate layers, laminate thickness, and laminate FRP types were selected as parameters. It was observed that the improvements in flexural capacities due to an increase in compressive strength of concrete and the laminate thickness are nearly constant.

6.2 Future Research

The following are the recommendations for further research work:

- The effects of chemical and thermal environmental exposure on FRP composites need to be studied further. Such exposures include temperature variations, moisture, freeze-thaw cycles, ultraviolet radiation, and immersion in alkali and acidic solutions.

- Since the obtained long-term field data was limited to CFRP composites, the proposed function of the design life of the environmental reduction factor is only suitable for CFRP materials. More field data of GFRP and AFRP is needed for calibrating prediction models. It would be advisable to obtain FRP samples from the field every few years to evaluate the strength retention with respect to the service life.
- The performance of interfacial FRP concrete bonded systems needs to be fully understood by evaluating the adhesive bonding between the concrete and the FRP materials with experiments such as peel off, shear fracture, and pull-off tests.
- The effects of the environmental conditions studied were limited to sound concrete beams strengthened by CFRP. Further studies are needed to investigate the long-term performance of CFRP bonded to deteriorated concrete beams.
- A more detailed numerical analysis is needed to determine the specific contributions of the various parameters, including cohesive interaction behavior, the orientation of the laminate, steel reinforcement, and sustained loads.

Appendix A: Stress-strain Diagrams of Coupon Specimens at Different Environmental Conditions and Durations

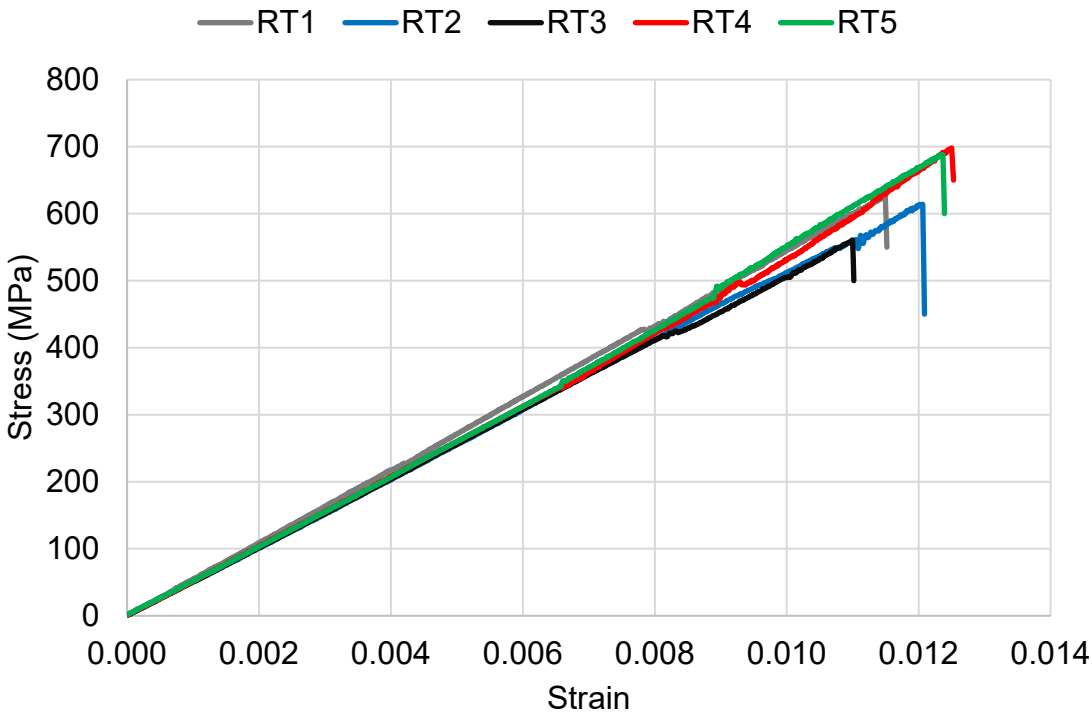

Figure A-1 Stress-strain diagram of CFRP samples immersed in RT (23 °C) for 28 days

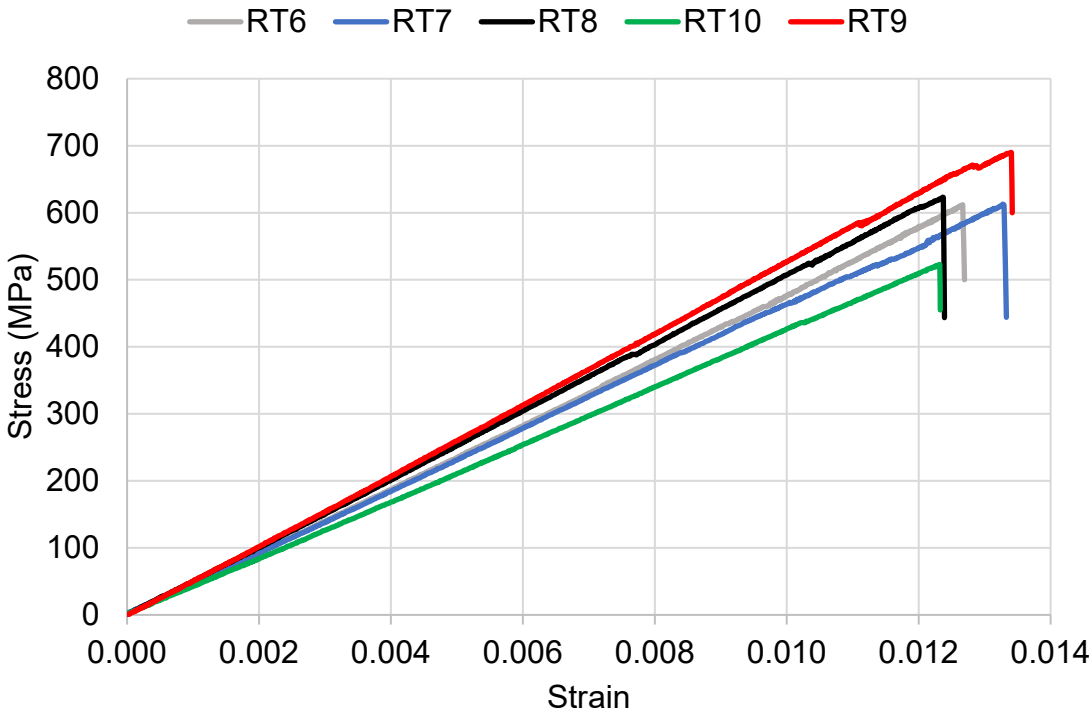

Figure A-2 Stress-strain diagram of CFRP samples immersed in RT (23 °C) for 56 days

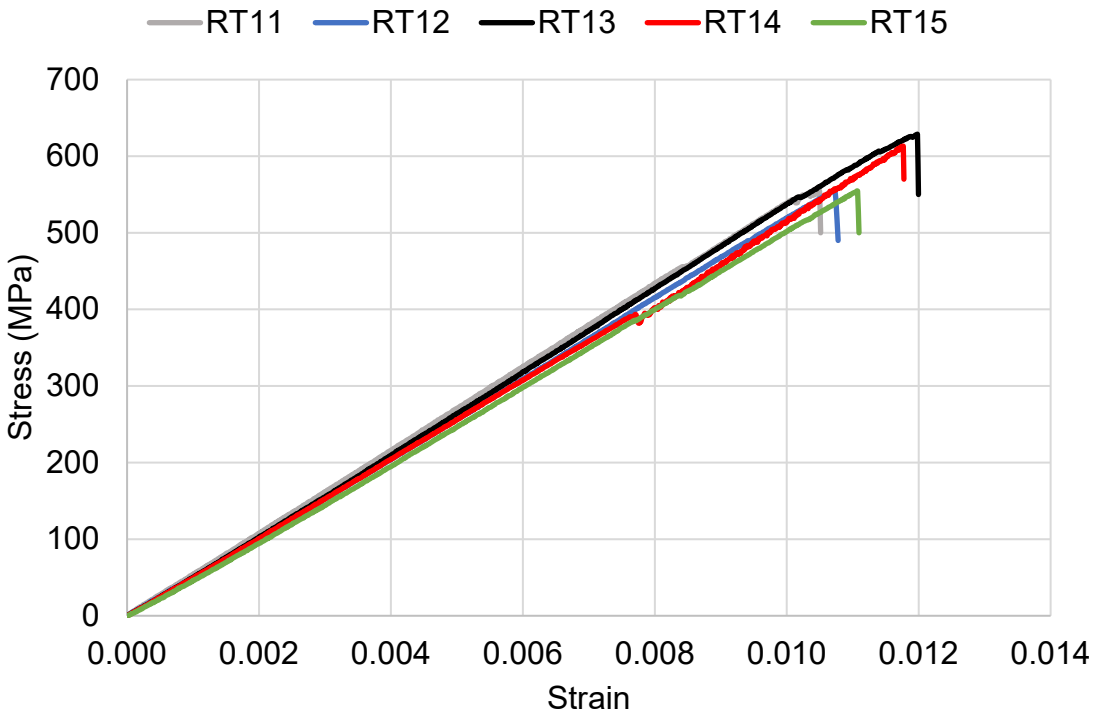

Figure A-3 Stress-strain diagram of CFRP samples immersed in RT (23 °C) for 84 days

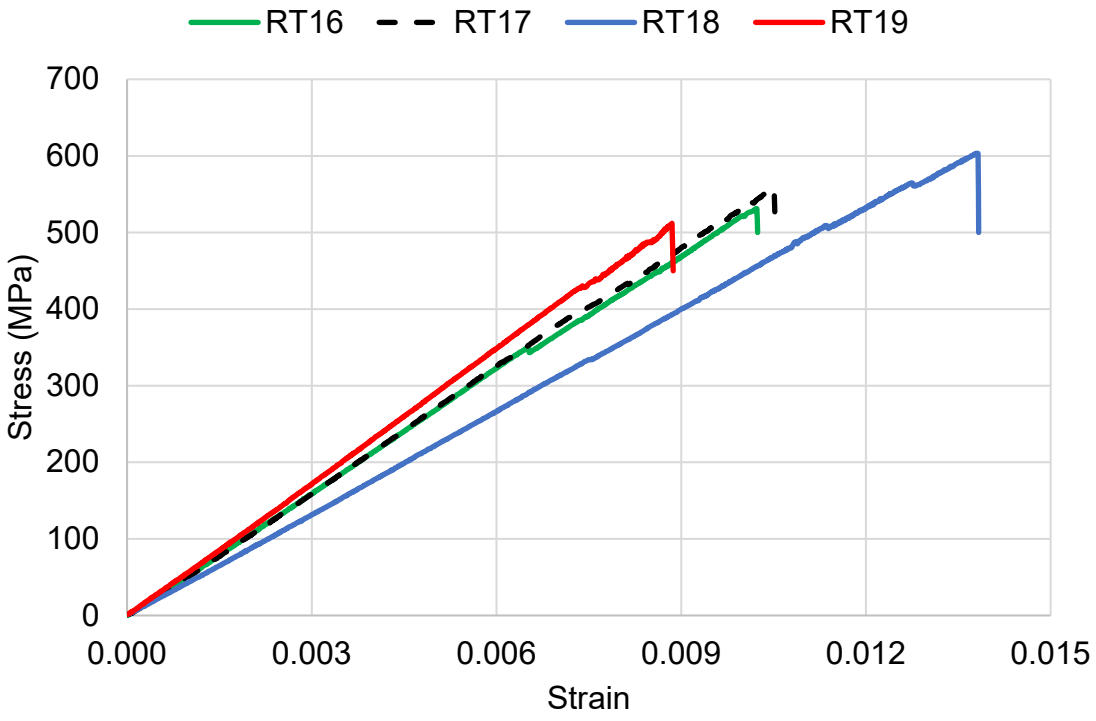

Figure A-4 Stress-strain diagram of CFRP samples immersed in RT for 112 days

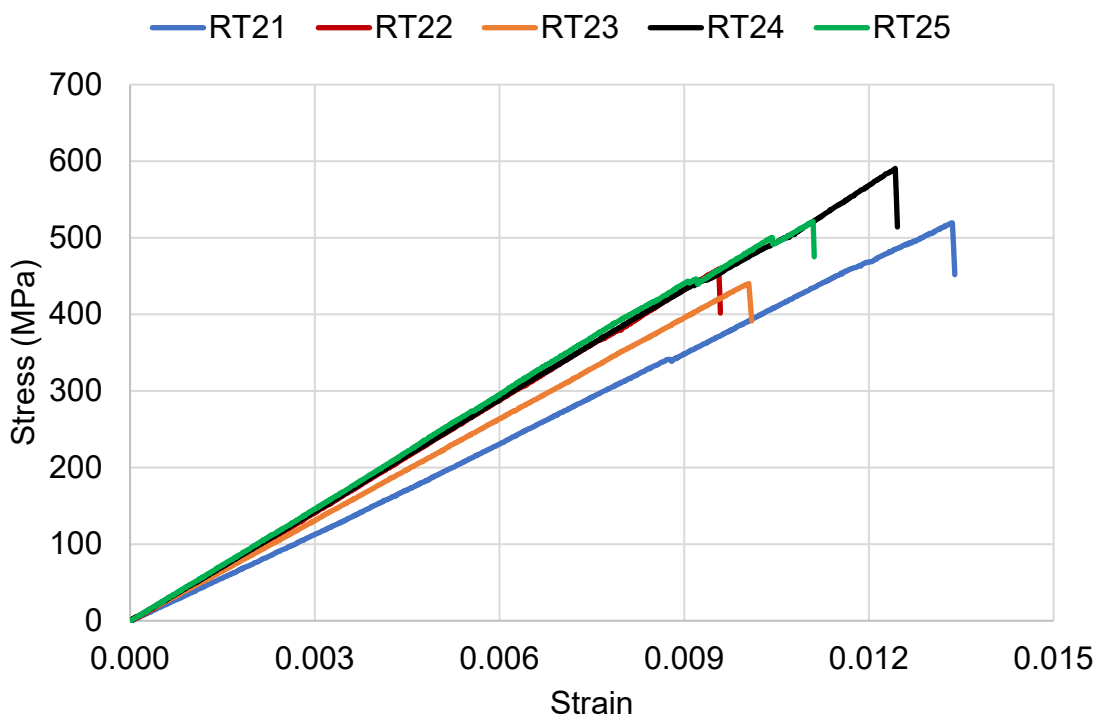

Figure A-5 Stress-strain diagram of CFRP samples immersed in RT for 224 days

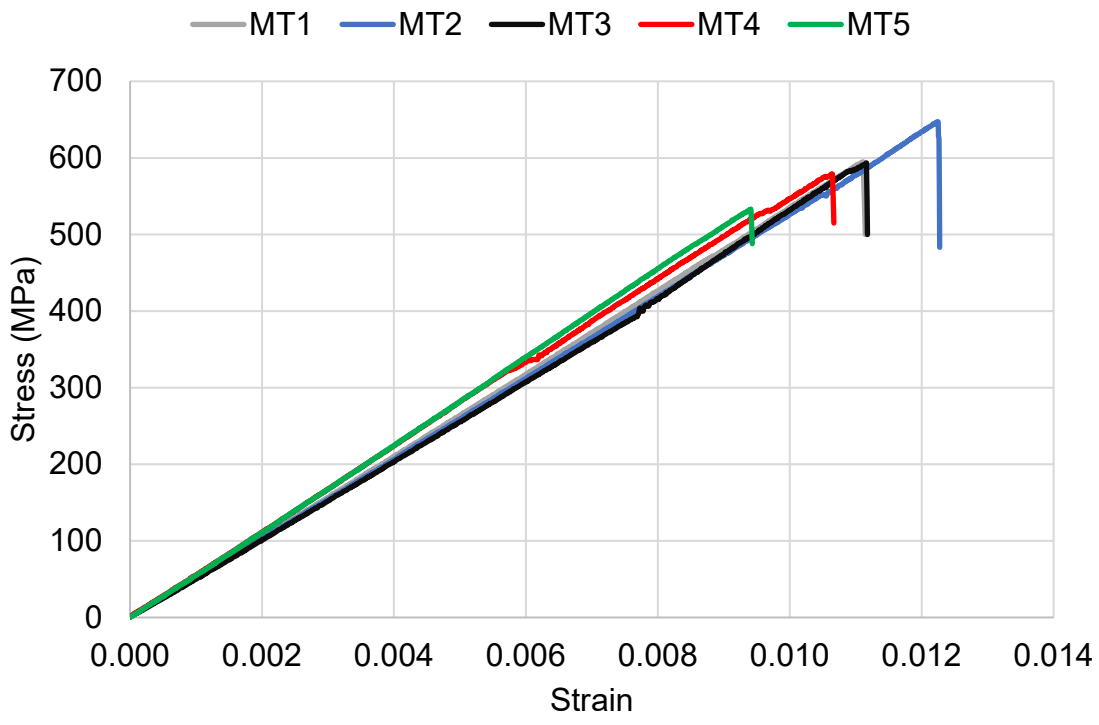

Figure A-6 Stress-strain diagram of CFRP samples immersed in MT (45 °C) for 28 days

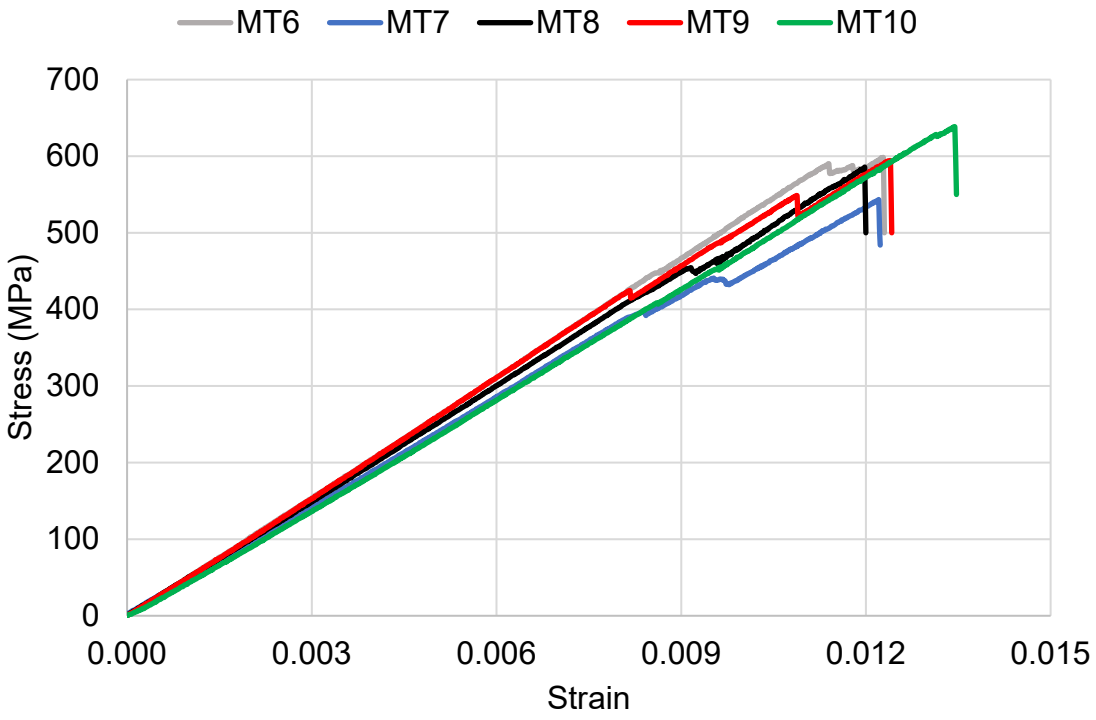

Figure A-7 Stress-strain diagram of CFRP samples immersed in MT (45 °C) for 56 days

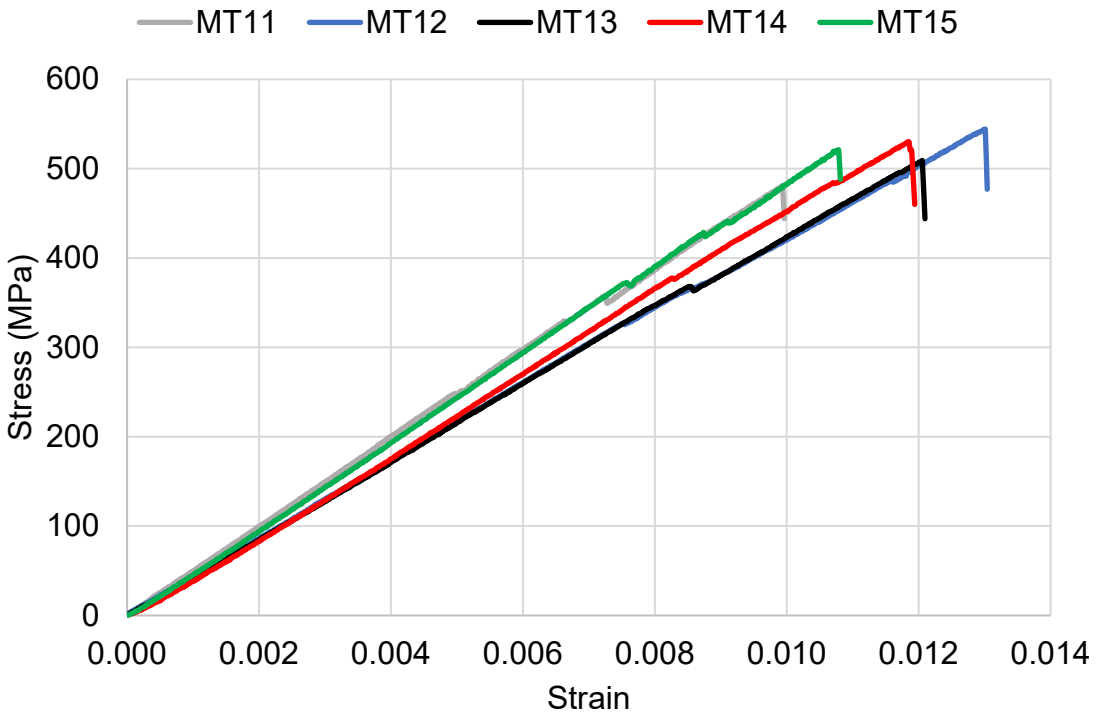

Figure A-8 Stress-strain diagram of CFRP samples immersed in MT (45 °C) for 84 days

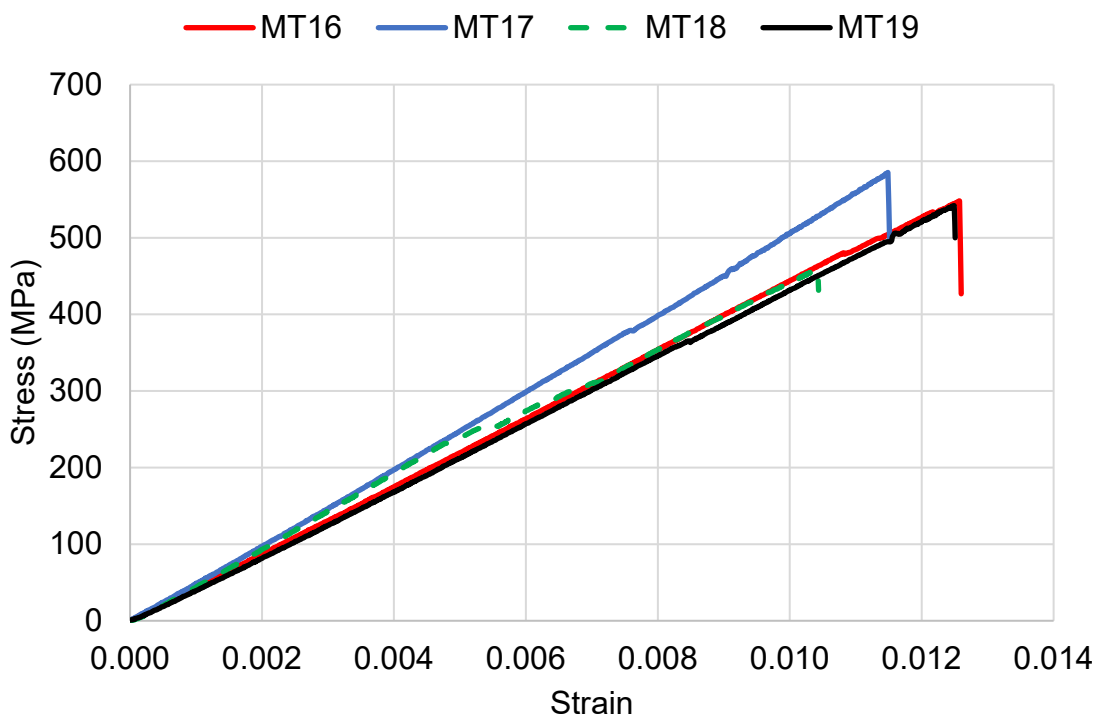

Figure A-9 Stress-strain diagram of CFRP samples immersed in MT for 112 days

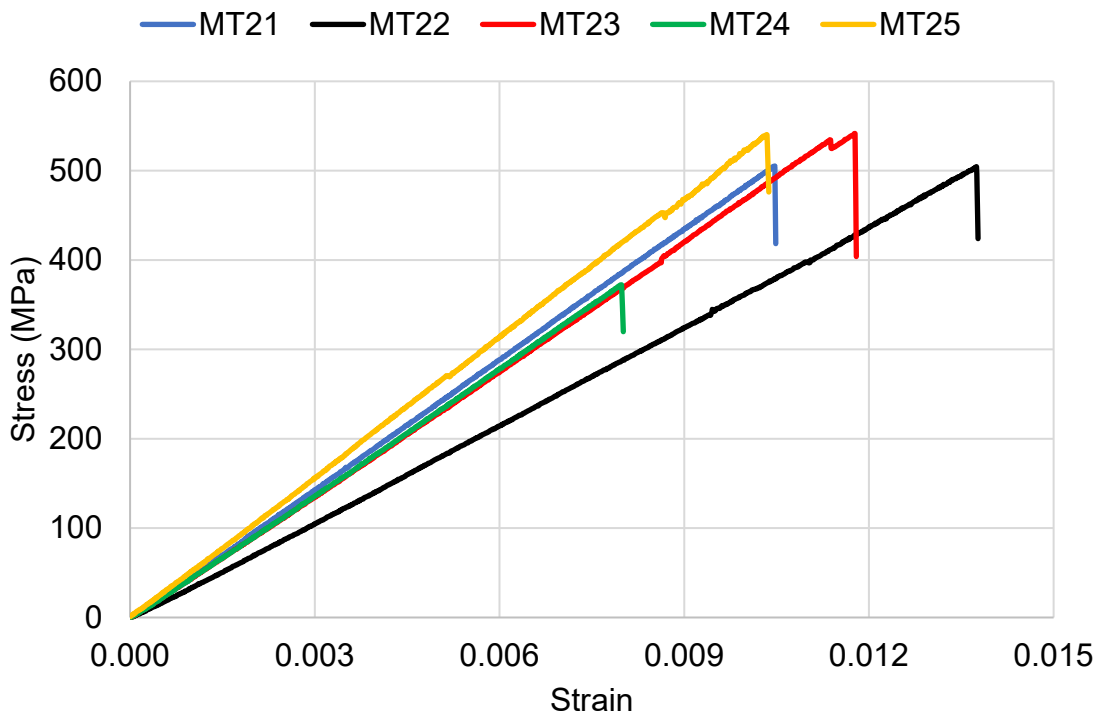

Figure A-10 Stress-strain diagram of CFRP samples immersed in MT for 224 days

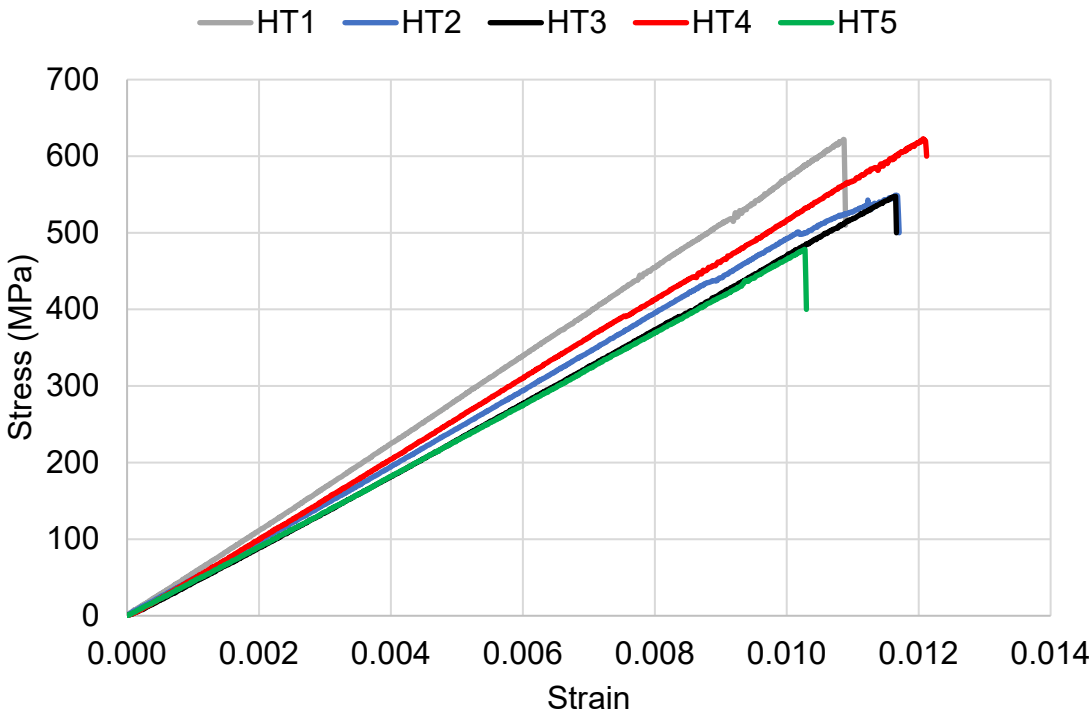

Figure A11 Stress-strain diagram of CFRP samples immersed in HT (65 °C) for 28 days

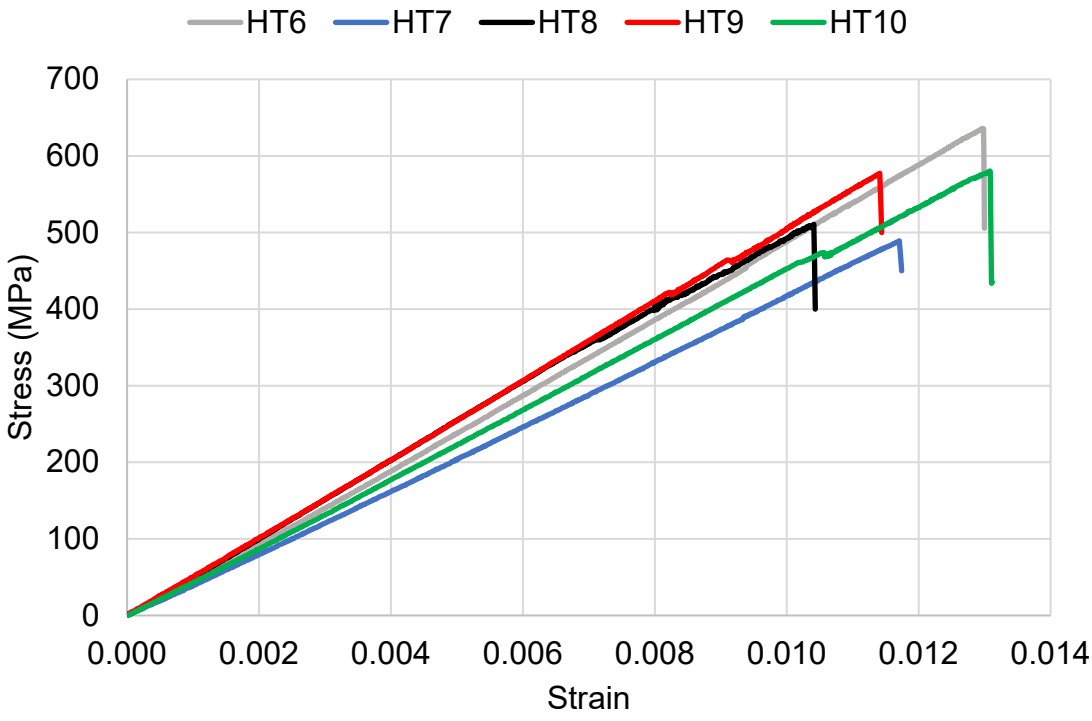

Figure A12 Stress-strain diagram of CFRP samples immersed in HT (65 °C) for 56 days

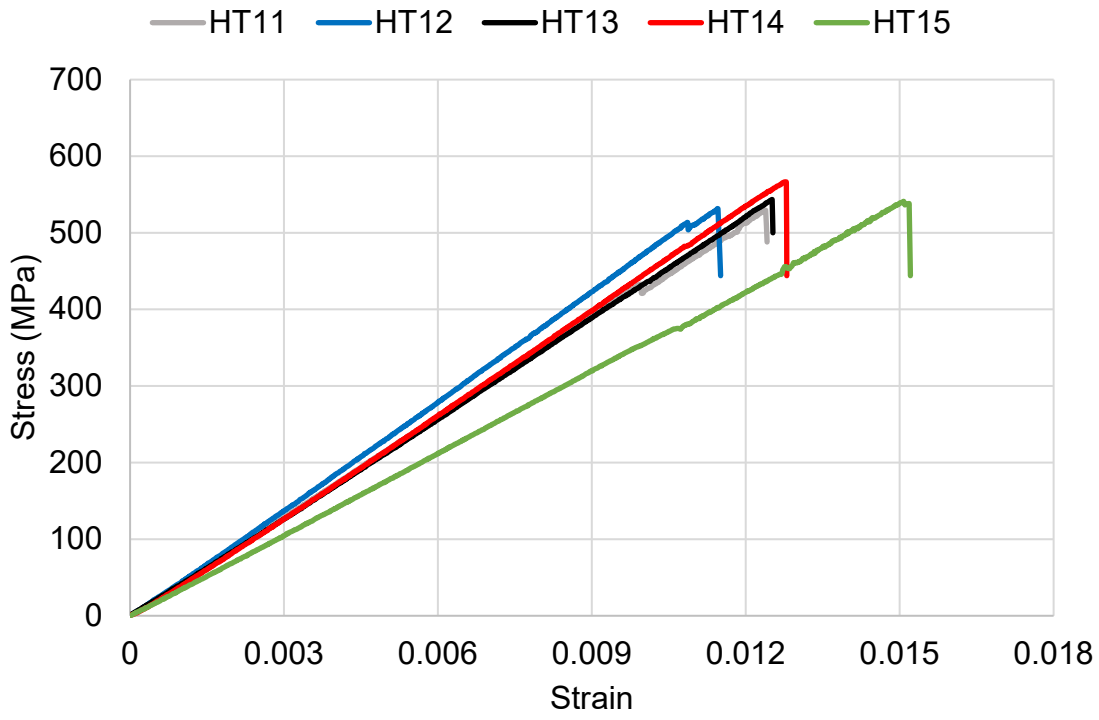

Figure A13 Stress-strain diagram of CFRP samples immersed in HT (65 °C) for 84 days

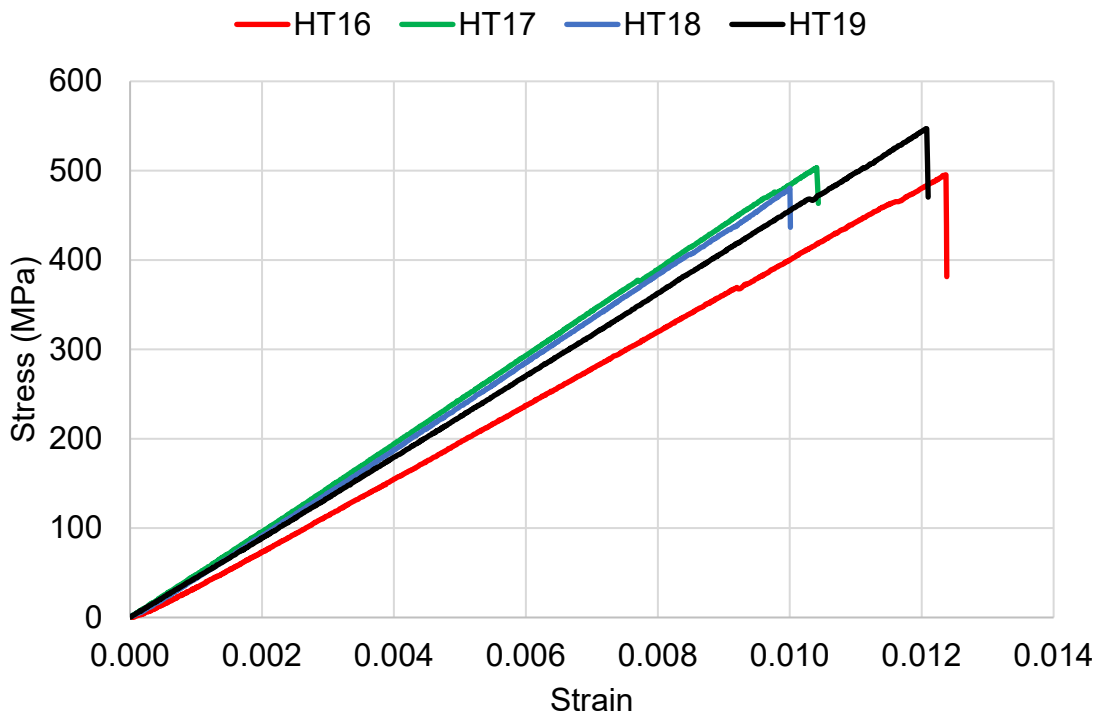

Figure A-14 Stress-strain diagram of CFRP samples immersed in HT for 112 days

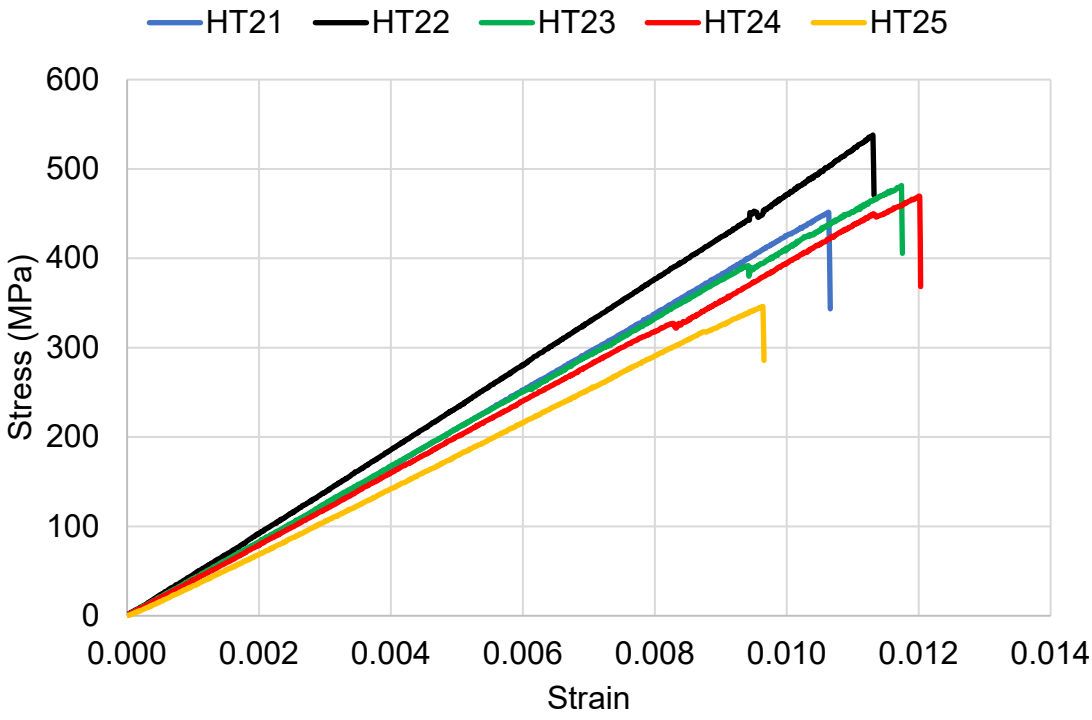

Figure A-15 Stress-strain diagram of CFRP samples immersed in HT for 224 days

Appendix B: Material Properties

B.1 Concrete Properties

Mix Design Parameters
Minimum Compressive Strength: 3 ksi @ 28 Days
Sack Content: 5.50
Air Content: 1.5% +/- 1%
Fly Ash Content: 20%
Slump Range (inches): 5 +/- 1"
Water/cement (w/c) Ratio: 0.244

One Cubic Yard Mix Proportions	
Materials	Weights per Cubic Yard, SSD
Cement	414 lb.
Fly Ash	103 lb.
Coarse Aggregate (1” Limestone)	1050 lb.
Fine Aggregate (sand1)	336 lb.
Fine Aggregate (man-sand)	1001 lb.
Admixture 1 (Sika-plastiment)	10.3 oz.
Admixture 2 (Sika 686)	20.7 oz.
Sika Air	2.1 oz.
Water	29.5 gallon

B.2 Carbon Fiber Fabric Sheet (SikaWrap® Hex-117C)

Product Information
Fiber Type: 0 ° (unidirectional)
Dry Fiber Density: 0.065 ib./in^3 (1.8 g/cc)
Area Density: 9.0 osy (300 gsm)
Dry Fiber Tensile Strength: 550 ksi (3,793 MPa)
Dry Fiber Modulus of Elasticity in Tension: 34,000 ksi (234 GPa)
Dry Fiber Elongation at Break: 1.5%

Cured Laminate Technical Information (Design Values)
Nominal Ply Thickness: 0.02 in. (0.51 mm)
Tensile Strength: 105 ksi (724 MPa)
Tensile Modulus: 8,200 ksi (56.5 GPa)
Tensile Elongation: 1.0%

B.3 Two-Component Epoxy Impregnation Resin (Sikadur®-330)

Technical Information
Tensile Strength (ASTM-D638): 7.9 ksi (33.8 MPa)
Flexural Strength (ASTM D-790): 8.8 ksi (60.6 MPa)
Flexural Modulus (ASTM D-790): 506 ksi (3,489 MPa)
Elongation at Break (ASTM D-638): 1.2%

Appendix C: Specimens After Failure

Figure C-1 Failure modes from flexural tests of specimens immersed in room temperature (23 °C) water for different durations

Figure C-2 Failure modes from flexural tests of specimens immersed in moderate temperature (45 °C) water for different durations

Figure C-3 Failure modes from flexural tests of specimens immersed in moderate temperature (60 °C) water for different durations

Appendix D: Theoretical Calculation of Flexural Capacity

Concrete Beam Strengthened by CFRP Laminate

A theoretical approach to evaluate the contribution of external CFRP laminates to a simply supported concrete beam was obtained in accordance with ACI 440.2R (2017). The beam was plain normal concrete (i.e. no steel reinforcement).

D.1 Concrete Design Properties

The specified compressive strength, f_c', of concrete using standard at the age of 28 days was 28.5 MPa (4.14 ksi). Modulus of elasticity, E_c, for normal-weight concrete is defined as the slope of the compressive stress, f_c', from zero to 0.45 f_c' and shall be calculated as:

$$E_c = 57{,}000\sqrt{f_c'} \tag{D-1}$$

$$E_c = 57{,}000\sqrt{4140} = 3{,}667 \text{ ksi} = 25.29 \text{ GPa} \tag{D-2}$$

The tensile strength of concrete in flexure can be defined as the modulus of rupture, f_r , for concrete shall be calculated as:

$$f_r = 7.5\lambda\sqrt{f_c'} \quad \text{(in psi)} \tag{D-3}$$

where: λ = modification factor and equals to 1 for normal-weight concrete.

$$f_r = 7.5 \times 1 \times \sqrt{4140} = 482 \text{ psi} = 3.3 \text{ MPa} \tag{D-4}$$

D.2 Beam Geometry

Table D1 lists the dimensions of the beam. Figure D1 shows a schematic of the section view of the beam with CFRP external reinforcement.

Table D1 Beam dimensions

Item	Value
Beam length, l	18.0 in. (457.2 mm)
Beam width, b	6.0 in. (152.4 mm)
Beam depth, h	6.0 in. (152.4 mm)
Depth to CFRP, d_f	6.01 in. (152.65 mm)
CFRP width, b_f	6.0 in. (152.4 mm)

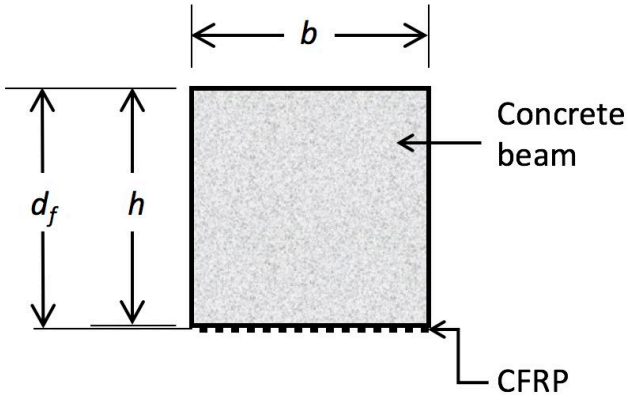

Figure D1 Schematic of the section view of the beam with CFRP external reinforcement

D.3 Manufacture's Reported CFRP Properties

Table D2 Manufacture's reported CFRP properties

Item	Design value
Nominal ply thickness, t_f	0.02 in (0.51 mm)
Ultimate tensile strength, f_{fu}^*	105 ksi (724 MPa)
Modulus of elasticity of CFRP laminate, E_f	8,200 ksi (56.5 GPa)
Rupture strain, ε_{fu}^*	1.0 %

D.4 Procedures of Flexural Calculation

The beam was used as a control sample, so it considered in an interior space. Therefore, per Table 9.4 in ACI 440.2R (2017), an environmental reduction factor of 0.95 was utilized.

$$f_{fu} = C_E f_{fu}^* \tag{D-5}$$

$$f_{fu} = 0.95 \times 105 = 99.75\ ksi \tag{D-6}$$

$$\varepsilon_{fu} = C_E \varepsilon_{fu}^* \tag{D-7}$$

$$\varepsilon_{fu} = 0.95 \times 0.01 = 0.0095 \tag{D-8}$$

Calculate the CFRP area:

$$A_f = n t_f b_f \tag{D-9}$$

where n is number CFRP layer, t_f is CFRP laminate thinness, and b_f is CFRP width.

$$A_f = 1 \times 0.02 \times 6 = 0.12\ in^2 \tag{D-10}$$

The ratio of CFRP reinforcing to concrete section is as follows:

$$\rho_f = \frac{A_f}{b \times h} \tag{D-11}$$

$$\rho_f = \frac{0.12}{6 \times 6} = 0.00333 \tag{D-12}$$

Determine the design strain of the CFRP system:

The design strain of CFRP accounting for debonding failure mode, ε_{fd}, was calculated as:

$$\varepsilon_{fd} = 0.083\sqrt{\frac{f_c'}{1E_f t_{f1}}} \leq 0.9\varepsilon_{fu} \quad \text{(D-13)}$$

$$\varepsilon_{fd} = 0.083\sqrt{\frac{4140}{1 \times 8{,}200{,}000 \times 0.02}} \leq 0.9 \times 0.0095 \quad \text{(D-14)}$$

$$\varepsilon_{fd} = 0.0132 > 0.00855 \quad \text{(D-15)}$$

$$\varepsilon_{fd} = 0.00855 \quad \text{(D-16)}$$

Because the rupture strain is smaller than the design strain, CFRP rupture controls the design of the CFRP system.

Calculate the depth to the neutral axis:

The neutral axis is the location where the bending stress is zero. The location of the neutral axis depends on the relative stiffness and size of each of the material sections (i.e. concrete and CFRP laminate). Based on the theory of mechanics of material, the depth to the neutral axis, c, was calculated as 3.022 in. (76.75 mm)

Calculate the stress level in the CFRP:

$$f_{fe} = E_f \varepsilon_{fe} \quad \text{(D-17)}$$

$$f_{fe} = 8{,}200 \times 0.00855 = 70.1 \text{ ksi} = 483.4 \text{ MPa} \quad \text{(D-18)}$$

Calculate flexural strength for CFRP system:

$$M_n = \Psi_f A_f f_{fe} \left(d_f - \frac{\beta_1 c}{2}\right) \quad \text{(D-19)}$$

where: M_n = nominal flexural capacity,

Ψ_f = CFRP strength reduction factor (0.85 for flexure),

c = distance from extreme compression fiber to the neutral axis, and

β_1 = ratio of depth of equivalent rectangular stress block to depth of the neutral axis.

$$M_n = 0.85 \times 0.12 \times 70.1 \left(6.01 - \frac{0.85 \times 3.022}{2}\right) = 33.79 \text{ kip-in} \quad \text{(D-20)}$$

D.5 Structural Analysis of Concrete Member

The flexural strength of concrete beam was evaluated using a three-point loading test in accordance with ASTM C78/C78M (2010). Figure D2 show a schematic of the bending moment diagram for the beam.

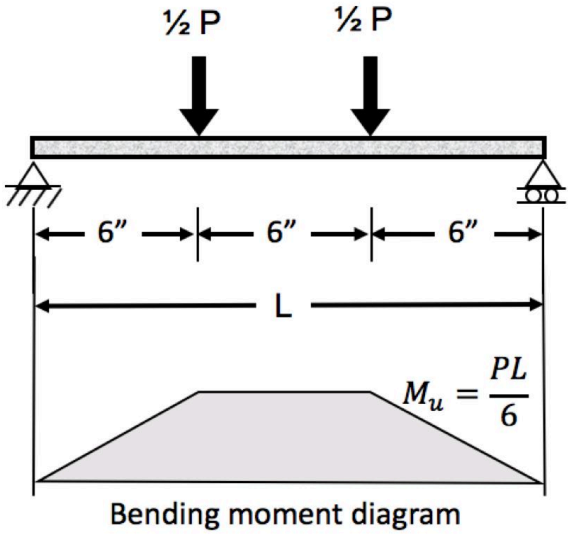

Figure D2 Bending moment diagram for the beam with three-point loading

Form the structural analysis of the beam, the ultimate moment, M_u, can be calculated as:

$$M_u = \frac{PL}{6} = \frac{P \times 18}{6} = 3P \tag{D-21}$$

Bending stress in the beam:

The bending stress of the beam can be calculated at any location along the beam and beam's cross section by using bending moment. The bending moment differs over the height of the cross section according to equation below:

$$\sigma = \frac{My}{I} \tag{D-22}$$

where: M = bending moment at any location of the beam's length,

y = the distance from the beam's neutral axis to the point of interest along the height of the cross section, and

I = the moment of inertia of the beam's cross section.

The maximum bending stress is given by

$$\sigma_{max} = \frac{M_u \, y_{max}}{I} \tag{D-23}$$

The moment of inertia of the beam's cross section, I, can be calculated as:

$$I = \frac{bh^3}{12} = \frac{6 \times 6^3}{12} = 108 \; in^4 \tag{D-24}$$

The distance from the beam's neutral axis to the point of interest along the height of the cross section can be calculated as:

$$y_{max} = \frac{h}{2} = \frac{6}{2} = 3\ in \tag{D-25}$$

By rearrange Eq. (D-23):

$$\sigma_{max} = \frac{3P\ \times 3}{108} = \frac{P}{12} \tag{D-26}$$

Ultimate load of the plain concrete beam (without CFRP reinforcement):

Since σ_{max} was calculated early, the ultimate load, P_u, can be calculated as:

$$482\ psi = \frac{P}{12} \tag{D-27}$$

$$P_u = 12 \times 482 = 5784\ \text{psi} = 5.78\ \text{kips} \tag{D-28}$$

Ultimate load of the concrete beam strengthened by CFRP laminate:

$$M_n = M_u \tag{D-29}$$

$$M_n = \ 33.79\ = 3P_u \tag{D-30}$$

$$P_u = \ \frac{33.79}{3} = 11.26\ \text{kips} \tag{D-31}$$

It can be noted that the flexural strength of the concrete beam strengthened by CFRP laminate is higher than the flexural strength of the plain concrete beam by 95%.

References

AASHTO, 2017. AASHTO LRFD Bridge Design Specifications, 8th ed. Washington, DC.

Abanilla, M.A., Li, Y., Karbhari, V.M., 2005. Durability characterization of wet layup graphite/epoxy composites used in external strengthening. Compos. Part B Eng. 37, 200–212. https://doi.org/10.1016/j.compositesb.2005.05.016

ACI 318R, 2014. Building Code Requirements for Structural Concrete, American Concrete Institute, ACI Comittee 318.

ACI 440.2R-17, 2017. Guide for the design and construction of externally bonded FRP systems for strengthening existing structures, ACI committee 440.

Al-Rousan, R.Z., Alhassan, M.A., AlShuqari, E.A., 2018. Behavior of plain concrete beams with DSSF strengthened in flexure with anchored CFRP sheets—Effects of DSSF content on the bonding length of CFRP sheets. Case Stud. Constr. Mater. 9, e00195. https://doi.org/10.1016/j.cscm.2018.e00195

Allen, D.G., Atadero, R.A., 2012. Evaluating the long-term durability of externally bonded frp via field assessments. J. Compos. Constr. 16, 737–746. https://doi.org/10.1061/(ASCE)CC.1943-5614.0000305

ASTM:D7522, 2012. Standard Test Method for Pull-Off Strength for FRP Bonded to Concrete Substrate 1. Annu. B. ASTM Stand. i, 1–6. https://doi.org/10.1520/D7522

ASTM, 2018. Standard Test Method for Flexural Strength of Concrete (Using Simple Beam with Third-Point Loading), ASTM C78. ed, ASTM International. West Conshohocken, PA. https://doi.org/10.1520/C0078_C0078M-18

ASTM, 2017. D3039 Standard test method for tensile properties of polymer matrix composite materials. Annu. B. ASTM Stand. 1–13. https://doi.org/10.1520/D3039

ASTM, 2016. Standard Test Method for Compressive Strength of Cylindrical Concrete Specimens, ASTM C39. ed. ASTM International, West Conshohocken, PA. https://doi.org/10.1520/C0039_C0039M-16

ASTM C143/C143M, 2015. Standard Test Method for Slump of Hydraulic-Cement Concrete. Astm C143 1–4. https://doi.org/10.1520/C0143

Bahn, B.Y., Harichandran, R.S., 2008. Flexural behavior of reinforced concrete beams strengthened with CFRP sheets and epoxy mortar. J. Compos. Constr. 12, 387–395. https://doi.org/10.1061/(ASCE)1090-0268(2008)12:4(387)

Bank, L.C., Gentry, T.R., Thompson, B.P., Russell, J.S., 2003. A model specification for FRP composites for civil engineering structures. Constr. Build. Mater. 17, 405–437. https://doi.org/10.1016/S0950-0618(03)00041-2

Böer, P., Holliday, L., Kang, T.H.K., 2013. Independent environmental effects on durability of fiber-reinforced polymer wraps in civil applications: A review. Constr. Build. Mater. 48, 360–370. https://doi.org/10.1016/j.conbuildmat.2013.06.077

Borrie, D., Liu, H.B., Zhao, X.L., Singh Raman, R.K., Bai, Y., 2015. Bond durability of fatigued CFRP-steel double-lap joints pre-exposed to marine environment. Compos. Struct. 131, 799–809. https://doi.org/10.1016/j.compstruct.2015.06.021

Breña, S.F., Bramblett, R.M., Benouaich, M.A., Wood, S.L., Kreger, M.E., 2001. Use of Carbon Fiber Reinforced Polymer Composites to Increase 13. Type of Report and Period Covered Unclassified Unclassified. Univ. Texas. Austin, USA Cent. Transp.

Res. 7.

Cao, S., Wu, Z., Wang, X., 2009. Tensile properties of CFRP and hybrid FRP composites at elevated temperatures. J. Compos. Mater. 43, 315–330. https://doi.org/10.1177/0021998308099224

Chajes, M.J., Thomson, T.A., Januszka, T.F., Finch, W.W., 1994. Flexural strengthening of concrete beams using externally bonded composite materials. Constr. Build. Mater. 8, 191–201. https://doi.org/10.1016/S0950-0618(09)90034-4

Chen, Y., Davalos, J.F., Ray, I., 2006. Durability Prediction for GFRP Reinforcing Bars Using Short-Term Data of Accelerated Aging Tests. J. Compos. Constr. 10, 279–286. https://doi.org/10.1061/(asce)1090-0268(2006)10:4(279)

Choi, S., Gartner, A. L., Etten, N. V., Hamilton, H. R., & Douglas, E.P., 2011. Durability of Concrete Beams Externally Reinforced with CFRP Composites Exposed to Various Environments. Am. Soc. Civ. Eng. 16, 10–20. https://doi.org/10.1061/(ASCE)CC.1943-5614

Cohen, M., 2018. Numerical analysis of debonding mechanisms of externally bonded FRP reinforcement in RC beams.

Cromwell, J.R., Harries, K.A., Shahrooz, B.M., 2011. Environmental durability of externally bonded FRP materials intended for repair of concrete structures. Constr. Build. Mater. 25, 2528–2539. https://doi.org/10.1016/j.conbuildmat.2010.11.096

Davalos, J.F., Chen, Y., Ray, I., 2012. Long-term durability prediction models for GFRP bars in concrete environment. J. Compos. Mater. 46, 1899–1914. https://doi.org/10.1177/0021998311427777

Dejke, V., 2001. Durability of FRP reinforcement in concrete. Licenciate Thesis, Dep. Build. Mater. Chalmers Univ. Technol. Gothenburg, Sweden. Chalmers University of Technology.

Deng, J., Tanner, J.E., Dolan, C.W., Mukai, D., 2010. Development of Accelerated Aging Test Methodology and Specimen for Bonded CFRP Systems. Fifth Int. Symp. Durab. Build. Constr. Sealants Adhes. 6, 342-342–17. https://doi.org/10.1520/stp48978s

Esfahani, M.R., Kianoush, M.R., Tajari, A.R., 2007. Flexural behaviour of reinforced concrete beams strengthened by CFRP sheets. Eng. Struct. 29, 2428–2444. https://doi.org/10.1016/j.engstruct.2006.12.008

FIB Bulletin 14, 2001. CEB FIB bulletin 14, Externally bonded FRP reinforcement for RC structures, International Federation for Structural Concrete (fib). Lausanne, Switzerland.

Gawil, B., Wu, H.C., Elarbi, A., 2020. Modeling the behavior of CFRP strengthened concrete beams and columns at different temperatures. Fibers 8. https://doi.org/10.3390/fib8020010

GB 50608-2010, 2010. Technical Code for Infrastructure Application of FRP Composites. Beijing, China.

Hassan, S.A., Gholami, M., Ismail, Y.S., Sam, A.R.M., 2015. Characteristics of concrete/CFRP bonding system under natural tropical climate. Constr. Build. Mater. 77, 297–306. https://doi.org/10.1016/j.conbuildmat.2014.12.055

Homam, S.M., Sheikh, S.A., Collins, P., Pernica, G., Daoud, J., 2000. Durability of fibre

reinforced polymers used in concrete structures. Proc. 3rd Adv. Compos. Mater. Bridg. Struct. 751–758.

Karbhari, V.M., Abanilla, M.A., 2007. Design factors, reliability, and durability prediction of wet layup carbon/epoxy used in external strengthening. Compos. Part B Eng. 38, 10–23. https://doi.org/10.1016/j.compositesb.2006.06.001

Karbhari, V.M., Engineer, M., 1996. Effect of environmental exposure on the external strengthening of concrete with composites - Short term bond durability. J. Reinf. Plast. Compos. https://doi.org/10.1177/073168449601501202

Karbhari, V.M., Ghosh, K., 2009. Comparative durability evaluation of ambient temperature cured externally bonded CFRP and GFRP composite systems for repair of bridges. Compos. Part A Appl. Sci. Manuf. 40, 1353–1363. https://doi.org/10.1016/j.compositesa.2009.01.011

Karbhari, V.M., Seible, F., 2000. Fiber Reinforced Composites – Advanced Materials for the Renewal of Civil Infrastructure. Appl. Compos. Mater. 7, 95–124. https://doi.org/10.1023/A:1008915706226

Kaw, A.K., 2006. Mechanics of Composite Materials, Second Edi. ed. Taylor & Francis Inc, Bosa Roca, United States.

Krucinska, I., Stypka, T., 1991. Direct measurement of the axial poisson's ratio of single carbon fibres. Compos. Sci. Technol. 41, 1–12. https://doi.org/10.1016/0266-3538(91)90049-U

Li, S., Hu, J., Ren, H., 2017. The combined effects of environmental conditioning and sustained load on mechanical properties of wet lay-up fiber reinforced polymer.

Polymers (Basel). 9. https://doi.org/10.3390/polym9070244

Lu, X.Z., Teng, J.G., Ye, L.P., Jiang, J.J., 2005. Bond-slip models for FRP sheets/plates bonded to concrete. Eng. Struct. 27, 920–937. https://doi.org/10.1016/j.engstruct.2005.01.014

Lu, Z., Xian, G., 2018. Resistance of basalt fibers to elevated temperatures and water or alkaline solution immersion. Polym. Compos. 39, 2385–2393. https://doi.org/10.1002/pc.24220

Lubliner, J., Oliver, J., Oller, S., Oñate, E., 1989. A plastic-damage model for concrete. Int. J. Solids Struct. 25, 299–326. https://doi.org/10.1016/0020-7683(89)90050-4

Mata, O.R., Atadero, R.A., 2014. Evaluation of pull-off tests as a FRP-concrete bond testing method in the laboratory and field. Pract. Period. Struct. Des. Constr. 19, 1–8. https://doi.org/10.1061/(ASCE)SC.1943-5576.0000170

Meier, U., 1995. Strengthening of structures using carbon fibre/epoxy composites. Constr. Build. Mater. 9, 341–351. https://doi.org/10.1016/0950-0618(95)00071-2

MINISTRY OF HOUSING UTILITIES AND URBAN UTILITIES, 2005. Arab Republic of Egypt Ministry of Housing , Utilities and Urban Utilities Egyptian Code of Practice the Use of Fiber Reinforced Polymer (Frp). Egypt.

Naganuma, T., Iba, H., Kagawa, Y., 1999. Optothermal properties of glass particle-dispersed epoxy matrix composite. J. Mater. Sci. Lett. 18, 1587–1589. https://doi.org/10.1023/A:1006660215936

Nam H. Kim, Bhavani V. Sankar, A.V.K., 2018. Introduction to Finite Element Analysis and Design, 2nd ed. John Wiley & Sons, 2018.

NATIONAL RESEARCH COUNCIL, 2014. Guide for the design and construction of externally bonded FRP systems for strengthening existing structures, Advisory Committee on Technical Recommendations for Construction. Roma, Italy. https://doi.org/10.1111/j.1538-7836.2010.03753.x

Nelson, W., 2004. Applied Life Data Analysis, Accelerated Testing: Statistical Models, Test Plans, and Data Analysis, Technometrics. https://doi.org/10.1198/tech.2005.s308

Obaidat, Y.T., Heyden, S., Dahlblom, O., 2013. Evaluation of parameters of bond action between FRP and concrete. J. Compos. Constr. 17, 626–635. https://doi.org/10.1061/(ASCE)CC.1943-5614.0000378

Obaidat, Y.T., Heyden, S., Dahlblom, O., 2010. The effect of CFRP and CFRP/concrete interface models when modelling retrofitted RC beams with FEM. Compos. Struct. 92, 1391–1398. https://doi.org/10.1016/j.compstruct.2009.11.008

Pallempati, H., Beneberu, E., Yazdani, N., Patel, S., 2016. Condition Assessment of Fiber-Reinforced Polymer Strengthening of Concrete Bridge Components. J. Perform. Constr. Facil. 30, 04016052. https://doi.org/10.1061/(asce)cf.1943-5509.0000902

Pan, Y., Xian, G., Silva, M.A.G., 2015. Effects of water immersion on the bond behavior between CFRP plates and concrete substrate. Constr. Build. Mater. 101, 326–337. https://doi.org/10.1016/j.conbuildmat.2015.10.129

Pendhari, S.S., Kant, T., Desai, Y.M., 2008. Application of polymer composites in civil construction: A general review. Compos. Struct. 84, 114–124.

https://doi.org/10.1016/j.compstruct.2007.06.007

Pham, H.B., Al-Mahaidi, R., Saouma, V., 2006. Modelling of CFRP-concrete bond using smeared and discrete cracks. Compos. Struct. 75, 145–150. https://doi.org/10.1016/j.compstruct.2006.04.039

Phani, K.K., Bose, N.R., 1987. Temperature dependence of hydrothermal ageing of CSM-laminate during water immersion. Compos. Sci. Technol. 29, 79–87. https://doi.org/10.1016/0266-3538(87)90050-9

Phani, K.K., Bose, N.R., 1986. Hydrothermal ageing of CSM-laminate during water immersion — an acousto-ultrasonic study. J. Mater. Sci. 21, 3633–3637. https://doi.org/10.1007/BF02403012

Rahimi, H., Hutchinson, A., 2001. CONCRETE BEAMS STRENGTHENED WITH EXTERNALLY BONDED FRP PLATES. J. Compos. Constr. 5, 102–113.

Robert, M., Cousin, P., Benmokrane, B., 2009. Durability of gfrp reinforcing bars embedded in moist concrete. J. Compos. Constr. 13, 66–73. https://doi.org/10.1061/(ASCE)1090-0268(2009)13:2(66)

Santos, P.M.D., Júlio, E.N.B.S., 2013. A state-of-the-art review on roughness quantification methods for concrete surfaces. Constr. Build. Mater. 38, 912–923. https://doi.org/10.1016/j.conbuildmat.2012.09.045

Shrestha, J., Zhang, D., Ueda, T., 2016. Durability performances of carbon fiber-reinforced polymer and concrete-bonded systems under moisture conditions. J. Compos. Constr. 20, 1–12. https://doi.org/10.1061/(ASCE)CC.1943-5614.0000674

Sika Corporation, 2018. SikaWrap ® Hex-117 C CARBON FIBER FABRIC FOR

STRUCTURAL STRENGTHENING 1–4.

Sika Corporation, 2014. Sikadur ® 330 US.

Sika Corporation, 2006. State Highway 183 MacArthur Boulevard Overpass Emergency Repair.

Silva, M.A.G., Biscaia, H., 2008. Degradation of bond between FRP and RC beams. Compos. Struct. 85, 164–174. https://doi.org/10.1016/j.compstruct.2007.10.014

Silva, M.A.G., da Fonseca, B.S., Biscaia, H., 2014. On estimates of durability of FRP based on accelerated tests. Compos. Struct. 116, 377–387. https://doi.org/10.1016/j.compstruct.2014.05.022

Simulia, D., 2014. Abaqus 6.14 Documentation. Provid. RI, USA DS SIMULIA Corp 11.

Smith, S.T., Teng, J.G., 2002. FRP-strengthened RC beams. II: Assessment of debonding strength models. Eng. Struct. 24, 397–417. https://doi.org/10.1016/S0141-0296(01)00106-7

Srinivasaa, V., Shivakumar, V., Nayakaa, V., Jagadeeshaiaiha, S., Seethrama, M., Shenoya, R., Nafidie, A., 2010. Fracture morphology of carbon fiber reinforced plastic composite laminates. Mater. Res. 13, 417–424. https://doi.org/10.1590/s1516-14392010000300022

Subhani, M., Al-Ameri, R., Al-Tamimi, A., 2016. Assessment of bond strength in CFRP retrofitted beams under marine environment. Compos. Struct. 140, 463–472. https://doi.org/10.1016/j.compstruct.2016.01.032

Tatar, J., Hamilton, H.R., 2016. Comparison of laboratory and field environmental conditioning on FRP-concrete bond durability. Constr. Build. Mater. 122, 525–536.

https://doi.org/10.1016/j.conbuildmat.2016.06.074

Timilsina, S., 2018. In-Service Performance Evaluation of Fire and Impact Damaged Bridges with CFRP Laminate Strengthening. The University of Texas at Arlington.

Timilsina, S., Yazdani, N., Beneberu, E., Mulenga, A., 2020. Analysis of a Fire Damaged and FRP Laminate Strengthened Reinforced Concrete Bridge. ACI Struct. J. (in press).

TR55, 2012. Design Guidance for Strengthening Concrete Structures Using Fiber Composite Materials, The Concrete Society. The Concrete Society, Surrey, United Kingdom.

Uthaman, A., Xian, G., Thomas, S., Wang, Y., Zheng, Q., Liu, X., 2020. Durability of an epoxy resin and its carbon fiber-reinforced polymer composite upon immersion in water, acidic, and alkaline solutions. Polymers (Basel). 12. https://doi.org/10.3390/polym12030614

Wang, X., Zhu, Y., Dong, Z.-Q., Wu, Z.-S., Wu, G., 2014. Prediction of Long-Term Performance and Durability of BFRP Bars under the Combined Effect of Sustained Load and Corrosive Solutions. J. Compos. Constr. 19, 04014058. https://doi.org/10.1061/(asce)cc.1943-5614.0000517

Wang, Z., Zhao, X.L., Xian, G., Wu, G., Singh Raman, R.K., Al-Saadi, S., Haque, A., 2017. Long-term durability of basalt- and glass-fibre reinforced polymer (BFRP/GFRP) bars in seawater and sea sand concrete environment. Constr. Build. Mater. 139, 467–489. https://doi.org/10.1016/j.conbuildmat.2017.02.038

WorldClimate.com, 2020. Average Weather Data for Irving, Texas [WWW Document].

URL http://www.worldclimate.com/climate/us/texas/irving

Xie, J., Lu, Z., Guo, Y., Huang, Y., 2019. Durability of CFRP sheets and epoxy resin exposed to natural hygrothermal or cyclic wet-dry environment. Polym. Compos. 40, 553–567. https://doi.org/10.1002/pc.24687

Yazdani, N., Aljaafreh, T., Beneberu, E., 2020. Concrete beam flexural strengthening with anchored pre-saturated CFRP laminates. Compos. Struct. 235, 111733. https://doi.org/10.1016/j.compstruct.2019.111733

Biographical Information

Eyad Alsuhaibani attended Qassim University, Qassim, Saudi Arabia, where he earned a bachelor's degree in Civil Engineering in June 2012 and worked as a graduate teaching assistant for 18 months. He earned a master's degree in structural engineering at the University of Texas at Arlington in Arlington, Texas in August 2016 and worked in collaboration with the City of Arlington to evaluate sewer lines by using multi-sensor robotics. His research interests include advancing non-destructive testing on concrete infrastructure, durability performance of carbon fiber-reinforced polymer used in concrete structures, and finite element analysis.